University of Alberta

Improvements to the resolution and efficiency of the DEAP-3600 dark matter detector and their effects on background studies

by

Kevin S. Olsen

A thesis submitted to the Faculty of Graduate Studies and Research in partial fulfillment of the requirements for the degree of

Master of Science

Department of Physics

Fall 2010
Edmonton, Alberta

Examining Committee

Dr. Aksel Hallin, Physics

Dr. Carsten Krauss, Physics

Dr. Craig Heinke, Physics

Dr. Steve McQuarrie, Oncology

"I've always wanted," he said dreamily, "to know exactly what would happen when an irresistible force meets an im–movable object."

Paul Sarath,
Emeritus Professor of Archaeology,
University of Taprobane
The Fountains of Paradise
Arthur C Clarke

Abstract

The **D**ark matter **E**xperiment using **A**rgon **P**ulse-shape discrimination will be a tonne scale liquid argon experiment to detect scintillation light produced by interactions with weakly interacting massive particles, leading dark matter candidates. The detector will be constructed out of acrylic and use a spherical array of 266 photo-multiplier tubes (PMTs) to count photons produced by an event and will use properties of liquid argon to discriminate signals from background α and γ events. There is currently a smaller prototype, with a cylindrical geometry and using two PMTs, in operation underground at SNOLAB an underground laboratory in eastern Canada. The goal of the prototype detector is to understand the sources of background signals in a detector of our design and to validate our method of distinguishing different types of background radiation. The work presented herein is a series of studies with the common goal of understanding the source of background signals, and improving the resolution and efficiency of the detector.

Table of Contents

1 Introduction **1**

1.1 Observational Evidence of Dark Matter 3

1.1.1 The Coma Cluster 3

1.1.2 Rotation Curves of Galaxies 4

1.1.3 Gravitational Lensing 5

1.1.4 The Cosmic Microwave Background Radiation 8

1.1.5 The Bullet Cluster 11

1.2 The Distribution of Dark Matter 14

1.3 Candidates for Dark Matter 17

1.3.1 WIMPs 17

1.3.2 Axions 19

1.4 Detection of WIMP Dark Matter 20

1.4.1 Indirect Detection 22

1.4.2 Direct Detection 23

1.4.3 Producing WIMPs at Accelerator Labs 26

1.5 Current Dark Matter Searches 26

1.5.1 CDMS 27

1.5.2 PICASSO 30

1.5.3 XENON 31

1.5.4 Controversial Results: DAMA, CoGeNT and XENON100 32

2 The DEAP Programme **34**

2.1 DEAP-1 . . . 34

2.2 Detecting Dark Matter with Liquid Argon . . . 36

2.2.1 Scintillation from Noble Gases . . . 36

2.2.2 Argon . . . 38

2.3 Pulse-shape Discrimination and Analysis . . . 40

2.3.1 Scintillation Efficiency . . . 43

2.3.2 ^{22}Na Calibration . . . 45

2.3.3 PSD Studies . . . 45

2.3.4 Additional Variables and Data Cuts . . . 46

2.4 Detector Operations . . . 47

2.5 DEAP-3600 . . . 49

3 Analysis of Alpha Backgrounds in the DEAP-1 Detector **53**

3.0.1 Alpha Particles . . . 53

3.0.2 Beta and Gamma Radiation . . . 55

3.0.3 Atmospheric Muons . . . 57

3.0.4 Neutrons . . . 58

3.1 Analysis of High-Energy α Backgrounds in DEAP-1 . . . 59

3.2 Closing Remarks . . . 67

4 Relative energy corrections for the DEAP-1 detector **69**

4.1 Fitting Mechanism . . . 70

4.2 Limitations . . . 73

4.3 Applications and Results . . . 74

4.3.1 Correction Factors . . . 74

4.3.2 Calibration of 2008 Data . . . 77

4.3.3 Analysis of α Backgrounds After Corrections . . . 78

4.3.4 Calibration of 2009 Data . . . 81

4.4 Closing Remarks 85

5 Measurement of High Efficiency Hamamatsu R877-100 PMT 86

5.1 Experimental Setup and Procedure 87

5.2 Measurements and Results 92

5.2.1 Dark Pulse Height Spectrum 92

5.2.2 Dark Pulse Rate 96

5.2.3 Triggered SPE Pulse Height Spectrum 98

5.2.4 Averaged Waveforms and Baseline Determination . . . 109

5.2.5 Gain 114

5.2.6 SPE Efficiency 117

5.2.7 Time Resolution 119

5.3 Closing Remarks 124

6 Conclusion 128

A Data Cleaning Cuts and Zfit Corrections 147

B Run List 148

C Fitter Results 149

D List of NIMs Used in Tests 151

E Cicuit Diagrams for Custom Electronics 152

List of Tables

2.1 Basic properties of noble gases 38

2.2 Scintillation properties of noble liquids 39

4.1 2008 α calibrations, after corrections 77

4.2 2009 α calibrations, after corrections 83

B.1 Run sets analysed 148

C.1 Fitter results from Chapter 4 150

List of Figures

1.1 Rotation curve of NGC 3198 4
1.2 Gravitational lensing in Abell 1689 7
1.3 The CMB, WMAP 7-year data 8
1.4 Power spectrum of fluctuations in the CMB 10
1.5 HST image of the Bullet cluster 13
1.6 Map of the Universe from the Sloan Digital Sky Survey 14
1.7 3D Dark Matter distribution over time 16
1.8 WIMP parameter space: SI 27
1.9 WIMP parameter space: SD 28

2.1 Schematic of the DEAP-1 experiment 36
2.2 Example pulses of events with high and low F_{prompt} 41
2.3 SPE spectra of the DEAP-1 PMTs 42
2.4 F_{prompt} versus TotalPE from 2007 surface run 43
2.5 Measurement of $\mathcal{L}_{eff}$ for LAr 44
2.6 F_{prompt} distribution of PSD data, surface run 46
2.7 Schematic of DEAP-3600 50
2.8 Projected WIMP sensitivity for DEAP-3600 52

3.1 Radioactive decay chain of ^{232}Th 55
3.2 Radioactive decay chain of ^{238}U 56
3.3 Muon flux of various underground sites 58
3.4 α energy spectra before and after the boil-off 61

3.5 α energy spectrum from short-lived ^{222}Rn 62
3.6 Comparison of the spectra from backgrounds and pure Rn . . 63
3.7 Background spectrum with pure Rn removed 64
3.8 Zfit versus energy for high-F_{prompt} backgrounds 65
3.9 Zfit distribution of ^{222}Rn and short-lives daughters 66
3.10 Zfit of ^{210}Po peak 67
3.11 Zfit of low energy backgrounds 68

4.1 Fitter example 70
4.2 TMinuit χ^2 distribution for Compton edges 72
4.3 Corrections factors to run 1360 over time 75
4.4 Correction factors within run sets 76
4.5 Corrected α energy spectrum after the top-up 78
4.6 Energy calibration from 2008 radon spike 79
4.7 Corrected background spectrum with pure Rn removed 80
4.8 Uncorrected 2009 high-F_{prompt} spectrum 82
4.9 Model describing α backgrounds in 2009 83
4.10 Corrected α energy spectrum, 2009 84
4.11 Energy calibration from 2009 85

5.1 An unpopulated PMT base. 89
5.2 An unpopulated preamplifier board. 89
5.3 Schematic of test setup electronics 90
5.4 Dark pulse electronics schematic 92
5.5 Dark pulse spectra, Hamamatsu PMT 94
5.6 Dark pulse spectra, ET PMT 94
5.7 Peak-to-valley ratios, Hamamatsu PMT 95
5.8 Peak-to-valley ratios, ET PMT 95
5.9 Dark pulse rates, Hamamatsu PMT 99

5.10 Dark pulse rates, ET PMT 99
5.11 MCA dark rates versus threshold, Hamamatsu PMT 100
5.12 MCA dark rates versus threshold, ET PMT 100
5.13 LED coincidence electronics schematic 101
5.14 Discriminator response to fan-in/fan-out offset 102
5.15 SPE spectra, Hamamatsu PMT 105
5.16 SPE spectra, ET PMT 105
5.17 SPE amplitude from MCA, Hamamatsu PMT 106
5.18 SPE amplitude from MCA, ET PMT 106
5.19 Analysis of low-amplitude MCA noise, Hamamatsu PMT . . . 110
5.20 Analysis of low-amplitude MCA noise, ET PMT 111
5.21 Average waveforms of SPE for varying HV 112
5.22 Comparison of PMT baselines 115
5.23 PMT baseline detail 115
5.24 Averages of the raw PMT pulses 116
5.25 Gain measurements, Hamamatsu 118
5.26 Gain measurements, ET PMT 118
5.27 Relative efficiency, Hamamatsu PMT 120
5.28 Relative efficiency, ET PMT 120
5.29 Timing analysis electronics schematic 121
5.30 TPHC spectra, Hamamatsu PMT 122
5.31 TPHC spectra, ET PMT 122
5.32 Example fit of a TPHC spectrum 123
5.33 Risetime measurement, Hamamatsu PMT 125
5.34 Risetime measurement, ET PMT 125
5.35 TPHC spectra widths, Hamamatsu PMT 126
5.36 TPHC spectra widths, ET PMT 126

E.1 Circuit diagram for the ET 9390B base 153
E.2 Circuit diagram for the Hamamatsu R877-100 base 154
E.3 Circuit diagram for the preamp 155

List of Symbols

2dFGRS	2dF Galaxy Redshift Survey
2MASS	Two Micron All-Sky Survey
6dFGS	6dF Galaxy Survey
ANTARES	Astronomy with a Neutrino Telescope and Abyss environmental RESearch project
ArDM	Argon Dark Matter, two-phase LAr dark matter detector
ASCA	Advanced Satellite for Cosmology and Astrophysics, X-ray telescope
AV	Acrylic vessel
CERN	The European Organization for Nuclear Research
CCD	charge-coupled device
CFHT	Canada-France-Hawaii Telescope
CLASS	Cosmic Lens All-Sky Survey
CLEAN	Cryogenic Low Energy Astrophysics with Noble gases
COBE	COsmic Background Explorer
CoGeNT	Coherent Germanium Neutrino Technology
COUPP	Chicagoland Observatory for Underground Particle Physics
COSMOS	Cosmic Evolution Survey
CRESST	Cryogenic Rare Event Search with Superconducting Thermometers
DAQ	Data acquisition
DEAP	**D**ark matter **E**xperiment using **A**rgon **P**ulse-shape discrimination
DEAP-1	Prototype detector in operation at SNOLAB using 7 kg of LAr
DEAP-3600	full size experiment with 3600 kg of LAr, under construction
DMTPC	Dark Matter Time Projection Chamber
DRIFT	Directional Recoil Identification From Tracks, directional dark matter TPC
EDELWEISS	Expérience pour DEtecter Les Wimps En Site Souterrain, dark matter experiment using cryogenic Ge detectors
EGRET	Energetic Gamma Ray Experiment Telescope
EROS-2	Expérience pour la Recherche d'Objets Sombres, microlensing survey

FET	field-effect transistor
HST	Hubble Space Telescope
HV	High voltage, refers to the operating voltage of a PMT
IRAS	Infrared Astronomical Satellite
KIMS	Korea Invisible Mass Search
KK	Kaluza-Klein, referring to elements of the KK theory of extra dimensions
LAr	Liquid argon
LED	Light-emitting diode
LKP	Lightest Kaluza-Klein particle, WIMP candidate
LNGS	Laboratori Nazionali del Gran Sasso, underground lab in Italy
LSBB	Laboratoire Souterrain à Bas Bruit, underground lab in France
LSC	Laboratorio Subterràneo de Canfranc, underground lab in Spain
LSM	Laboratoire Souterrain de Modane, underground lab in France
LSP	Lightest supersymmetric partner,WIMP candidate
LUX	Large Underground Xenon, two-phase LXe dark matter detector
LXe	Liquid xenon
MACHO	Massive astrophysical compact halo object
MCA	Multichannel analyzer
MIDAS	Maximum Integrated Data Acquisition System
MOND	Modified Newtonian dynamics, an alternative to dark matter
MSSM	Minimal supersymmetric Standard Model
NAIAD	NaI Advanced Detector
NEWAGE	NEw generation WIMP-search With an Advanced Gaseous tracking device Experiment, directional dark matter TPC
NIM	Nuclear instrumentation module
PAMELA	Payload for Antimatter Matter Exploration and Light-nuclei Astrophysics
pe	Photo-electrons
PICASSO	Project in Canada to Search for Supersymmetric Objects
PMT	Photomultiplier tube
PSD	Pulse-shape discrimination
PTFE	Polytetrafluoroethylene, a fluorocarbon solid commonly known as Teflon
ROSAT	Röntgensatellit, a German X-ray telescope
ROOT	Object-oriented multipurpose data analysis package developed at CERN
SAES Getter Group	Manufacturer of gas purifiers
SBA	Super-bialkali, a special photocathode construction made by Hamamatsu
SCA	Single-channel analyzer
SD	Spin-dependent
SDSS	Sloan Digital Sky Survey
SI	Spin-independent

SIMPLE	Superheated Instrument for Massive ParticLe Experiments
SPE	Single photoelectron
SQUID	Superconducting quantum interference devices, measures extremely weak magnetic fields
SRIM	Stopping and Range of Ions in Matter, a computer program for calculating interactions in matter
SUSY	Supersymmetry
TPB	Tetraphenyl butadiene, used as a wavelength shifter
TPC	Time projection chamber
TPHC	Time-to-pulse-height converter, NIM module
UCS	Universal Computer Spectrometer, an MCA from Spectrum Techniques
VUV	Vacuum ultraviolet, light between 100 – 200 nm, strongly absorbed by air
WArP	WIMP Argon Programme, two-phase LAr dark matter detector
WIMP	Weakly interacting massive particle
WIPP	Waste Isolation Pilot Plant, underground lab in Nevada
WMAP	Wilkinson Microwave Anisotropy Probe

Chapter 1

Introduction

The **D**ark matter **E**xperiment using **A**rgon **P**ulse-shape discrimination (DEAP) seeks to detect a new class of particle that would solve many outstanding problems in astrophysics. Weakly interacting massive particles (WIMPs) are a proposed candidate for the composition of dark matter and the DEAP collaboration aims to detect these particles through the weak interaction. We observe a target of liquid argon (LAr) that will produce photons when a collision occurs between a WIMP and an argon nucleus. The first clues that dark matter existed were early observations of the motion of stars relative to our galactic plane and distant galaxies within clusters. Both sets of measurements found that there was a significant discrepancy between the observed mass and that required to cause the observed motions. Evidence that the universe is composed of a large fraction of non-luminous matter has been building continuously since these initial measurements. Major contributions have been studies of the rotation curves of galaxies, observations of gravitational lensing, measurements of the cosmic microwave background radiation, and studies of the X-ray spectrum of galaxy clusters.

The nature of dark matter is speculated from the combined observational evidence, which has presented difficulties for some proposed candidates with each new discovery. The primary distinction is whether dark matter consists

of baryonic matter. A component of the total galactic dark matter distribution being made up of difficult-to-detect, but, normal, baryonic objects is very likely. These could be astronomical objects, such as black holes, brown dwarf stars, or exo-planets. Members of this class of dark matter candidate are called massive astrophysical compact halo objects (MACHOs). However, observations of gravitational lensing rule these objects out as the sole dark matter as they, and their effects, are not common enough to explain the required dark mass. In addition, cosmic microwave background measurements and big-bang nucleosynthesis calculations show that the vast majority of dark matter will not be baryonic. In the non-baryonic category, candidates are classified as hot, warm, or cold, referring to the energy of the particles. Hot dark matter is discounted since it would be more evenly distributed, while observations suggest dark matter clumps around large masses such as galaxies. Furthermore, it has been shown to be incapable of producing the measured large scale structure of the Universe. Cold dark matter is slower moving, allowing it to be gravitationally bound to galaxies, while warm dark matter shares properties of both (MACHOs are a form of cold dark matter). WIMPs are a form of non-baryonic cold dark matter which present little difficulty in conforming to the observational evidence. They are the favoured candidate and have inspired several experiments that have attempted to detect them. At present they remain hypothetical and only limits on their mass and interaction cross section have been set. WIMPs are a generic candidate in that there are no known particles with the required properties and none predicted in the standard model. Theoretical extensions of the standard model do contain particles with such properties and the WIMP designation encompasses an entire group of theoretical predictions.

The following sections will outline the evidence for the existence of dark matter, the candidates for dark matter, how the DEAP collaboration will

detect WIMPs with LAr, and the state of current searches.

1.1 Observational Evidence of Dark Matter

The first use of the term "dark matter" came in 1922, when Jacobus Kapteyn published measurements of the vertical oscillation of stars in our galaxy about the galactic plane. He found that his observations allowed him to calculate the total mass of the system, accounting for objects either invisible to us or not yet observed [1]. The need for a greater total mass on a local scale was confirmed by Jan Oort in 1932 [2]. This is not the type of dark matter we think of today, Kapteyn's calculation led only to a very small correction of the total mass, not enough to cause the amount of trouble that we are currently in. Evidence for dark matter on a galactic scale came during the next decade, and the problems it presented were so great that the finding was largely ignored by the scientific community, until more evidence began to accrue several decades later.

1.1.1 The Coma Cluster

In 1933 Fritz Zwicky published the results of his study of the redshifts of galaxy clusters beyond our local galaxy [3] (translated into English in [4]). From this data, he calculated the velocities of individual galaxies with respect to the mean velocity of the whole cluster. The velocities measured were far too large for the total mass of the cluster, a discrepancy determined by applying the Virial theorem to the Coma cluster. Zwicky estimated the total mass that the Coma cluster needed to bind its galaxies at the observed velocities would require a portion of non-luminous matter that must exceed the mass of visible matter by an order of magnitude.

Zwicky's analysis of galactic masses using the Virial theorem has withstood the test of time, confirmed by measurements of X-ray emissions [5, 6], and

followed more recently by studies of weak-gravitational lensing [7, 8]. This was the first evidence for the existence of dark matter in its present form - on a galactic scale and in far greater abundance than luminous matter. The next substantial work supporting Zwicky's findings would not arrive until 1970.

1.1.2 Rotation Curves of Galaxies

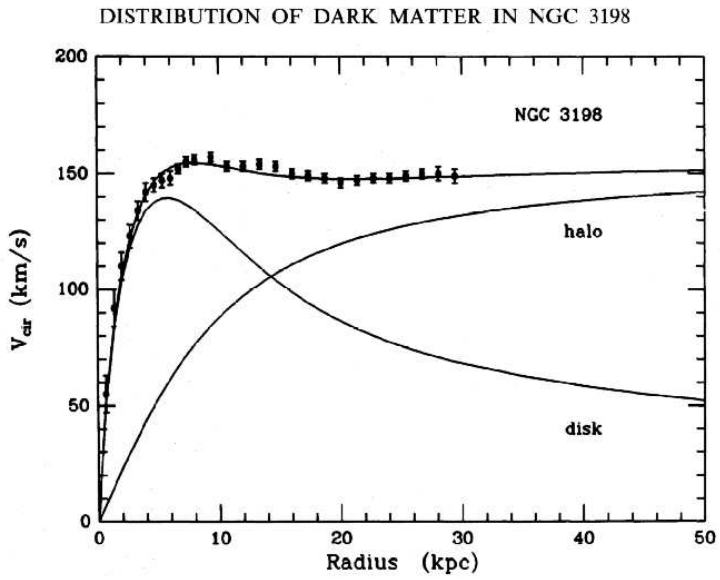

Figure 1.1: An example of a galaxy rotation curve, for the galaxy NGC 3198 [9]. Shown are the separate contributions from the baryonic disk and the dark matter halo (labelled disk and halo, respectively). If dark matter were not present in large quantities, the data would be expected to follow the Keplerian trend calculated for the disk.

A galaxy rotation curve is a plot of its constituents' velocities as a function of distance from the galactic centre. Keplerian physics predicts that these curves for spiral galaxies should rapidly increase to a peak and slowly fall off at large distances. This approach treats assumes the members of the disk lie on a flat disk and obey Kepler's laws of planetary motion. The result is that an object's and its velocity is proportional to its orbital radius as:

$$v \propto \frac{1}{\sqrt{R}}$$

One of the first galaxies to be extensively studied was M31, or Andromeda. Initial measurements were published in 1939 and showed larger than expected velocities at large distances [10]. A much more extensive study that went to much greater distances was performed by Vera Rubin and Kent Ford and published in 1970 [11, 12]. This study showed that the velocities of objects in M31 do not fall away beyond the radius enclosing most stars and gas, as a classical model predicts. This was closely followed by studies of other galaxies, such as of NGC 300, M33 (Triangulum), and NGC 4038/39 (Antennae) in 1970 [13, 14], and M81 (Bode's) and M101 (Pinwheel) in 1973 [15]. In all cases the rotation curves did not match classical predictions and a large portion of undetected mass far from the galactic nucleus was hypothesised, in the form of a galactic halo. An example of the rotation curves for the classical prediction and the measured rotation curve of the galaxy NGC 3198 can be seen in Figure 1.1. The deviation of the measured curve from classical calculations is seen, as are the effect of adding a dark matter halo to the galaxies structure.

Such measurements have since been carried out on several galaxies and the observation has been widely accepted as a characteristic of spiral galaxies. This has become a cornerstone in the argument for the existence of dark matter. Rubin's initial analysis was done using X-ray measurements of the 21-cm line of neutral hydrogen, created by undergoing a change in its energy state. This method has been augmented by the study of gravitational lensing as the primary contributor to evidence for the existence of dark matter.

1.1.3 Gravitational Lensing

In 1911 Albert Einstein expanded his work on the equivalence principle in the general theory of relativity to predict that light may be deflected by a strong gravitational field [16]. While this was met with strong criticism, the effect was verified by an equatorial expedition from the Royal Observatory to study

a total solar eclipse in 1919. At total eclipse the stars in the immediate vicinity of the darkened sun were photographed and their positions and displacements measured. The results confirmed Einstein's prediction [17]. This is the fundamental concept behind the effect of gravitational lensing, the basic formalism of which was published by Einstein in 1936 [18]. In this paper he described the prospect of observing the effect as hopeless. Zwicky, referring to his own calculations of the masses of galaxies which included great portions of invisible matter (Section 1.1.1), concluded that the effect due to larger bodies than stars would be observed with "practical certainty" [19]. The debate would not be settled until 1979 when the first observation of gravitational lensing was published, a double image of the Twin Quasar, QSO 0957+561 A/B, lensed behind a cluster of initially-unresolved galaxies [20]. Since then, gravitational lensing has become one of the most used and most important tools in probing the dark matter sector and building an even larger body of evidence to support its existence.

A gravitational lens is the curvature of space-time caused by a very large gravitational field. The path of light travelling near or through the curved space-time also curves according to general relativity. The extent to which we can observe this effect depends on how strongly space-time is distorted and how directly the path of light interacts with it. The first observations in 1979 were of strong gravitational lensing, in which the most massive objects, such as a cluster of galaxies, are close to being directly in the line of sight of the observed light. This lensing is strong enough to be easily seen and can cause the lensed object to produce multiple images, or a perfect ring, for the observer. An example in the galaxy cluster Abell 1689 is shown in Figure 1.2. This type of lensing is very rare, but was first discovered because it is easily identified.

Since the effect had been established, searches began for a smaller effect,

Figure 1.2: Strong gravitational lensing: the streaked objects in this image are distant galaxies beyond the galaxy cluster Abell 1689, which is a gravitational lens and distorts the image, captured by the Hubble Space Telescope (HST). (NASA [21]).

weak gravitational lensing, which is not easily visible and is caused by smaller deviations in space-time. This can be observed in objects far from the line of sight of the lens, or from less massive objects. The observations require a large number of objects passing through the same lens, each with very small, but coherent, distortions, that can be analysed statistically to determine the mass and distribution of the lensing object. The theory was developed early on, but observations required deep, wide surveys which can be done with higher resolution equipment, such as large charge-coupled devices (CCDs) on optical telescopes. The first large-scale surveys were completed in 2000 on three similar sized telescopes (near 4 m): William Herschel Telescope, the 4-m Victor M. Blanco Telescope, and the Canada-France-Hawaii Telescope

(CFHT) [22–24]. These studies each looked at random sections of sky and were able to detect weak lensing effects in each region and measured the average distribution of dark matter required to support such observations.

Another variation of gravitational lensing, microlensing, has been measured by regarding the change in light intensity with time of background stars as dense objects pass in front of them. Microlensing surveys were performed to detect baryonic dark matter in the form of MACHOs. Surveys performed by the MACHO Collaboration and EROS-2 reported very few lensing candidates, concluding that baryonic matter can only account for a very small fraction of observed dark matter [25, 26]. The results of studying gravitational lensing at each magnitude complemented one another and can be combined with measurements of the cosmic background microwave radiation and thermal X-ray emissions from baryonic gas or plasma to measure the amount of dark matter present in the Universe, its distribution, and its density (discussed in Section 1.2).

1.1.4 The Cosmic Microwave Background Radiation

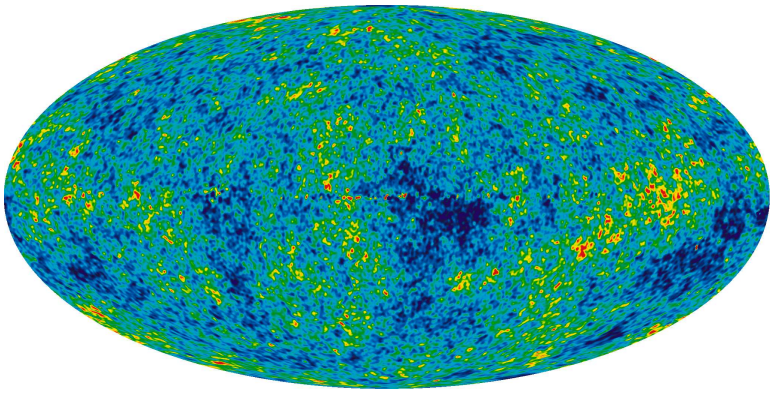

Figure 1.3: An all-sky map of the cosmic microwave background radiation, compiled from seven years of WMAP data. The colours indicate variations in the temperature of the 13.7 billion year old radiation, the temperature range from red to blue is only ± 200 μK (NASA [27]).

The cosmic microwave background radiation (CMB) was discovered accidentally in 1964 by Arno Penzias and Robert Wilson while they studied passive satellite communication techniques using the Holmdel Horn Antenna. The antenna was sensitive to microwave radiation and the initial observation was of an excess noise temperature of about 3.5 K [28]. The noise was radiation from a period after the Big Bang in which matter in the Universe became transparent to photons. This time, known as the last scattering (for a review on modern cosmological models and the production of the CMB see [29]), occurred when the Universe cooled to a point where radiation could no longer ionise normal matter. The radiation that was emitted during this period remains today as low energy microwaves evenly distributed in all directions. The CMB was first studied in detail by the COBE satellite, launched 1989, which determined its important characteristics: that the temperature is almost uniform across the sky; that it follows a blackbody spectrum almost perfectly; and that there are small variations. This was followed by studies specifically aimed at measuring the anisotropies in the CMB, most notably the Wilkinson Microwave Anisotropy Probe (WMAP), launched 2001, and the Planck space observatory, launched 2009.

The CMB has a uniform temperature of 2.725 K [30] in all directions with very small anisotropies, after removing galactic foregrounds and a dipolar signal due to the Earth's motion relative to the CMB. The variations in the temperature profile are small, only on the order of 10 μK. The uniformity of the temperature implies that the Universe was in thermal equilibrium when the CMB was released. To further support this, the radiation also follows the blackbody spectrum and is the most precisely measured blackbody in nature. The very small anisotropies are the most interesting feature, as they give insight to the actual composition of the early Universe. The variations were produced by two classes of event, those before, or during, the last scattering,

and those affecting the radiation en route to the observer. The first class is due to either perturbations in the initial density, and from the dynamics of the surrounding matter at the time of the last scattering. The dynamically induced fluctuations are called acoustic oscillations and their influence can also be seen in baryonic matter in the Universe, the study of which has led to observations about the distribution and structure of dark matter (see Section 1.2). Since dark matter is neutral, and does not interact electromagnetically, the behaviour due to the acoustic oscillations is very different than that caused by the initial density. The second class is due to interactions with baryonic matter (generally hot) and gravitation (such as lensing).

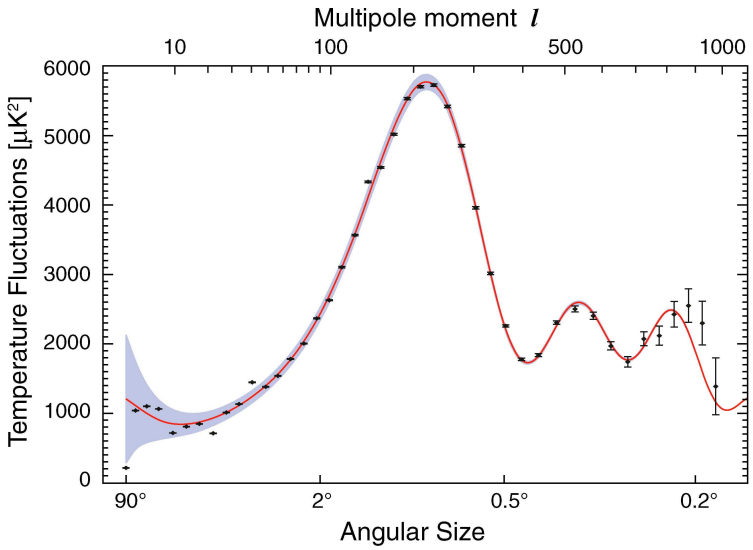

Figure 1.4: The power spectrum of the CMB from five years of WMAP data. This figure compares the angular size of the bright spots on the CMB map (Figure 1.3) to the magnitude of their temperature fluctuations (using a calculated quantity that includes the multipole moments). Each peak represents a different source of the fluctuations. (NASA [31]).

An important implication of the anisotropies comes from the very small amplitudes of the fluctuations. Initial measurements by the BOOMERanG collaboration were able to determine multiple peaks in the power spectrum of the anisotropies, which gave evidence about the origin of the variations and

magnitude of their contributions. They were able to measure cosmological constants and found them to be in agreement to a model of an expanding Universe whose overall shape is flat [32]. However, the small fluctuations would not be enough to cause the structure formation of the Universe that we see today, which is a dense network of filaments with great spaces between them (see Section 1.2). Dark matter would be needed to help produce the structure formation seen today. The power spectrum of the CMB, as measured by WMAP, is shown in Figure 1.4. A more in-depth analysis was done by the WMAP collaboration, which included data from previous experiments, such as BOOMERanG and COBE, and the Sloan Digital Sky Survey (SDSS). With detailed information about the CMB they have been able to calculate the ratios of baryonic matter and dark matter to the total composition of the Universe required to produce the CMB at the time of the last scattering. These measurements, along with those performed by other experiments, fit very well with other observations such as supernovae data and gravitational lensing. The WMAP team reports [30]:

$$\Omega_c = 0.227 \pm 0.014 \quad \text{Dark matter density}$$

$$\Omega_b = 0.0456 \pm 0.0016 \quad \text{Baryon density}$$

$$\Omega_\Lambda = 0.728\ ^{+0.015}_{-0.016} \quad \text{Dark energy density}$$

which means that there is a far greater abundance of dark matter than visible matter.

1.1.5 The Bullet Cluster

The Bullet cluster was first detected by the Einstein Observatory, an X-ray telescope satellite that re-entered Earth's atmosphere in 1982. The peak in the Einstein data was re-analysed by a team searching for failed clusters (large volumes of hot gas that lack galaxies) and optically re-imaged to determine

that is was actually a large galaxy cluster with possible gravitational lensing arcs [33], and designated it 1E 0657-56 in 1995. Follow-up X-ray observations by the ROSAT and ASCA X-ray telescopes showed that the cluster was unusually bright and was likely the result of two merging clusters [34], that such a hot cluster may challenge current models of the Universe was emphasised. Using detailed images from HST in 2004 another team was able to produce a map of the gravitational potential distribution of the clusters using both weak and strong gravitational lensing. They compared this to X-ray observations from the Chandra X-ray Observatory, which has much higher capabilities and resolution than previous studies, and noted a discrepancy in the position of the luminous baryonic matter compared to the gravitational distribution [35]. The interpretation of these results was that a smaller cluster passed through the larger cluster. The collision, at incredibly high speeds, shock compressed the gas in the clusters, resulting in heating and an unusually high emission of X-rays. This gas represents the majority of baryonic matter in the clusters, and was essentially ripped out of the clusters at the site of the collision while galaxies and dark matter passed through. The gravity maps show that the mass distribution, which cannot be accounted for by the galaxies, and the source of the X-ray emissions are in different places, see Figure 1.5. The Bullet Cluster data has been touted as direct evidence of non-interacting, non-baryonic cold dark matter present in galaxy clusters [36, 37].

Even more important is that the difference in mass position peaks and baryonic emission peaks is so great that the current theories of modified Newtonian dynamics (MOND), the most popular alternative to dark matter, cannot account for the discrepancy. MOND was first proposed by Mordehai Milgrom in 1983 as a solution to the problem presented by the rotation curves of galaxies (Section 1.1.2). He proposed that the Keplerian inconsistencies were best explained by a nonlinearity of Newton's second law at low accelerations. He

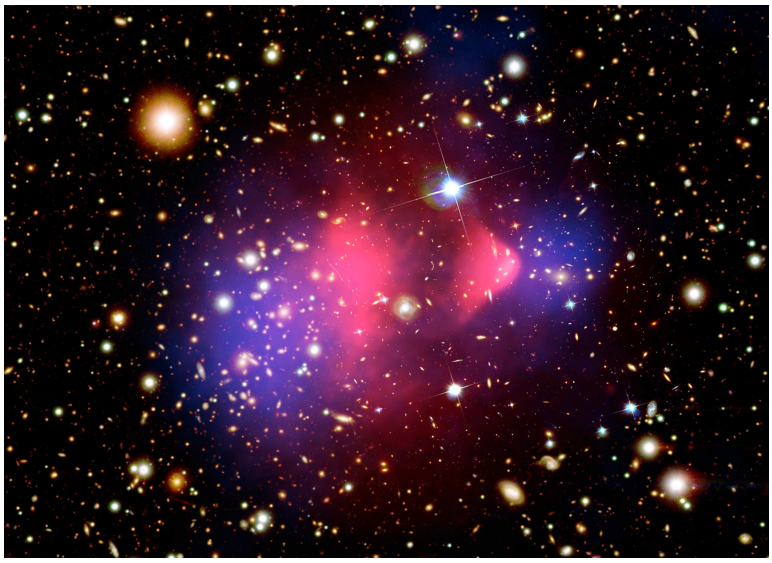

Figure 1.5: A high-resolution image of the Bullet cluster taken with the HST. The smaller cluster is to the right, having passed through the larger cluster on the left. Overlayed on the image are X-ray distributions observed by the Chandra X-ray observatory, in red, and the mass distribution determined from strong and weak gravitational lensing, in blue. The large discrepancy in the positions of the red and blue distributions is too large to be accounted for MOND and is regarded as direct evidence for the existence of dark matter (NASA [38]).

modified Newton's theory of gravity to successfully account for these discrepancies [39–41]. Unfortunately, this was not sufficient and as more evidence for the existence of dark matter was uncovered the MOND theories had to be adapted. This was done successfully until the analysis of the Bullet cluster [36].

Even worse for MOND is that following the analysis of the Bullet cluster other galaxy clusters were observed to behave in the same manner. MACS J0025.4-1222 was reported on in 2008. It is also the result of a collision between two clusters and shows a clear separation between the distribution of gravitational forces and the hot baryonic gas emitting X-rays [42]. A similar analysis was performed on the cluster Cl 0024+17 in 2007, which showed an even larger discrepancy between the X-ray observations of baryonic matter and the gravitational map created from HST data. This cluster is different in that

the collision occurred more than a billion years ago and, after the dark matter of both clusters collapsed inward, the kinematic pressures pushed some matter away from the centre of mass. The observation is of a ring-like structure of invisible mass surrounding the cluster [43]. The combination of gravitational lensing data from the high resolution images produced by the HST and other observations, such as X-rays and microwaves, has become an important tool in probing the distribution of dark matter, but not only in specific clusters. It has proven to be the most powerful tool to probe the large scale structure of the Universe and its relationship to dark matter.

1.2 The Distribution of Dark Matter

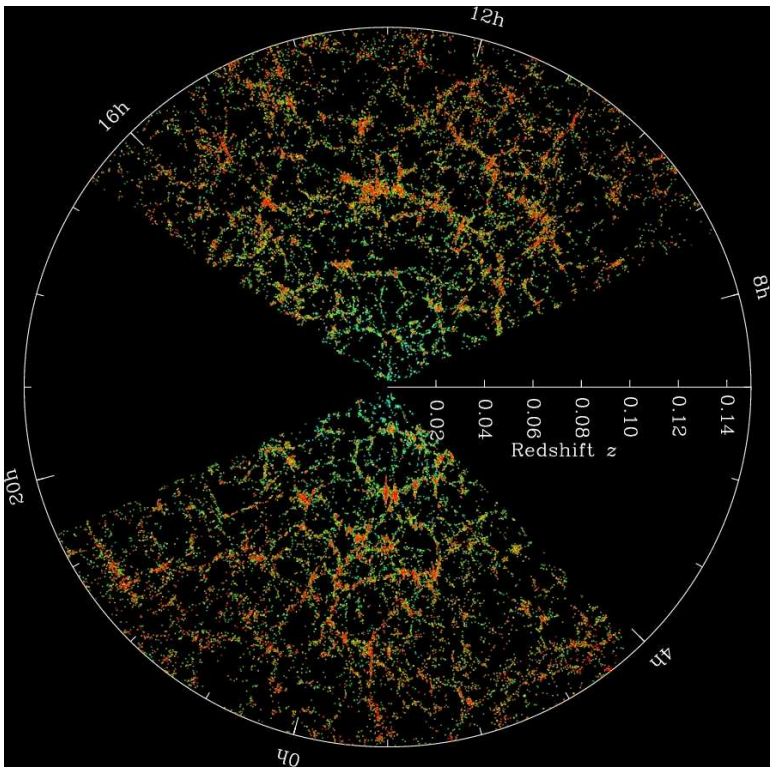

Figure 1.6: A portion of the Universe mapped by the SDSS [44]. The void and filament structure can be clearly seen. The outer edge of the map is two billion light years away. The colour scale shows the age of the stars, red being the oldest (SDSS [45]).

Several studies have been able to provide a very accurate depiction of the large scale distribution of dark matter in the Universe. The first clues came from early redshift studies using faint infrared radiation to catalog large numbers of galaxies. These initial observations quickly saw a nonuniform structure with large voids that were unexpected at the time [46–48]. Several in-depth studies have been since carried out in the optical and infrared regimes that attempt to gather three dimensional data of the large portions of the sky, avoid complications arising from our own galaxy, and create the most complete sky catalogue possible, at the greatest distances. The structure of the Universe consists of long, inter-connected strings of galaxy clusters connected by filaments of galaxies and gas, with great voids containing negligible amounts of mass between them, which can be seen in Figure 1.6. Several subsequent large-scale sky surveys were able to confirm this with increasing resolution and range: 2dFGRS, 2MASS, and 6dFGS [49–51]. The most comprehensive redshift survey is the ongoing SDSS [44], which produces three dimensional models of the distribution of galaxies and clusters. The three dimensional power spectrum of galaxies within the portion of sky mapped by SDSS was able to further constrain the fraction of baryonic matter in the Universe [52] while a comparison to models ruled out the possibility that the observed filament and void structure could be created without dark matter [53, 54]. Without cold dark matter the structure would be washed out and more uniform. Furthermore models also ruled out the ability for hot dark matter to create these structures [55] (established earlier using smaller scale redshift surveys).

Further information about the distribution of dark matter within the large scale structure of the Universe has been developed using contributions from several data sets. For instance, the COSMOS project, undertaken with the HST, combines data from several sources, including the Chandra X-Ray Observatory, the XMM-Newton X-ray telescope, and the Very Large Array radio

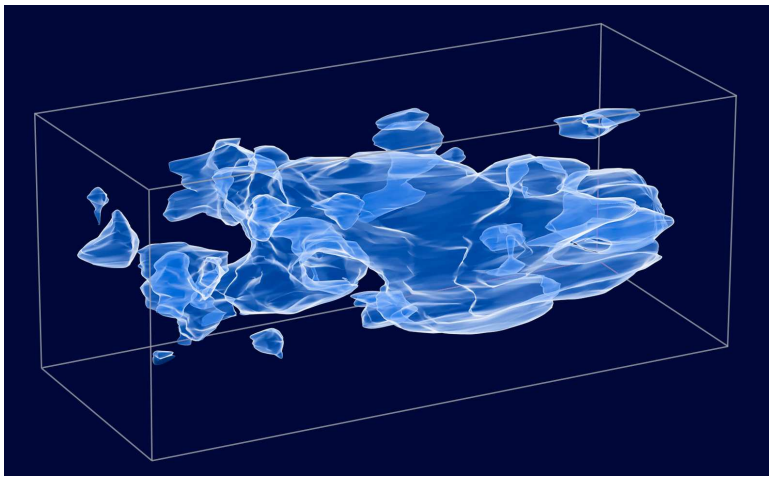

Figure 1.7: A compilation computed from weak lensing measurements performed by the COSMOS survey using data taken by the HST with increasing distance,this graph illustrates the formation of the Universe's filament structure and the clumpiness of the dark matter halos surrounding it. From right to left, the three-dimensional representation moves from both a greater distance, and from further back in time. The dark matter halo becomes tighter, with more defined structure on the left as the gravitational forces cause the halo, and the baryonic matter within it, to collapse into the large scale structure we see today (NASA, adapted from [56]).

observatory [57]. A primary goal of COSMOS is to study the relationship between the large scale structure of the Universe and dark matter. The gravitational lensing surveys identify the distribution of matter while surveys covering most of the spectrum, from radio to X-ray, tightly constrain the localisation of baryonic matter. By combining these measurements, as was done to investigate the Bullet cluster (Section 1.1.5), the development of dark matter halos over time and three dimensional models of the distribution around galactic filaments have been constructed [58, 59] (see Figure 1.7). These modern observations, along with the measurements of the CMB, all from the greatest observatories ever constructed, form an immense body of evidence for the existence of dark matter and have already placed a great deal of constraints on the nature of dark matter, allowing for very specialised direct searches to be developed.

1.3 Candidates for Dark Matter

The body of evidence just presented has given the experimental community a very good idea of what to look for to confirm the existence of dark matter. It has also allowed the theoretical community to try to place dark matter particles within the models of particle physics beyond the Standard Model. Dark matter does not interact via the strong interaction or electromagnetically; it is particulate, and does not form larger atoms. It is neutral and massive, travels slowly enough to be gravitationally bound to stars and galaxies, and is non-baryonic. There is no known particle with these characteristics, nor are there any such hypothetical particles predicted by the Standard Model. There is, however, an entire zoo of particles beyond the standard model that may be suitable to make up dark matter. Many of these collectively fall under the generic classification of WIMPs, while another candidate, the axion, is distinct due to its much lower mass. While we search for a dark matter candidate, it is accepted that the distribution is partially composed of candidates already ruled out by observation, such as MACHOs or relativistic neutrinos. For a more complete review of many more possible dark matter candidates see [60].

1.3.1 WIMPs

Neutralinos

The neutralino is predicted by the leading extensions to the Standard Model: supersymmetry (SUSY) and the minimal supersymmetric Standard Model (MSSM), which is a reduction of supersymmetry to produce the fields of the Standard Model. There are several good candidates for WIMPs in SUSY, but many are ruled out by observational evidence, such as the gravitino which would be hot dark matter, or the sneutrino which is unstable and would not exist in the observed abundance. The best candidate for WIMPs in SUSY is

the lightest supersymmetric particle (LSP). A new symmetry is expected in SUSY, called R-parity for which we assign all the Standard Model particles R = 1, and all the super-partners R = −1. When SUSY is minimised R-parity will be conserved, the consequence of which will be that the LSP is stable (see [61]). In MSSM the LSP is the neutralino, which becomes the best WIMP candidate. To date no super-partners have been detected in a lab, but with the completion and commissioning of the LHC at CERN, and first collisions taking place in 2009, the rise or fall of SUSY is close at hand. Neutralinos are a leading candidate for two main reasons: they easily conform to the body of evidence for dark matter, and the SUSY theories, particularly MSSM, are well understood. MSSM is mathematically robust and calculations of neutralino densities can be performed.

Lightest Kaluza-Klein Particles

During early searches for unification theories, the Kaluza-Klein (KK) theory was proposed to unite gravity and electromagnetism using extra dimensions. This was overtaken by the emergence of the strong and weak interactions, however. The theory was revisited several times by such theories as string theory and large extra dimensions. Of particular note are theories with extra dimensions that are compactified, that is, that allow all particles to propagate through all of the dimensions. Such theories are called universal extra dimensions and particles have their momentum quantised proportional to R^{-1}, the size on the extra dimension. The lightest neutral and stable KK particle (LKP) then makes an excellent candidate for dark matter, falling under the WIMP classification.

Heavy Photons

Under certain theoretical conditions, the breaking of global symmetries may give rise to pseudo-Goldstone bosons. Such conditions lead to gauge theories which produce Higgs bosons in which symmetries are not exact and must be explicitly broken. Where the result would normally be an exact symmetry, spontaneously broken, and producing a massless Goldstone boson, such approximate symmetries produce spinless bosons with small masses, so-called pseudo-Goldstone bosons [62]. In such models the Higgs is a pseudo-Goldstone boson and is naturally light, while other heavy particles are produced. A new symmetry can be introduced to create T-parity which forces the lightest particle with odd T-number to be stable, this particle becomes the candidate for dark matter [63]. The little Higgs theories are fairly new and still being adapted, but there is hope that the LHC will be able to probe the parameters required very quickly and allow for either rapid development (or rapid demise).

1.3.2 Axions

An outstanding problem in physics is why cp-symmetry is violated in electroweak theory but seems to be conserved in quantum chromodynamics, dealing with the strong interaction. A popular solution is Peccei-Quinn theory, which introduces a new global symmetry that is spontaneously broken. The resulting Goldstone boson is the axion, given mass from the model's strong interaction [64]. Searches for axions have been ongoing, but have only been able to constrain the mass to < 0.01 eV, which makes it distinct from other WIMP candidates. The ability to detect axions in this range by dark matter experiments is close at hand and their parameter space may be ruled out by the next generation of direct searches. If both SUSY is correct and axions are discovered, then the LSP is the partner to the axion, the axino, which will replace the axion as the favourable dark matter candidate.

1.4 Detection of WIMP Dark Matter

The nature of WIMPs described above limits the methods that we may use to search for them. Since WIMPs will have a very low density, and have been shown to have a small scattering cross section by experiments already conducted, WIMP scattering events are very rare. Experiments are typically located deep underground and designed to have very low backgrounds. We know that WIMPs will only be found by two of the fundamental interactions, weak and gravitational and we have already observed and studied many of the gravitational effects (and we are still searching for new evidence).

A confirmation of the existence of dark matter in the proposed particle form will have to come from the observation of weak effects. The experiments capable of doing so that have been designed, operated, or proposed are classified as either direct or indirect. The direct searches are additionally distinguished by whether they are spin-dependent (SD) or spin-independent (SI), and whether they are directional. Indirect searches for WIMPs look for the products of their annihilation from a WIMP encountering its antiparticle, or another WIMP if they are Majorana particles (they are their own antiparticle). Direct searches look for evidence of a WIMP scattering off of a target by studying the energy deposited in the material by the recoiling nucleus which can produce a variety of effects. There are four primary detectable forms of deposited energy being currently studied: heat, sound, ionisation, and scintillation light. Ionisation is detected in conjunction with another form of energy to give more information about an event.

The dependence on the type of spin coupling is the primary distinction among experiments. In order to design an effective experiment we calculate the WIMP detection rate for a given theoretical model (although with approximations the calculation becomes largely model-independent). The parameters

of such calculations are the WIMP mass and the interaction cross section (and the energy spectrum of annihilation products in the case of indirect detection). The equation is constructed using the different WIMP-nucleon couplings. In the non-relativistic limit only two couplings contribute: axial-vector coupling to nuclear spin (SD), and scalar coupling to the nuclear mass (SI). Note that SD calculations differ depending on whether the WIMP scattering is due to neutrons or protons. Both couplings always contribute and should be added together. However it is assumed, in general, that only one of the couplings dominates. We have, therefore, two sets of WIMP parameters to probe independently. Most experiments are of the SI type and it has been shown that for heavier target nuclei the mass coupling is dominant for most supersymmetric models. In SD coupling, nucleons with different spin states can cancel in the overall coupling strength if different, whereas for SI coupling the coupling strength is dependent on the square of the mass number. The contributions from SI and SD coupling are model dependent and significantly contribute to model uncertainty [61]. So far WIMP searches have produced null results, which are reported as exclusion zones in the parameter space of the WIMP cross-section and mass within the sensitivity of the experiment. These exclusion plots are distinct for each coupling, and are shown in Figures 1.8 and 1.9 in Section 1.5 for SD and SI (proton and neutron), respectively.

Directional dark matter experiments are sensitive to the direction of the arrival of the incoming WIMP. Many detectors of this type use time projection chambers (TPCs) with notable examples being the long running DRIFT (Boulby mine) experiment and the newly developed DMTPC (WIPP) and NEWAGE (Kamioka). For a current review on the status of directional dark matter experiments see [65].

The following sections will outline the indirect search programmes, describe how the energy deposited in a direct detection experiment is utilised, and

briefly outline those scientific programmes. I will provide more detail about the current experimental limits and the programmes achieving them, including how the DEAP collaboration will use scintillation light from liquid argon to detect WIMPs.

1.4.1 Indirect Detection

Many of the extensions to the standard model predict that their lightest stable particles may annihilate and even predict the product and whether the LSP should be a Majorana particle. Evidence for WIMP annihilation would come in the form of gamma rays, neutrinos, anti-protons, or positrons. Some experiments have already reported excesses of gamma rays, positrons, or anti-protons originating in deep space, but the sources are not well understood and other astrophysical explanations (e.g. pulsars) are able to account for them. Gamma ray results have notably come from the EGRET experiment on the Compton Gamma Ray Observatory, and the current search from the Fermi Gamma-ray Space Telescope, launched 2008. Observations of anti-matter have notably been reported from the PAMELA instrument. For a more complete review of these deep space observations, their results, and their implications, see [60].

Due the difficulties associated with deep space indirect dark matter searches it has been proposed that high density dark matter around a heavy, nearby object may produce a more distinct signal. There are two experiments currently operating that search for neutrinos from the centre of the Earth or the Sun that may be due to WIMP annihilation. ANTARES is a water Cherenkov detector located in the deep Mediterranean sea. It has a similar counterpart at the South Pole, the IceCube Neutrino Observatory. Both detectors are similar in their construction, deploying long strings of detector modules that measure Cherenkov radiation from natural water using PMTs. They complement one

another in their direction and location and both are in the beginning of their data taking runs [66, 67].

1.4.2 Direct Detection

Historically, development of dark matter detection needs was motivated by the need to move to higher sensitivity targets, and then to larger scales. The earliest devices were semiconductor-type, whose scientific goals were primarily aimed at neutrino physics, followed by solid scintillators. The need for higher sensitivity, better signal identification, and background rejection led to advances in cryogenic and multi-phase detectors, such as the XENON and CDMS collaborations (discussed in Sections 1.5.3 and 1.5.1, respectively) which have become leaders in the field with small SI detectors. The current push is to build very large scale experiments, with interest in several different detector technologies, notably the noble liquid detectors and cryogenic Ge crystals, but also from newer technologies, such as innovative bubble chambers.

Heat depositions are measured as thermal phonons using cryogenic bolometers. There have been several experiments using this method: EDELWEISS (LSM) and CDMS (Soudan), which also measure ionisation; and CRESST (LNGS) and ROSEBUD (LSC), which also measure scintillation light. EDELWEISS [68] and CDMS both use high-purity Ge crystals, while ROSEBUD used sapphire (Al_2O3) [69], and CRESST used $CaWO_4$ [70]. CDMS has made one of the most sensitive measurements to date, while CRESST, ROSEBUD, and EDELWEISS have made plans to form a larger collaboration, EURECA (LSM), which will create a tonne scale cryogenic detector looking for both thermal phonons and scintillation light [71]. A description of the CDMS experiment, its current results and future goals will be discussed in section 1.5.1.

A novel approach to dark matter detection uses superheated liquids to make a bubble chamber. The PICASSO (SNOLAB) experiment measures the

acoustic phonons created by phase changes in the target liquid. The PICASSO experiment is of the SD type and has demonstrated very strong discrimination power at different temperatures. It has recently set the current limit for SD-proton parameter space and its results will be discussed in Section 1.5.2. Two similar experiments are COUPP and SIMPLE, both SD. SIMPLE (LSBB) uses several superheated droplet detectors containing C_2ClF_5 in a gel. When energy is deposited in the detectors, the gel undergoes a phase transition to gas and the pressure change and acoustic signatures are recorded [72]. COUPP (Fermilab) is a more conventional bubble chamber with a superheated CF_3I target. Events are recorded with a camera and the shape and rate of bubble development is used to discriminate event sources [73].

The scintillation based detectors make up the majority of the dark matter experimental development. Early experiments used solid scintillators, such as NAIAD (Boulby [74]) and DAMA (LNGS, see Section 1.5.4), which deployed NaI detectors. More recently, KIMS (Yangyang [75]) used CsI(Tl) crystals to achieve higher sensitivity. All three experiments are sensitive to both SI and SD coupling, but were shown to be the most competitive in the SD regime for proton coupling. The SI and SD-neutron sectors have been dominated by CDMS and the noble liquid scintillation experiments. The competitive field of direct dark matter detection is largely at the same stage: many collaborations have built prototype detectors to test the projected sensitivity and background rejection power of their design, some have built intermediate sizes that are currently operational, and most plan to enter the tonne-scale regime in the near future. Targets are almost exclusively liquid argon or xenon, LXe being most popular, and they are either single phase, or two phase, incorporating a TPC and using a ratio of scintillation light to ionisation as a form of pulse-shape discrimination (PSD).

The Cryogenic Low Energy Astrophysics with Noble gases (CLEAN) is a

medium-sized, single-phase detector at SNOLAB that was developed alongside DEAP. It will be run interchangeably with both argon and neon to be able to compare WIMP signals from both targets [76, 77]. Testing was performed with a small prototype and a scaled up version with 500 kg of active mass is under construction at SNOLAB. Another single-phase detector is XMASS at Kamioka Underground Observatory. XMASS will use an 800 kg LXe target surrounded by an array of 642 small, hexagonal PMTs [78]. Including DEAP, there are only three single-phase detectors in development, with the DEAP programme poised to become the first to reach the tonne scale. The operational principles of all three detectors are very similar, while the engineering tasks and designs differ greatly, a primary objective of which is having ultra-low backgrounds. The PSD techniques developed by the DEAP/CLEAN collaboration sets them apart from the XMASS programme.

There have been several two-phase detectors built and under construction. These detectors allow for a region of gas above the liquid. This gas region forms the end of a TPC while the liquid is used as a drift chamber. When an event occurs in the liquid phase, scintillation is produced and measured while ionisation electrons are drifted into the gas phase, where additional scintillation light is generated. The ionisation may also be counted directly with proportional counters. Using argon as a target are WArP (LNGS) and ArDM (CERN, surface). The WArP collaboration has recently completed a detector with 140 kg active mass and has begun taking data underground [79] while ArDM is developing a much larger detector at surface with an 850 kg active mass [80], with future plans to move underground (unspecified site). Among the xenon based two-phase experiments, two groups were able to build prototype detectors and set competitive constraints on WIMP parameter space: XENON10 (LNGS) and ZEPLIN-III (Boulby). The XENON collaboration, along with CDMS, has been able to build the most sensitive detectors to date

and will be discussed in Section 1.5.3.

1.4.3 Producing WIMPs at Accelerator Labs

An additional way in which WIMP candidates may be discovered is their production in the most powerful particle accelerators: the Tevatron at the Fermi National Accelerator Laboratory and the Large Hadron Collider at CERN. These colliders produce the most energetic particles in a laboratory setting to date and may be able to detect WIMP candidates as missing energy from a collision. The LHC in particular will be able to probe most of the parameter space needed for many supersymmetric scenarios. Such constraints placed on extensions to the standard model and the confirmation of the existence of other particles within these theories will allow dark matter searches to narrow the parameter space of their search and complement the finding by narrowing down the range of possible WIMP candidates. Unfortunately, detecting WIMP candidates produced in particle accelerators will not be enough to prove the existence of dark matter. A confirmation that the discovered particles are actually abundant in the Universe with required distributions will still be needed.

1.5 Current Dark Matter Searches

In the SI regime, the best limits on the interaction cross section and mass for a WIMP have been set by the XENON and CDMS collaborations, followed by ZEPLIN and EDELWEISS. The current limits for SI cross sections as a function of WIMP mass are shown in Figure 1.8. These same groups (except EDELWEISS) also dominate the SD-neutron regime, with the XENON and ZEPLIN groups achieving the highest sensitivity, Figure 1.9 (top). The SD-proton regime is dominated by solid scintillator experiments and bubble chambers, led by PICASSO and COUPP, especially for low WIMP mass, fol-

lowed by older results from KIMS and NAIAD, Figure 1.9 (bottom). The following sections will give details about the leading experiments using each of the primary methods for direct detection.

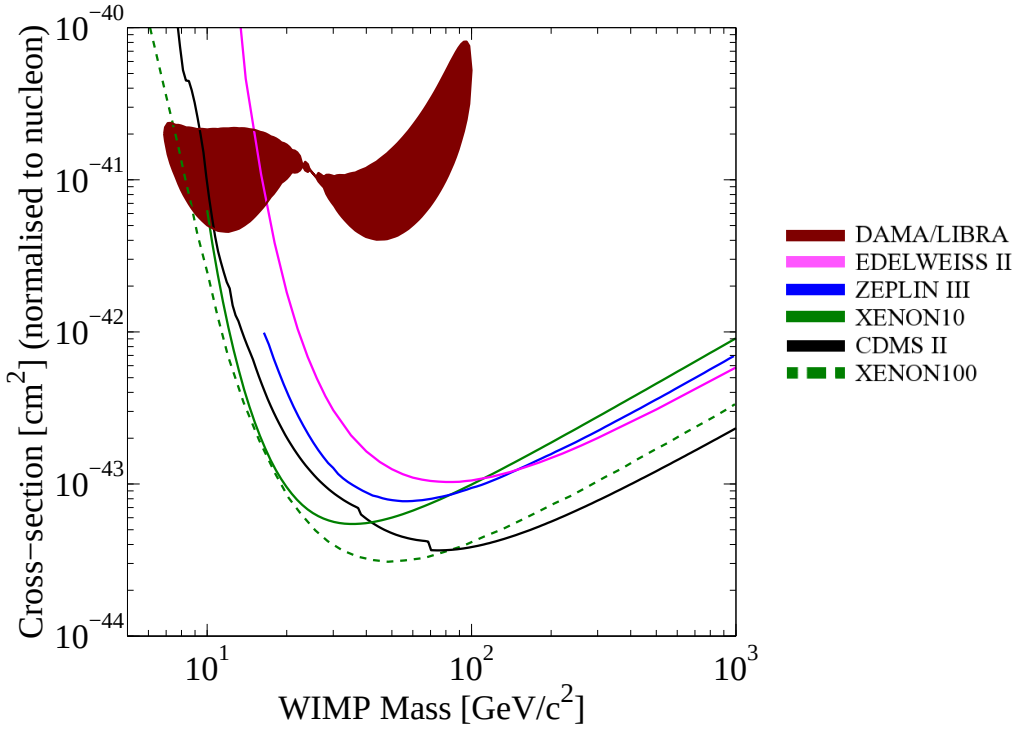

Figure 1.8: Current results from leading WIMP searches for SI WIMP-nucleon scattering. The region above an experiment's line is the parameter space excluded by that search. The shaded area is the parameter space allowed by DAMA, now mostly excluded by other experiments. Plot generated using [81] using data from [68, 82–86].

1.5.1 CDMS

The Cryogenic Dark Matter Search (CDMS) uses a combination of ultra-pure Si (100 g) and Ge (250 g) crystals mounted with photolithographically-fabricated thin films. These detectors operate at T$<$ 40 mK and the thin films are able to detect phonons produced by variations from the operating temperature, with their signals being read by SQUID devices. Detectors are organised in a tower structure, sitting in a vertical stack. The entire assembly sits in

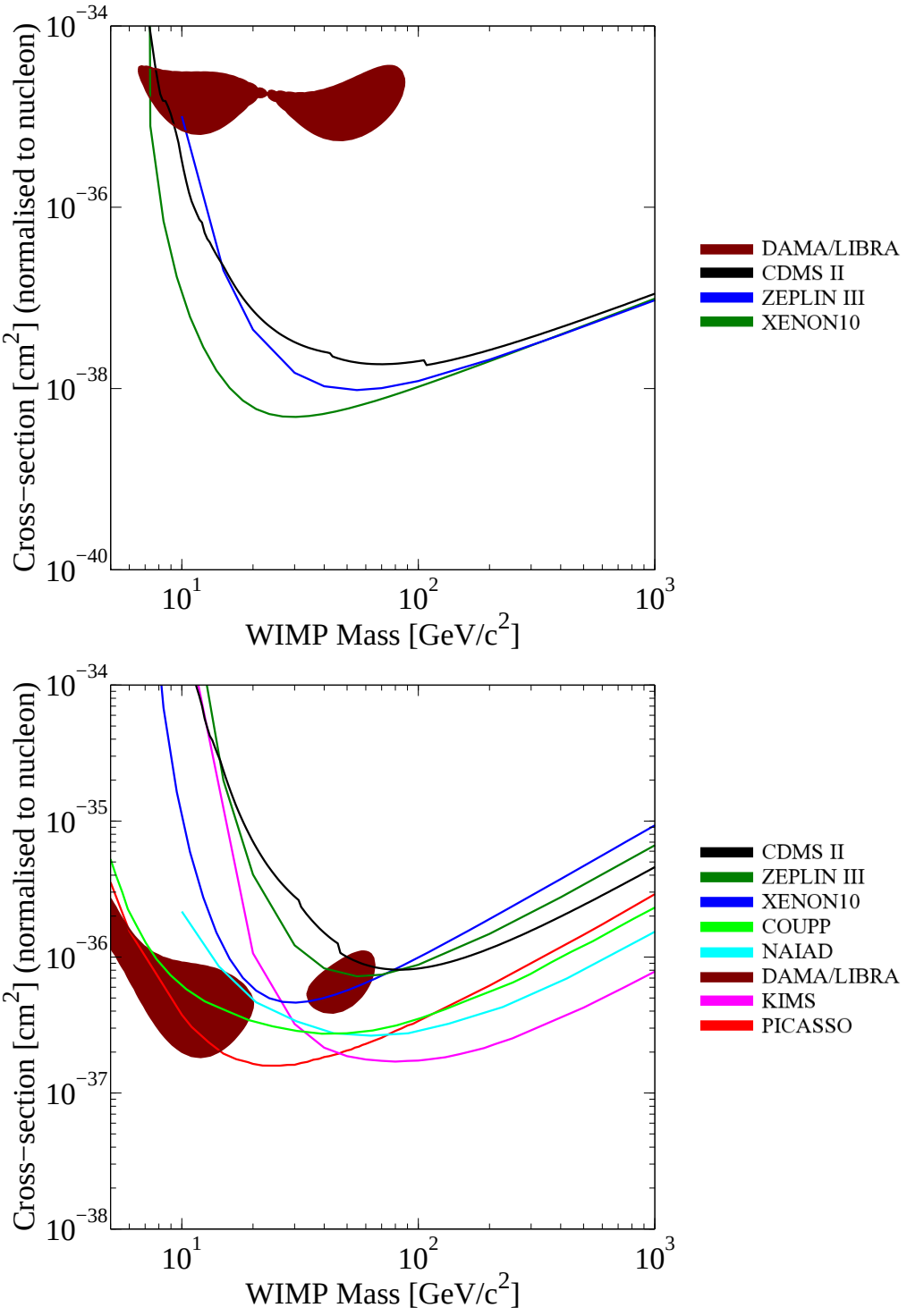

Figure 1.9: Current results from leading WIMP searches for spin-dependent WIMP-neutron (top) and WIMP-proton (bottom) scattering. The region above an experiment's line is the parameter space excluded by that search. The shaded area is the parameter space allowed by DAMA. Plots are generated using [81] with SD-neutron data from [82, 87–89], and SD-proton data from [73, 75, 82, 87–91].

an electric field, the lowest detector forming the ground reference point. The electric field drifts ionisation electrons to a warmer stage of the cryostat where FETs are used to measure the amount of ionisation. The cryostat assembly is made of high purity copper to ensure low radioactivity, and is shielded with lead recovered from the ballast of a sunken eighteenth century French ship, which ensures that radioactive impurities have decayed away sufficiently. The lead is supplemented with a polyethylene shield to further attenuate neutrons and the entire cryostat is surrounded by an active muon veto system. Further shielding has been provided by installing the cryostat in the Soudan Underground Laboratory in northern Minnesota (experimental details from [87, 92]). Studies of the ratio of phonon signals to the amount of ionisation allow for precise particle identification, easily vetoing β events while allowing nuclear recoils. The major experimental hurdles are similar to those of DEAP, properly identifying neutrons that produce a similar signal to WIMPs, and further reducing background sources.

The first iteration of the CDMS experiment was CDMS I, during which a small number of detectors were developed to test multiple new technologies. They were deployed at a shallow depth of 10.6 m in the Stanford Underground Facility and later moved to Soudan in 2003. The first WIMP search was taken with CDMS II beginning in 2006 at Soudan. 30 improved detectors were deployed in five towers, totalling 4.75 kg Ge and 1.1 kg Si, and run in stages until 2009. The combined data places the most sensitive restriction on SI WIMP scattering at high WIMP masses to date [83, 93]. The next phase is SuperCDMS, in which the detector towers will be replaced with "super" towers using larger crystals and improved phonon detectors. SuperTower 1 has been installed and features five 1" thick Ge crystals weighing 0.64 kg each. CDMS plans to achieve a 15 kg Ge detector at Soudan, with future goals to build a 100 kg Ge detector at SNOLAB (which offers greater shielding than

Soudan due to its depth). A major issue facing the CDMS collaboration is the high cost of manufacturing the Ge detectors compared to PICASSO, COUPP, and the noble liquid experiments. Achieving a tonne scale detector with noble liquids will be a fraction of the cost of doing the same with Ge crystals.

1.5.2 PICASSO

The Project in Canada to Search for Supersymmetric Objects (PICASSO) is located at SNOLAB and uses superheated droplets of C_4F_{10} suspended in water-based polymerised gel. The droplets are between 10 and 200 μm and contain the isotope ^{19}F, which is favourable for SD WIMP sensitivity [94]. When the ^{19}F is energised by incident particles it causes its host droplet to undergo a phase transition to gas which is explosive enough to create measurable acoustic signals. PICASSO uses piezoelectric transducers to detect sound waves caused by these interactions and has demonstrated that the sensitivity to different sources is dependent on the temperature of the superheated droplets, which allows their WIMP search to be insensitive to many forms of background radiation, such as γ and β particles [95]. Each event in the detectors results in a loss of active volume due to the phase change, which affects the WIMP sensitivity of a run over time. At the end of a timed run the detectors are pressurised to return the gas bubbles to liquid droplet form.

The PICASSO experiment has also been run in phases, starting with prototype detectors tested on the surface and underground at SNOLAB and the Windsor Salt Mine. These were polyethylene containers with only two piezoelectric transducers filled with 1 L of the polymerised gel containing C_4F_{10}. The droplets at this stage were small, ≈ 11 μm [94]. Advanced detectors began being installed at SNOLAB in 2007, beginning with a set of four that have since been running continuously. The goal was to install an array of 32 detectors in independent groups of four, and was completed in 2008. The WIMP

search with the full 32 detectors ran through 2009 and culminated in the most sensitive SD WIMP search to date [91], and continues to collect data. The new detectors contain 4.5 L of active gel, are made with acrylic containers in a stainless steel frame, and have nine piezoelectric transducers each.

1.5.3 XENON

The XENON collaboration has developed the leading two-phase noble liquid dark matter search using scalable technology in a multi-stage programme. The first iteration, XENON10, used a 15 kg cylindrical LXe target. The cylinder is constructed with copper rings to provide an electric field, separated with Teflon spacers. LXe is not contained by the cylinder and PMTs on the outside use the remaining LXe as an active shield, relying on the excellent stopping power of the large xenon nuclei. The bottom end is fitted with a quartz window and an array of 1" square PMTs. The upper end was fitted with a multi-wire proportional counter finishing the TPC and topped with a second PMT array within a gaseous xenon stage. Electrons exit the TPC into the gaseous xenon and scintillate again. The ratio and time difference between the primary and secondary scintillation light is the basis for particle identification. The detector is built with copper and stainless steel and shielded inside a castle made of a layer of depleted lead and polyethylene walls [96]. XENON10 was deployed underground in the Gran Sasso National Laboratory (LNGS) in Italy in 2006 and run until 2007, resulting in a WIMP search that remains one of the most sensitive [84, 97]. The second iteration is XENON100, built in 2008 at LNGS, which began its WIMP search in 2010, with results from 11.2 days announced [85]. This detector's design is a scaled version of the prototype with additional shielding and an active muon veto. XENON100 is claimed to have the lowest backgrounds of any dark matter experiment currently operating underground. Again, properly identifying nuclear recoils from neutrons and

reducing background sources are ongoing goals of the collaboration. The next planned upgrade is a one tonne LXe mass immersed in a large water shield with active muon veto capability.

1.5.4 Controversial Results: DAMA, CoGeNT and XENON100

There are a few prominent dark matter experiments from the past and present that I have not commented on that may prove to be very significant. I have not discussed them due to the controversies resulting from their claims. The primary concern is that the experimental results from detectors made with different materials have not always been reconcilable with one another. As the next generation of detectors comes online, more results are collected, and careful analysis is performed the controversies should be laid to rest over time.

First is the DAMA collaboration which deployed NaI scintillators at LNGS. They reported an annual modulation in their signal, but only at very low energies [98]. This is, significantly, the first claim of seeing a dark matter signal. There are two problems with the DAMA result: they have not been able to convince many members of the dark matter community that they fully understand their backgrounds, and the parameter space in which their experiment is sensitive has been ruled out with null results by several other experiments, including the CDMS, XENON100 and PICASSO experiments. Similar experiments using NaI crystals and lower backgrounds need to be performed to investigate the signal modulation, preferably in the southern hemisphere to test whether any observed oscillations are seasonal. Further probes of the low-mass WIMP region are needed.

The CoGeNT and XENON100 results are very recent, pre-published in 2010 and come directly to odds with one another. CoGeNT (Soudan) uses p-type point contact (PPC) germanium detectors, it is a small experiment devel-

oping the PPC technology for larger application. Their result showed a number of signals from low energy recoils consistent with low-mass WIMPs, but otherwise unexplained by backgrounds [99]. The first results from XENON100, released only months later, directly challenge the CoGeNT result by claiming a null result in the low-mass parameter space to which CoGeNT and DAMA are sensitive [85]. Furthermore, the XENON100 report has been openly criticised by both theorists and experimentalists alike [100, 101]. As with the DAMA result, time should resolve the controversy.

Chapter 2

The DEAP Programme

The DEAP programme is divided into two stages: DEAP-1 and DEAP-3600. The prior is a small prototype currently underground at SNOLAB, while DEAP-3600 will be a tonne-scale, spherical variant intended for a long term WIMP search. The prototype was developed primarily to demonstrate pulse-shape discrimination, and has been used extensively to test and improve analysis algorithms, and to study and understand the sources of background radiation that we will face when operating DEAP-3600. DEAP-1 has gone through several operational periods, beginning with a surface run at Queen's University in Kingston, and the fourth operational period has been running through August 2010. Many lessons about backgrounds originating in the detector have been learned and improvements to the construction methods, analysis, and argon purification system were made. The electronics and PMTs have been upgraded to match those that DEAP-3600 will use. This has allowed the analysis code to be adapted to work with these components, while the new signals are understood in advance of the large detector's operation.

2.1 DEAP-1

DEAP-1 is a small prototype detector containing 7 kg of LAr in a cylindrical volume. The chamber is made of a $\frac{1}{4}$" thick acrylic sleeve with TPB deposited

in the inside and a reflective coating on the outside. The first two chambers used TiO_2 paint, but the paint was found to be a strong background source and was subsequently replaced with a TPFE sleeve. The sleeve sits in a stainless steel tube fitted with glass windows at either end. The glass windows are also coated with TPB. To ensure low backgrounds from detector materials, a new acrylic chamber has been made for each operational period, with an evolving construction process. The dimensions vary, but the chamber is approximately 28 cm long and 14 cm wide, while the windows are 1 cm thick. Acrylic light guides (20.8 cm long, 14.8 cm wide during the period I studied DEAP-1 data) separate the PMTs from the glass windows. They are used for two reasons; to keep the PMTs from cooling to near cryogenic temperatures, and to help block background neutron radiation. The LAr vessel is housed in a larger stainless steel shell that provides an insulating vacuum, with the light guides and PMTs protruding. A schematic of the detector is shown in Figure 2.1.

The process systems are housed above the detector. The LAr is in a closed system and is liquefied by circulating it through a liquid nitrogen bath. The nitrogen system is not closed and boils off over time. The liquid level of the bath is monitored and nitrogen is refilled as needed. The LAr is 99.999% pure natural argon gas, and initially liquefied in DEAP-1. Impurities from other atmospheric gases, such as oxygen and nitrogen, can absorb scintillation light [102, 103], so the LAr is passed through a SAES getter which reduces impurity concentrations down to less than 0.1 ppb by mass. Additionally a radon trap is installed to remove radon contamination using activated charcoal. The experiment is housed in a steel rack which supports the detector, process systems, and shielding. The LAr chamber is completely surrounded by a water shield comprised of 20 L water containers (cube-shaped boxes). The gaps are filled with plastic boards.

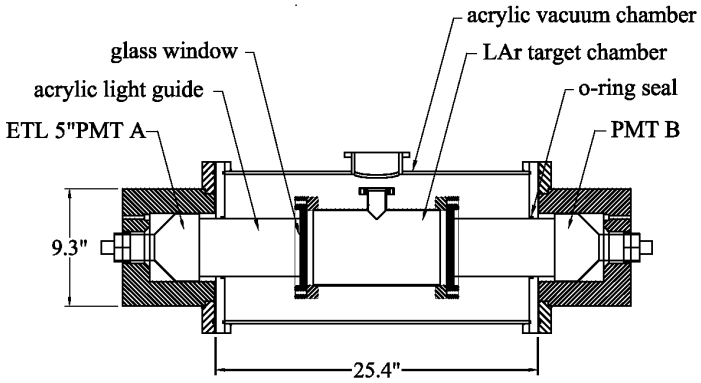

Figure 2.1: A schematic of DEAP-1. Shown is the LAr chamber, external vacuum chamber, light guides, PMTs, and process systems connections.

2.2 Detecting Dark Matter with Liquid Argon

2.2.1 Scintillation from Noble Gases

Scintillation light is produced in certain materials when ionising radiation interacts with electrons or nuclei within it. Electron recoils are dominant since the energy delivered to an electron in a collision is inversely proportional to mass ($p^2/2m$), and the Coulomb attraction being greater for a nucleon. Therefore, an incoming particle's energy is less readily absorbed by electron collisions than those with nucleons, allowing for the rate of electromagnetic events to be up to several orders of magnitude greater than the rate of nuclear recoils, due to the great disparity between their masses[1]. The incoming radiation may excite or ionise the atoms in the scintillating material when passing through, and it may have collisions with electrons or nuclei. When the electrons or nuclei are struck by the incident radiation they recoil through the material and cause others atoms to ionise or become excited.

[1]The mass of protons and neutrons is around 940 MeV, compared to 0.5 MeV for an electron.

Energy deposited in the noble gases causes excited atoms to form dimer pairs (excimers). The excimers are metastable and recombine into stable states with the release of vacuum ultraviolet (VUV) scintillation light [104]. There are two mechanisms through which this occurs. The first is direct excitation, in which an atom is excited and bonds to an un-excited atom (illustrated with argon):

$$\begin{aligned} \mathrm{Ar}^* + \mathrm{Ar} &\rightarrow \mathrm{Ar}_2^* \\ \mathrm{Ar}_2^* &\rightarrow 2\mathrm{Ar} + h\nu \end{aligned} \tag{2.1}$$

The second process is through ionisation, where an ion bonds to another atom and de-excites into a dimer before recombination produces a scintillation photon:

$$\begin{aligned} \mathrm{Ar}^+ + \mathrm{Ar} &\rightarrow \mathrm{Ar}_2^+ \\ \mathrm{Ar}_2^+ + e^- &\rightarrow \mathrm{Ar}^{**} + \mathrm{Ar} \\ \mathrm{Ar}^{**} &\rightarrow \mathrm{Ar}^* + \text{heat} \\ \mathrm{Ar}^* + \mathrm{Ar} &\rightarrow \mathrm{Ar}_2^* \\ \mathrm{Ar}_2^* &\rightarrow 2\mathrm{Ar} + h\nu \end{aligned} \tag{2.2}$$

In Equations 2.1 and 2.2 the term $h\nu$ represents the scintillation photon and the process $\mathrm{Ar}^{**} \rightarrow \mathrm{Ar}^* + \text{heat}$ is non-radiative. Each ionised and excited atom from the incident radiation produces one VUV photon, unless the excimers are destroyed by another process (Section 2.3.1). In the case of noble liquids, these VUV photons do not have enough energy to excite a ground state atom and so the scintillation light is not re-absorbed by the liquid.

The excimer Ar_2^* was observed to undergo recombination in distinct slow and fast components [105]. The Ar_2^* forms one of two distinct states: a singlet, ${}^1\Sigma_u^+$, and a triplet, ${}^3\Sigma_u^+$. It has been shown that the mechanism of energy deposition (linear energy transfer) affects the ratio of ${}^1\Sigma_u^+$ and ${}^3\Sigma_u^+$ states produced. Excitation from β and γ particles produce many more excimers

in the $^3\Sigma_u^+$ state than in the $^1\Sigma_u^+$ state. In the case of argon and neon these states have vastly different lifetimes [106, 107], which form the basis for PSD (Section 2.3).

2.2.2 Argon

While all the noble gases produce scintillation light due to their similar electronic structure, some are more desirable than others for a tonne scale WIMP search. Helium has far too small a nucleus to make effective WIMP detection possible, as WIMP-nucleon recoils would be too rare. It is also much harder to maintain in its liquid form, ^{4}He, which is becoming increasingly rare and expensive. Radon is highly radioactive and its abundance is so low that it is essentially unavailable. Its scarcity is followed by xenon and krypton, which makes them prohibitively expensive, see Table 2.1. Neon is more abundant by an order of magnitude, while argon is a main component of the atmosphere at 0.94% [108].

Property	He	Ne	Ar	Kr	Xe	Rn
Atomic number Z	2	10	18	36	54	86
Abundance (ppm)	5	15.4	9400	1	$\frac{1}{20}$	10^{-15}
Cost ($ per 100 L)	0.09	35.30	0.82	690.00	2000.00	-
Melting point T_m (K)	-	24.6	83.8	115.8	161.4	202.0
Boiling point T_b (K)	4.22	27.07	87.29	119.92	165.10	211.3

Table 2.1: Some basic properties of the noble gases [108]. Abundance refers to atmospheric. Cost and abundance are approximate and may vary considerably.

With helium and radon ruled out, the remaining four noble gases still have potential complications. Argon, krypton, and xenon each have significant amounts of radioactive impurities contaminating even the purest samples. Krypton contains ^{85}Kr, which produces β radiation, and ^{81}Kr, which is a γ emitter. Though its nucleus is considerably massive and much cheaper than xenon, there is too much activity from the radioisotopes contaminating kryp-

ton to make it a suitable candidate for a tonne-scale WIMP search. The lower activity and larger nucleus[2] of xenon offset its higher cost. Xenon is found containing ^{85}Kr while argon contains significant amounts of ^{39}Ar, a γ emitter produced by atmospheric cosmic ray reactions. Neon does not have any naturally occurring long-lived radioisotopes, but has a very small cross section due its much smaller nucleus, which makes it unfavourable for a high-sensitivity WIMP search. However, since it can be made very pure, it has a much better chance of probing the low-mass WIMP sector, which is much harder to obtain with argon and xenon due to their high β and γ activity.

Property	Ne	Ar	Kr	Xe
λ (nm)	77	128	147	174
$^1\Sigma_u^+$ time (ns)	18.2 ± 0.2	7.0 ± 1.0	2.1 ± 0.3	4.3 ± 0.6
$^3\Sigma_u^+$ time	14.9 ± 0.3 μs	1.6 ± 0.1 μs	80 ± 3 ns	22.0 ± 0.2 ns
Scintillation yield ($\times 10^4$ photons/MeV)	1.5	4.0	-	4.2

Table 2.2: Summary of scintillation properties for the primary choices of noble liquids [107, 109–112]. λ is the wavelength of scintillation light produced. $^1\Sigma_u^+$ time and $^3\Sigma_u^+$ time are the length of time it takes for recombination from each state.

The next most important factors for choosing Ar as our target are the properties of the scintillation produced. Primarily, these are the amount of light produced, the difference between recombination of the $^1\Sigma_u^+$ and $^3\Sigma_u^+$ states (for single-phase detectors), and the amount of ionisation produced (for TPC-type detectors). Krypton and xenon have a very small difference between the $^1\Sigma_u^+$ and $^3\Sigma_u^+$ recombination times, which makes them unsuitable for a single-phase experiment since PSD would not be able to achieve levels required for a competitive WIMP search. Table 2.2 contains a summary of scintillation light yields and recombination times for neon, argon, krypton, and xenon in their

[2]It should be noted that the common stable isotopes of xenon have between 74 and 80 neutrons which is comparable to the total mass number of krypton's common stable isotopes (between 80 and 86).

liquid phases.

Thus, Xe and Ar are the best choices for a large scale and competitive WIMP search, while argon is a better choice for single-phase experiments since PSD can be done without the need for a TPC. It is also desirable due its low cost and great abundance. Contamination by ^{39}Ar does present a problem and will be discussed in Section 3.0.2. Both the LXe and LAr programmes have been developing purification techniques to remove the isotopes.

2.3 Pulse-shape Discrimination and Analysis

As shown in Table 2.2, the difference between recombination times for Ar_2^* in the $^1\Sigma_u^+$ and $^3\Sigma_u^+$ states is large enough to perform accurate PSD. The ratio of $^1\Sigma_u^+$ and $^3\Sigma_u^+$ states has been measured for argon and accurate discrimination between nuclear recoils and electromagnetic events has been demonstrated by the DEAP/CLEAN collaboration [77, 111]. In DEAP-1, we are able to distinguish events by studying the ratio of prompt light from an event to the event's total light. Thus ratio is called F_{prompt}. A large fraction of late light from γ and β interactions distinguishes them from nuclear recoils due to neutrons, αs and WIMPs. Example waveforms for both types of events with the regions of prompt and late light highlighted are shown in Figure 2.2.

We use the F_{prompt} ratio as an observable after defining the prompt and late regions of light. The leading edge[3] is the time when the waveform first crosses a threshold of 5 mV (about $\frac{1}{10}$ the pulse height due to a single photoelectron), denoted by t_A and t_B. The prompt region is 150 ns wide, beginning from 50 ns before the leading edge. The amount of light in each region is calculated by integrating the waveform after making baseline corrections: $Q = \int V(t)\,dt$. The charge Q is converted to units of photoelectrons (pe) using a calibration

[3]Code variables Edge0 and Edge1 for each PMT.

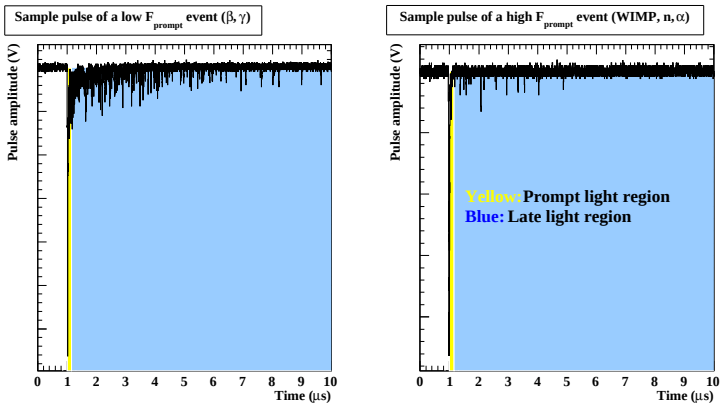

Figure 2.2: waveforms from two events in DEAP-1. The left shows an event with low F_{prompt}, from a β or γ particle. The right shows a high-F_{prompt} event from a nuclear recoil (neutron calibration). The regions of prompt and late light are highlighted.

factor C. We have:

$$F_{prompt} \equiv \frac{\int_{t_A-50ns}^{t_A+100ns} C_A V_A(t)\,dt + \int_{t_B-50ns}^{t_B+100ns} C_B V_B(t)\,dt}{TotalPE} \tag{2.3}$$

where the scripts A and B refer to each of the two PMTs in DEAP-1 and TotalPE is the total light in the pulse, defined as:

$$TotalPE \equiv \int_{t_A-50ns}^{10\mu s-(t_A-50ns)} C_A V_A(t)\,dt + \int_{t_B-50ns}^{10\mu s-(t_B-50ns)} C_B V_B(t)\,dt \tag{2.4}$$

C_A and C_B are determined iteratively while taking data and the range is from 50 ns before the leading edges to the end of the waveform. 4 μs of the tail of waveforms with TotalPE $<$ 200 pe is scanned for pulses crossing a 5 mV threshold. These pulses are integrated over a 25 ns window and the integrals are histogrammed for each run. The mean is determined to be the average charge due to single photoelectrons (SPE) in each PMT, C_A and C_B. Figure 2.3 shows these calibration plots for a typical run. The above definitions are specific to the way the data used in this thesis was analysed. The definition of F_{prompt} can, and should, be generalised. For instance, the current iteration of DEAP-1 uses different integration ranges and new software algorithms are

being developed that attempt to count SPE, thus F_{prompt} would not be defined using integrals.

The region of interest in TotalPE for WIMP activity is between 120-240 pe, or about 40-80 keV_{ee}[4]. We combine this by limiting F_{prompt} to < 0.7 to form a region in which PSD studies focus, a primary goal of DEAP-1 being to demonstrate that the number of electromagnetic events from γs in this region is small. Figure 2.4 shows the distribution of events in F_{prompt}–TotalPE parameter space from ^{22}Na PSD runs taken during the 2007 surface run (described in Section 2.4). Note that the F_{prompt} space occupied by γ events smears out at low energy, this is because the ratio of $^1\Sigma_u^+$ and $^3\Sigma_u^+$ states produced by nuclear and electromagnetic events varies with energy [113].

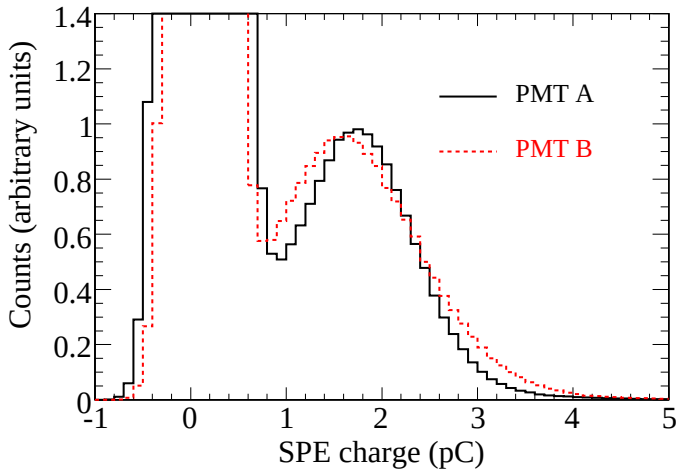

Figure 2.3: The SPE charge spectra for each DEAP-1 PMT from a typical run. The mean is iteratively determined and used to determine the absolute light yield and to calibrate calculations of pulse charge to number of pe [113].

When not taking background data (or performing a WIMP search in the case of DEAP-3600) there are three modes of operation in DEAP-1 that determine analysis parameters and PSD quality. A neutron source is used to

[4]Electron-equivalent energy, see Section 2.3.1

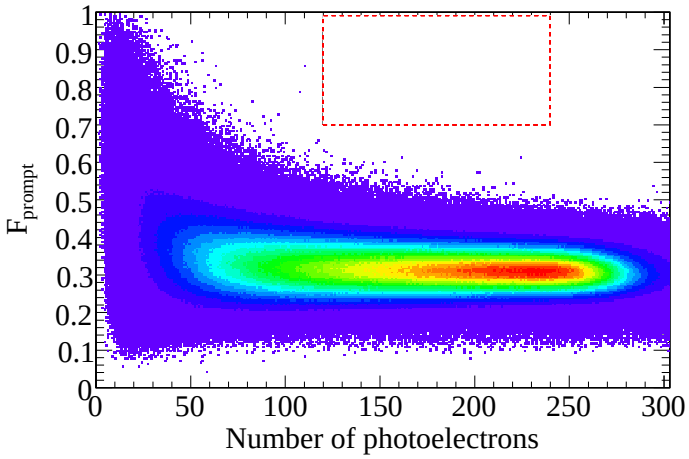

Figure 2.4: F_{prompt} verses TotalPE distribution for triple-coincidence γ events from an ^{22}Na source. The data here is from the 2007 surface run and used to determine PSD capabilities [113].

determine the detector response to nuclear recoils, and an ^{22}Na source is used for energy calibration and PSD analysis.

2.3.1 Scintillation Efficiency

There is a discrepancy between the light yield of nuclear and electromagnetic events. The ratio between the amount of light produced by the two types of event, given that they have the same initial energy, is called the nuclear recoil scintillation efficiency, $\mathcal{L}_{\text{eff}}$. We use an ^{22}Na source for energy calibration which is a γ emitter, so the value we determine is specific to the light yield from electromagnetic events, expressed in keV_{ee}, electron-equivalent energy. To determine the energy of high-F_{prompt}, nuclear recoil events we use the $\mathcal{L}_{\text{eff}}$:

$$E[\text{keV}_{\text{ee}}] = E[\text{keV}_{\text{r}}] \times \mathcal{L}_{\text{eff}}$$

where keV_{r} is the nuclear recoil energy. The energy threshold for WIMP scattering is set by a detector's PSD and the detector material's $\mathcal{L}_{\text{eff}}$. The mechanisms that cause different ratios of $^1\Sigma_u^+$ and $^3\Sigma_u^+$ states, and different

light yields for electronic and nuclear recoils are not fully understood. However, a major factor that contributes to the lower scintillation efficiency of nuclear recoils is quenching, which are processes by which a photon is not produced after a nuclear recoil event. Lindhard quenching is a process where heat is produced instead of the creation of excimers. Another form of quenching is through biexcitonic collisions:

$$Ar^* + Ar^* \rightarrow Ar + Ar^+ + e^-$$

where the result is that two excitons are required to produce a single photon (from the resulting Ar^+).

The LAr $\mathcal{L}_{\text{eff}}$ for neutrons with different energies has been measured by the CLEAN collaboration using a deuterium-deuterium neutron generator. They measured the $\mathcal{L}_{\text{eff}}$ for a range of neutron energies from 10-250 keV_r and found a mean value of 0.25 ± 0.02 for recoils above 20 keV_r [114]. The results are shown in Figure 2.5. Other measurements of much higher energy α particles found a $\mathcal{L}_{\text{eff}}$ for them to be 0.72 ± 0.04 [115, 116].

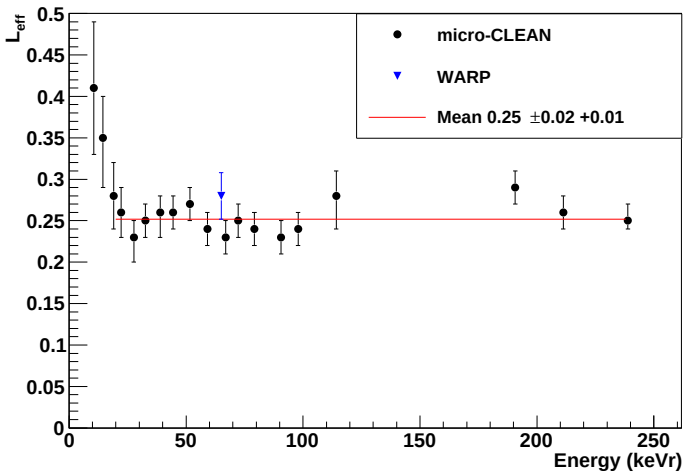

Figure 2.5: $\mathcal{L}_{\text{eff}}$ as a function of recoil energy. The cause of the upturn below 20 keV_r is not known, and the red line is the weighted mean for events above 20 keV_r [114]. Included is a measurement made by the WArP collaboration [117].

2.3.2 ^{22}Na Calibration

511 keV γ rays were produced by an ^{22}Na source for energy calibration and PSD studies. To reduce the background rate while operating on the surface, two NaI detectors were used to trigger the ^{22}Na γ events. The first is a PMT behind the source to collect γ rays travelling backwards relative to DEAP-1, and the second is an annulus-shaped NaI detector surrounding the source that detects additionally produced 1274 keV γ rays. The two trigger detectors combine with DEAP-1 to form a triple-coincidence γ tag. Due to shielding provided by SNOLAB, when DEAP-1 was moved underground a single PMT was used for tagging the 511 keV γ ray from the ^{22}Na source, providing a double-coincidence tag. The calibration varies over time, but is approximately 2.8 pe/keV$_{\mathrm{ee}}$.

2.3.3 PSD Studies

We quantify the level of PSD, or discrimination power, at a given energy as the probability of counting an electromagnetic event as a nuclear recoil in the region of interest. To determine the quality of PSD, ^{22}Na data is taken with the addition of another trigger from a single-channel analyser (SCA). This cuts the majority of events which have energies well above the region of interest (120-240 pe). The cut decreases dead time and allows more events in the region of interest to be collected in a shorter time. The PSD quality is checked by selecting all good events (see Section 2.3.4) that pass the coincidence cuts and studying the $\mathrm{F_{prompt}}$ results. Additionally, neutron calibration data has been used. The PSD is accurate if tagged electromagnetic events from the 511 keV γ rays do not impinge on the $\mathrm{F_{prompt}}$ region occupied by tagged neutron events from calibration. While the detector was operated on the surface 63 million triple-coincidence events were collected. Only 16.7 million survived the data cleaning cuts and had energies within the region of interest. None had

$F_{prompt} > 0.7$, resulting in a demonstrated discrimination power of 6.8×10^{-8} [113]. The results of the surface run are shown in Figure 2.6, which includes tagged neutron events. Once DEAP-1 was moved to SNOLAB a primary goal was to build a large dataset to study the PSD level. By the end of the first two underground runs the PSD level was pushed down to $9.26 - 9.46 \times 10^{-9}$ [118, 119].

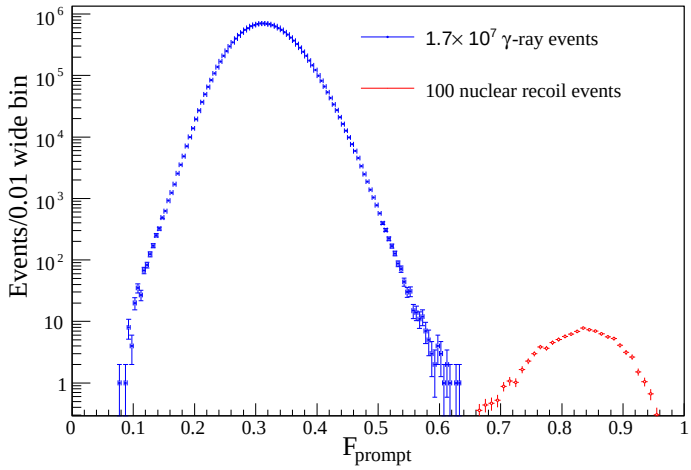

Figure 2.6: F_{prompt} distribution of PSD events from the surface run. There are no electromagnetic events in the nuclear recoil region.

2.3.4 Additional Variables and Data Cuts

This section introduces additional variables that are used in later analysis. The primary variables I used in my background studies are F_{prompt}, TotalPE, and Zfit. The Zfit variable is an approximate measure of an event's position, based on the amount of light collected by each PMT. We can use this variable to restrict events to those occurring in the LAr volume. Zfit is calculated as:

$$\text{Zfit} \equiv 35.2 \text{ cm} \times \frac{\int_{t_A-50ns}^{10\mu s-(t_A-50ns)} C_A V_A(t)\, dt - \int_{t_B-50ns}^{10\mu s-(t_B-50ns)} C_B V_B(t)\, dt}{\text{TotalPE}} \quad (2.5)$$

where 35.2 cm is the distance from the middle of the LAr volume to the faces of the PMTs. This variable acts differently during each period due to changes in

the detector surfaces and light guides. When DEAP-1 was first underground the Zfit position of background events was centred around 5 or 6 cm with more light coming from the detector centre than the ends. Optical effects due to the change in reflectivity were observed when the TPFE sleeve was used in place of the TiO_2 paint. A Zfit calibration was undertaken showing a strong correlation between Zfit = 0 and event positions in the detector centre. It also showed that position reconstruction degraded at Zfit = $\pm$ 10 cm, which is near the light guides. However, a dependence on light yield and Zfit was found, which must be corrected during analysis.

Additional variables are used for the data cleaning cuts listed in Appendix A. These cuts remove "bad" events, which may have strange pulse shapes. The variables PreSignal0 and PreSignal1 ensure that there are no pulses before the prompt light. PmtCutID0 and PmtCutID1 prevent waveforms with multiple signals (pile-up) from being selected. The primary cut is on timing, ensuring that the prompt pulses in both waveforms occur within 20 ns of each other and within 30 ns of the mean prompt pulse time. This is done using the trigger time mentioned in Section 2.3, Edge0 and Edge1.

2.4 Detector Operations

The DEAP-1 detector is currently in its fourth operational period. During each period the detector is run continuously, always taking data. It alternates between modes: background, ^{22}Na calibration, neutron calibration, and PSD studies. The data are organised in run numbers with subruns, which are now incremented automatically based on file size and run length. Run numbers can also be incremented by an operator for work purposes or when changing modes. Waveforms are digitised and recorded on computers located in the underground lab, then sent off-site for automated analysis and moved to servers where they can be accessed by the collaboration.

The first operational period was a surface run at Queen's University from August to October, 2007. This run was used to test the detector and demonstrate PSD. DEAP-1 was moved underground at SNOLAB to continue PSD studies in a low-background environment, and to study the background sources on site before construction of DEAP-3600. Between each subsequent operational period the detector was modified, building on the lessons learned during the previous period. For each period a new acrylic chamber was constructed with increasingly refined methods. Large changes involved using a new radon-free glove box (beginning in 2009), work to ensure low levels of radon and polonium contamination, new methods of depositing TPB, and procurement of different materials.

The first underground run took place between July and December 2008 and ended in order to attempt to reduce backgrounds by building a new chamber. A radon trap was installed to further purify the LAr during cool-down. DEAP-1 went cold again in March 2009 and ran until December 2009. The analysis presented here focuses entirely on the 2008 run and the first half of the 2009 run. During these periods some background data were collected with a lower voltage supplied to the PMTs to increase the sensitivity to large light events, such as high energy α particles, which otherwise saturate the PMTs. In June, 2009, a new DAQ system was installed, replacing the oscilloscope. CAEN digitisers using a VME bus were installed and controlled with a computer running the MIDAS software from TRIUMF, which will be similar to the DAQ for DEAP-3600. The third underground run began in March 2010 and DEAP-1 is currently still operational. This phase saw the introduction of new acrylic light guides and the 8" Hamamatsu R5912 PMTs that will be used on DEAP-3600. When the 2010 run ends, DEAP-1 will be removed from the SNO+ control room and installed in the J-Drift, part of the new development at SNOLAB.

2.5 DEAP-3600

The DEAP-3600 detector uses the same principles as DEAP-1, but has significant changes in structure and electronics. It is imperative that as we move to the tonne scale we continue to improve the PSD level and reduce the sources of background radiation. Much of the current work within the collaboration is to this effect. For example, the electronics on DEAP-1 have been adapted to match DEAP-3600, and an intermediate detector is being constructed to understand the data when multiple PMTs and a spherical geometry are used (although it is being primarily developed to test several engineering aspects). Additionally the source of argon will be changed from atmospheric to underground, where much less ^{39}Ar is present

The 3600 kg LAr target will be contained in a spherical acrylic vessel that will be machined at the University of Alberta. The inside surface will be polished to maximise optical transparency and a layer of TPB will be deposited as in DEAP-1. A resurfacer is being developed to remove the TPB and a layer of acrylic, which becomes contaminated with radon when exposed to air. On the top of the sphere a long neck will hold the refrigeration system made with a helical heat pipe filled with liquid nitrogen. The LAr that boils off will rise through outer channels in the neck and encounter the heat pipe, liquefy and return through the centre. The centre will accommodate the resurfacer and allow us to deploy calibration sources through a glove box. Both systems will be closed, as maintaining a large enough supply of nitrogen to cool this amount of LAr is un-feasible if allowed to boil-off as in DEAP-1.

Figure 2.7 shows the complete DEAP-3600 detector. The outside of the acrylic vessel will have a pattern of stubs machined in it, protruding 2 cm from the surface. We will affix acrylic light guides to these, either with clamps and an oil interface, or with a glue joint made of acrylic polymer. Both methods

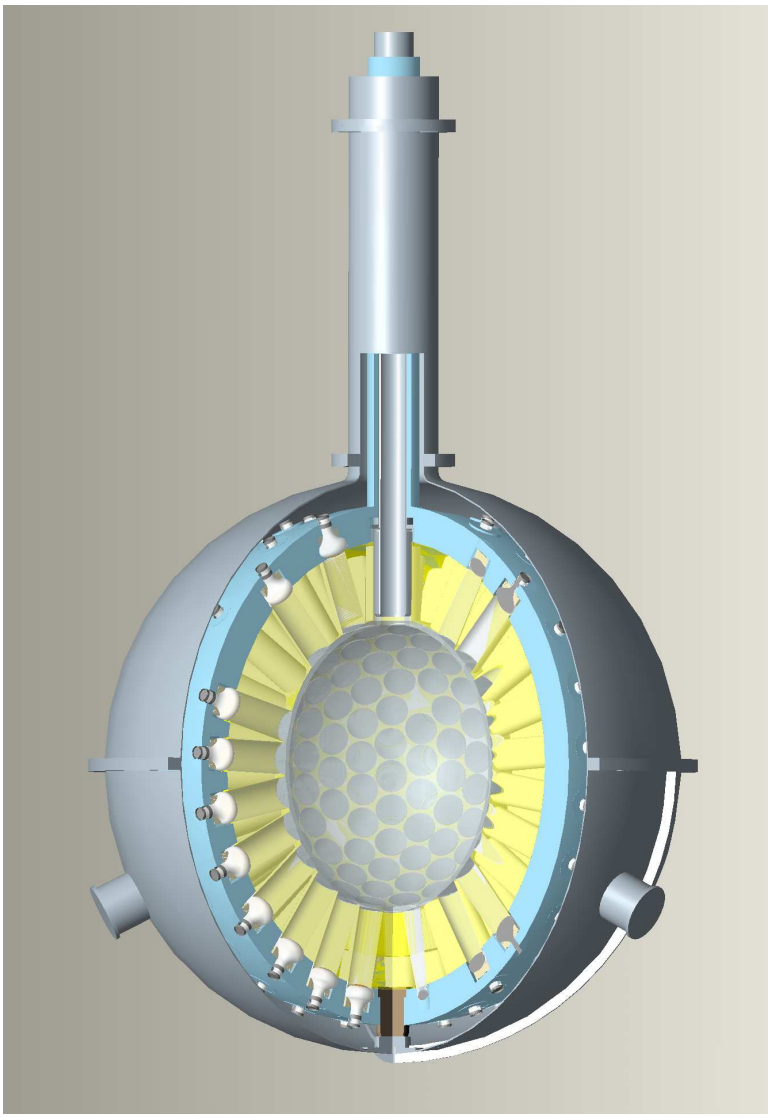

Figure 2.7: Engineering drawing of the completed DEAP-3600 dark matter experiment. The LAr target is in the centre, acrylic light guides and insulation is yellow, insulating foam is blue. The neck and stainless steel vacuum vessel are shown. The protrusions from the shell and brown piece at the bottom of the vessel are supports to aid in construction.

are being extensively researched. The light guides are needed to attenuate neutrons from the PMTs. The volume will be surrounded by 266 Hamamatsu R5912 PMTs. The outer surface of the vessel will be coated with a reflector and the light guides will be covered in an aluminised mylar foil to reflect any light not incident on the PMTs. The area between the light guides will be filled with pieces of acrylic to block neutrons, while the areas surrounding and above the PMTs will be filled with foam for thermal insulation. The entire vessel, PMTs, and neck will be insulated and enclosed in a stainless steel shell.

DEAP-3600 will be suspended from a stainless steel deck in a water tank with an active muon veto (PMTs in the water watching for Cherenkov radiation). The deck will be used as the main base of operations, having access to the process systems and supporting a gantry crane and glove box for deploying sources and maintenance. The project will be located in the newly excavated, and recently clean certified, Cube Hall at SNOLAB. MiniCLEAN will be situated next to DEAP-3600 in its own water tank, but sharing the deck. The deck and infrastructure have been installed, while the water tank and outer vessel of MiniCLEAN have been delivered. Using depleted argon, DEAP-3600 will be able to push the sensitivity of a WIMP search down to a scattering cross section of $10^{-46}\,\mathrm{cm}^2$ for a 10^2 GeV WIMP, as seen in Figure 2.8.

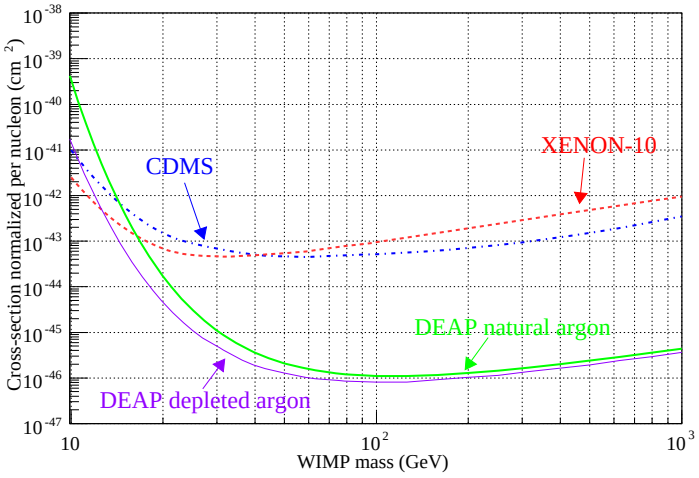

Figure 2.8: Projected WIMP search sensitivity for a single phase LAr detector of our size [113]. This plot shows the increase in sensitivity gained from using depleted argon which improves PSD and reduces dead time. The current experimental limits from XENON10 and CDMS are shown.

Chapter 3

Analysis of Alpha Backgrounds in the DEAP-1 Detector

Understanding and reducing the backgrounds affecting PSD in DEAP-3600 is a primary analysis task. I studied high-energy α particles in an attempt to understand their source and their nature. I was able to confirm that they are from the decay chain of ^{238}U whose daughters can be found on detector materials and in the argon gas. Methods to build cleaner argon chambers and to purify the argon gas were developed, and the levels of the α background have been reduced significantly. These techniques will be applied to the construction and operation of DEAP-3600. The following sections describe the different backgrounds present at SNOLAB and present the analysis.

3.0.1 Alpha Particles

Due to the large size and charge of these particles they have a high-F_{prompt} and can be mistaken for WIMP recoils. Since they generally have very high energy they will not cause as much trouble as neutrons, but they are accompanied by recoiling nuclei and it is important to understand how many of this type of event to expect. We are taking care to reduce them since they cause deadtime and can reduce the sensitivity of a WIMP search by reducing the PSD power. The decay chains of ^{238}U and ^{232}Th are the primary source of high-energy α

radiation, while also producing β and γ particles. Their daughters are very common in metals, so construction materials for the detector are carefully selected and the specific activity of each component is counted. The decay chains of ^{232}Th and ^{238}U are shown in Figures 3.1 and 3.2, respectively. α backgrounds travel a very short distance in matter, since they are very likely to collide with other particles and lose energy. Therefore, for analysis purposes we are mostly concerned with sources that are immediately incident on the LAr. In DEAP-1 this is the acrylic chamber and the LAr itself. For design purposes, αs can create neutrons via (α,n) reactions, discussed in Section 3.0.4, so care is taken when constructing new chambers to ensure clean materials and minimal contact with air. DEAP-3600 will be able to remove a layer of radon contaminated acrylic with the resurfacer. In argon the amount of contaminants is independent of the argon purity; they come from the steel and other metals that are used to process and store the argon. Because of this the entire process system must be kept clean and made with radiopure components. A radon trap was developed for DEAP-1 that manages to reduce the amount of radon contamination before the argon enters the process systems and the detector. The most common α emitters are from the ^{222}Rn decay chain and are short lived, with initial amounts decaying away quickly. This suggests that the radon contamination enters DEAP-1 from the storage bottles and cannot be maintained inside the argon chamber. Unfortunately, some daughters are long-lived and provide a constant source of background. Worse still, when the atoms undergo an α decay they may eject the heavy nucleus into the argon, which will be seen as a lower energy, high-F_{prompt} event, which can mimic a WIMP recoil and fall into the region of interest. This is the case when the decay parent is stuck on the detector walls, sending the daughter nucleus into the argon and the α deeper into the acrylic, avoiding identification. If the parent is embedded within the detector materials, such as TPB, then the α may enter

the LAr with reduced energy and appear WIMP-like. The DEAP-3600 LAr volume will be fiducialised and events occurring too near the walls will be removed. This analysis studies these types of events and was followed by the installation of the radon trap.

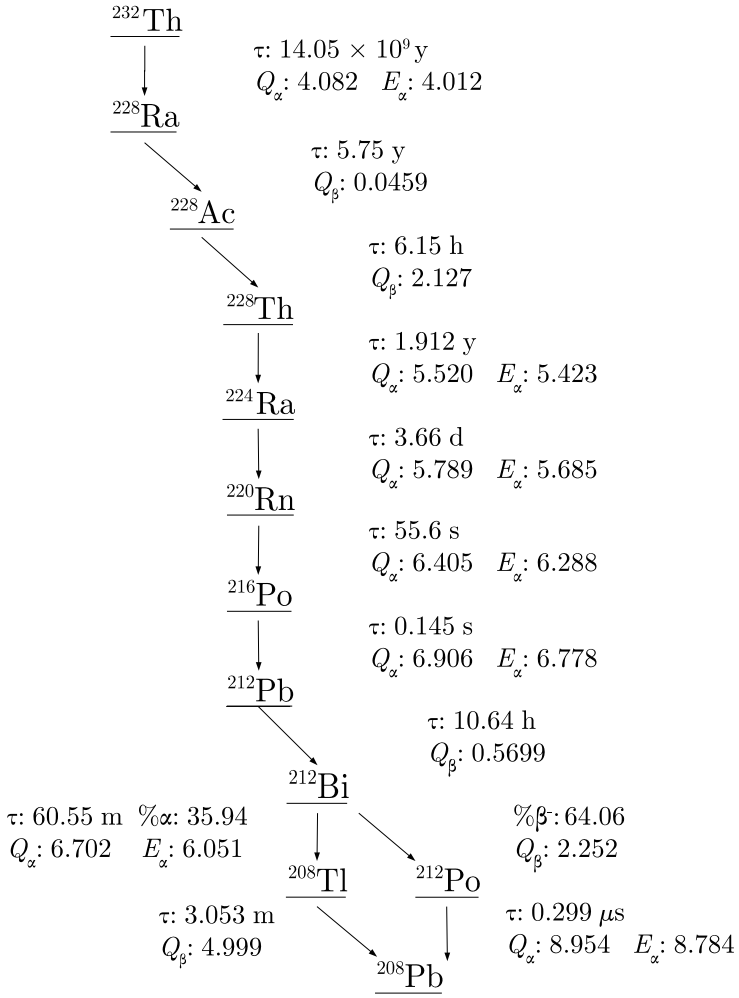

Figure 3.1: The decay chain of ^{232}Th. Shown are the half-lives, τ, the Q-values of beta and alpha decays, and the alpha-energies, E_α. Data received from the National Nuclear Data Center (NNDC) [120–125].

3.0.2 Beta and Gamma Radiation

β and γ radiation are produced by the same decay chains as α radiation where the sources are the rock walls and material impurities. Signals due to both

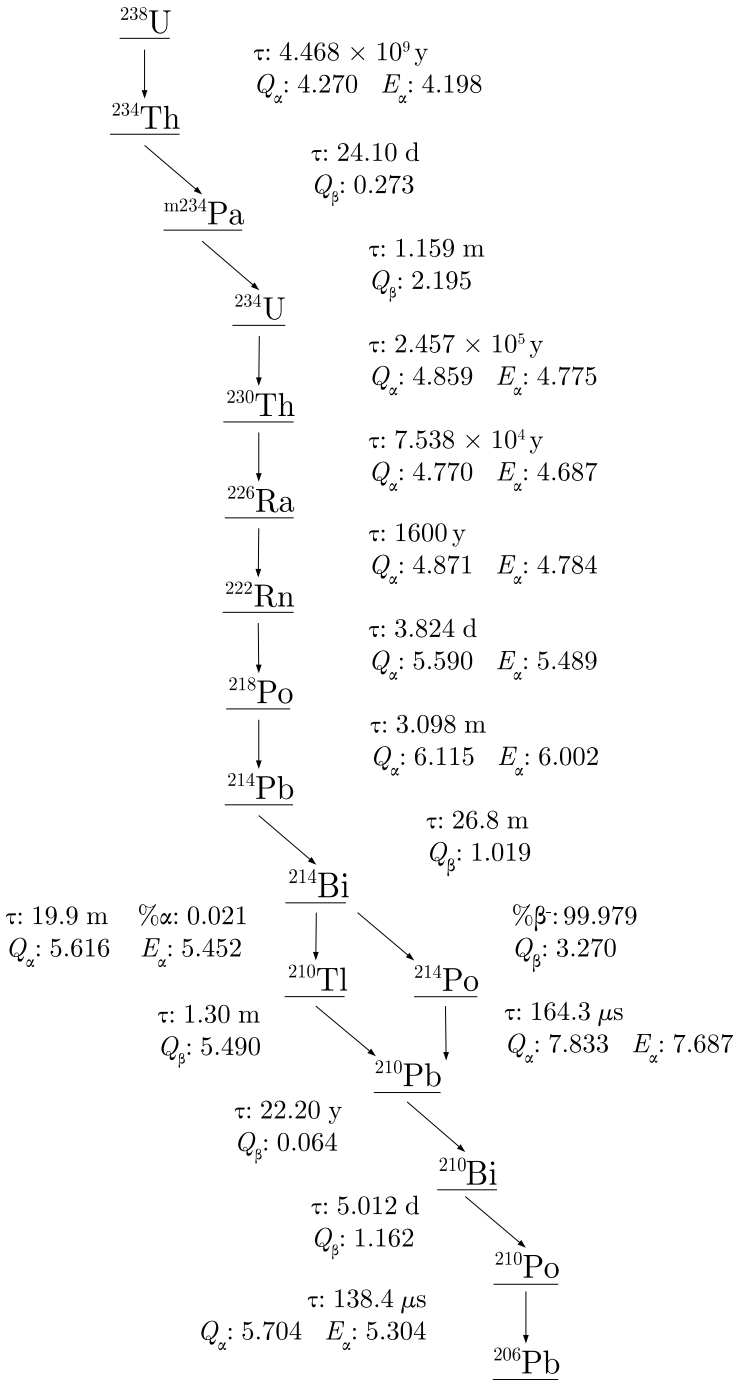

Figure 3.2: The decay chain of ^{238}U. Shown are the half-lives, τ, the Q-values of beta and alpha decays, and the alpha-energies, E_α. Data received from the National Nuclear Data Center (NNDC) [126–133].

types of radiation can be removed using PSD, but care is taken to reduce these events as they degrade the WIMP sensitivity and detector livetime. The water shield surrounding DEAP-3600 will be able to block β and γ particles and the active veto system will be able to tag the cosmic backgrounds. Components inside the water shield will have to be made as radiopure as possible and remaining events will have to be dealt with using PSD (and the acrylic shielding in the case of βs).

An additional source of β radiation is ^{39}Ar. This isotope is produced in the atmosphere by interactions with high-energy cosmic rays (neutron capture). Natural argon has a specific activity of ≈ 1 Bq/kg and a half-life of 269 years [134]. This gives argon a background rate of $\approx 10^7$ events/keV/100 kg argon per year, and the discrimination power against electronic recoils must be greater than that. DEAP-3600 will use argon that is depleted in $^{39}39$ to reduce the number of these events. Since ^{39}Ar is cosmogenically activated, underground sources of natural gas and CO_2 have been found that contain significantly reduced ^{39}Ar activity than atmospheric sources. Research into finding sources, developing extraction techniques, storing, testing, and transporting the depleted argon have been carried out by the DEAP/CLEAN and WArP collaborations and production agreements have been made to supply all three experiments with isotropically depleted argon [135, 136].

3.0.3 Atmospheric Muons

High energy cosmic rays produce muons when they interact with the atmosphere, which are a type of ionising radiation able to penetrate deep into the earth. Atmospheric muons produce two effects in DEAP. They can create Cherenkov radiation in the light guides, which may be removed during analysis using the Zfit calculation. To reduce their effect, the light guides have been doped with a UV absorber. Muons also carry enough energy to pro-

duce neutrons from detector materials through spallation. The experiments are shielded by the rock overburden granted by locating them at SNOLAB. SNOLAB has the lowest muon flux of any lab currently in operation due to its depth and high density rock. Figure 3.3 shows a comparison of other underground sites. To further reduce backgrounds from atmospheric muons the water shield that completely surround DEAP-3600 will have an active veto system. When muon pass through the shield and enter the detector they will produce Cherenkov radiation in the water which will be collected by an array of PMTs which will veto the event.

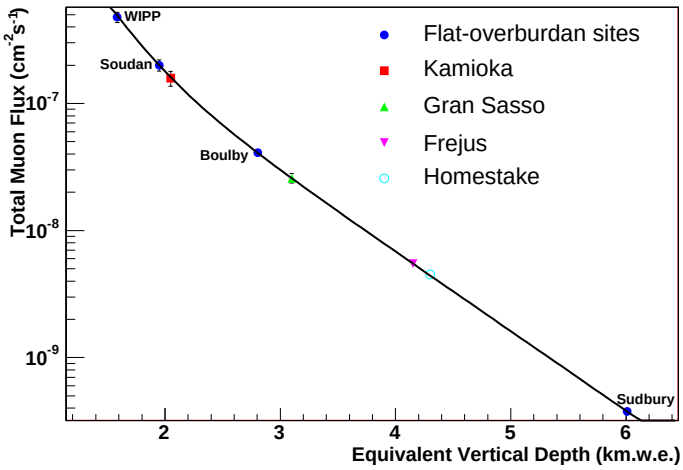

Figure 3.3: Comparison of depth and muon flux for various active underground facilities. Due to differences in the rock overburden, the depth is normalised to water equivalent units to account for variations in density.

3.0.4 Neutrons

These are the most troubling background since they will mimic the high-$F_{prompt}$of a WIMP signal. The design goal of DEAP-3600 is to have zero neutron events. The primary method of accomplishing this is through shielding and the active veto. Neutrons from external sources, such as the deck steel and rock walls, will be blocked by the water shield, while those produced by

atmospheric muons will be blocked and vetoed. Neutrons created by muons in components inside the water shield will be vetoed. However, there is another source of neutron production: (α,n) reactions. These are troubling since they cannot be completely removed. DEAP-3600 will use great amounts of acrylic shielding to prevent neutrons from (α,n) reactions in detector materials from reaching the LAr. Studies were done at Queen's University to measure the attenuation length of (α,n) neutrons and predict the absolute stopping length of acrylic, thus, DEAP-3600 will have about 22" of acrylic between the LAr and the steel shell and electronics. The PMTs produce the most neutrons with their borosilicate glass and will be faced against the light guides. Neutrons created by the stainless steel vessel and the metal components of the cables, bases, and PMTs will be blocked using acrylic inserts between the light guides. Monte Carlo studies are being done to study the likelihood of neutrons reaching the LAr through air gaps.

3.1 Analysis of High-Energy α Backgrounds in DEAP-1

While α radiation is indistinguishable from nuclear recoils using PSD alone, event position reconstruction and energy calculation will allow us to discriminate accurately. This analysis uses these tools to study high-energy α radiation from the ^{222}Rn decay chain. The goals of this study were to determine the sources of the αs so they could be reduced and to see whether ^{222}Rn daughters concentrate on the detector walls. In November, 2008, we did not recover properly from a mine-wide power outage. Upon restoring power our slow controls (process systems, temperature, and pressure monitors) malfunctioned and the liquid level of the nitrogen cooling bath was misrepresented. The result was a boil-off of the LAr which escaped the detector through safety valves under the increased pressure. After stabilising and taking data to check its consistency,

the argon in DEAP-1 was topped up to maintain the maximum target mass, and a burst of α activity from ^{222}Rn was introduced into DEAP-1. We had been studying αs prior to this event, so we were able to identify the peaks in the energy spectrum quickly. ^{222}Rn contamination comes from argon, as it is present in the argon gas's source and transportation materials. We know it is not supported by the detector since the initial activity decayed away in a matter of days. The data collected gave us a unique circumstance to attempt to distinguish the energy spectra of α radiation from short-lived ^{222}Rn daughters originating in the LAr and those from other background sources. This analysis focuses on background data collected from August, 2008, until just after the argon top-up in November. For this study we supplied the PMTs with a lower voltage than normal operation to ensure that the high energy α particles do not saturate the PMT electronics.

^{222}Rn decays quickly through ^{218}Po and ^{214}Po producing three α particles. The final α decaying isotope is ^{210}Po (138 days) which is supported by ^{210}Pb with a much longer half-life (22.3 y). The initial amount of ^{222}Rn decays away quickly ($\approx$3 d) and this analysis looks closely at the daughters. The hypothesis is that the short-lived daughters will be distinct from the long-lived ^{210}Po, which will end up concentrated on the surface of the detector walls. When a ^{210}Po on the surface decays the α will either travel away from the wall, through the argon and be detected, or it will burrow further into the wall and the Po nucleus may move into the argon, causing nuclear recoils. This is a serious problem, as the recoiling nucleus from a decay may interfere with the WIMP region of interest.

Before the November 2008 argon top-up, the energy spectrum of the background could be described by a linear combination:

$$\frac{dN_{Bg}}{dE} = \frac{dN_{Bg}^{Rn222}}{dE} + \frac{dN_{Bg}^{Po218}}{dE} + \frac{dN_{Bg}^{Po214}}{dE} + \frac{dN_{Bg}^{Po210}}{dE} + \frac{dN_{other}}{dE} \qquad (3.1)$$

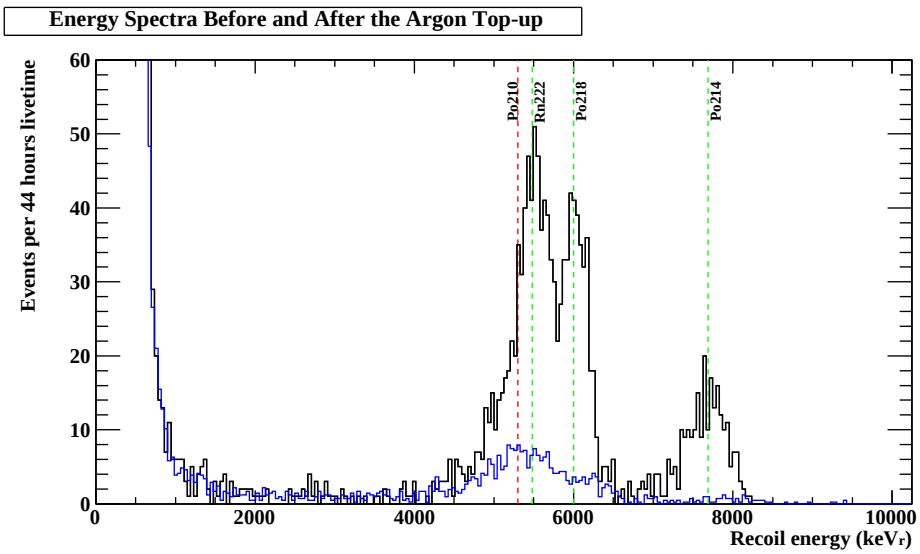

Figure 3.4: Energy spectra of high F_{prompt} events in the DEAP-1 detector during low-voltage background runs taken during the 2008 underground run. The blue line is the normalised spectrum before the boil-off event, Equation 3.1, and the black line is from shortly after and is dominated by ^{222}Rn, Equation 3.2.

Each term represents the number of event counts per energy bin due to each α source: ^{222}Rn and its short-lived daughters, ^{210}Po, and all other backgrounds. This is compared to the data taken within days of the argon addition, so we treat the long-lived ^{210}Po (supported by ^{210}Pb with a 22 yr half-life) as unaffected by the top-up. After the top-up we describe the total backgrounds in the detector from all sources as:

$$\frac{dN_{Bg}}{dE} = \frac{dN^{Rn222}_{top+Bg}}{dE} + \frac{dN^{Po218}_{top+Bg}}{dE} + \frac{dN^{Po214}_{top+Bg}}{dE} + \frac{dN^{Po210}_{Bg}}{dE} + \frac{dN_{other}}{dE} \qquad (3.2)$$

Both spectra are shown in Figure 3.4. The blue line contains good events (Appendix A) with $F_{prompt} > 0.6$ from all of the low-voltage background runs in the 2008 data, before the boil-off. The run is normalised to the livetime of the background runs taken shortly after the argon was refilled, which is the black line. At low energy, leakage from electromagnetic events can be seen. Within a few days the low-voltage background spectrum returned to the levels seen before the top-up, a strong indication that the peaks are from short-lived

^{222}Rn. A list of runs used in the analysis is in Appendix B.

Since the backgrounds in the detector from sources other than ^{222}Rn will be equivalent in both cases, we take the difference of the two energy spectra to remove them. The remaining events should only be those due to ^{222}Rn and its short-lived daughters:

$$\frac{dN_{Rn}}{dE} = \frac{dN_{top}^{Rn222}}{dE} + \frac{dN_{top}^{Po218}}{dE} + \frac{dN_{top}^{Po214}}{dE} \tag{3.3}$$

Figure 3.5 is the energy spectrum in DEAP-1 from only the short-lived daughters of ^{222}Rn(Equation 3.3). It shows that the peaks representing αs from the decay of ^{222}Rn and ^{218}Po are now nearly equal in height and that the ^{210}Po peak shows less contribution.

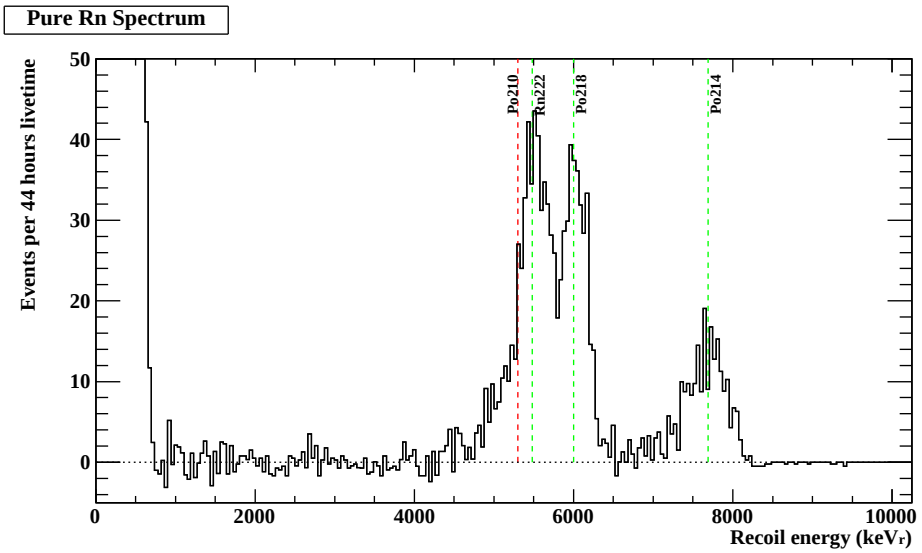

Figure 3.5: Energy spectrum after subtracting the top-up radon spike from the pre-boil-off background data, Equation 3.3 = 3.2 - 3.1. This spectrum is composed of only the αs from ^{222}Rn and its short-lived daughters.

An important clue to the nature of the radon contamination is the difference between the ^{214}Po peak and that from ^{222}Rn and ^{218}Po. The smaller ^{214}Po peak was integrated and compared to the combined peaks from ^{222}Rn and ^{218}Po. The ratio between them was found to be 3.9 ± 0.5; there is only one

^{214}Po decay for the two decays from ^{222}Rn and ^{218}Po decay. This is consistent with the hypothesis that the radon contaminants originate in the LAr and move to the walls of the detector. The ^{222}Rn in the LAr would be mostly non-reactive and uncharged, able to diffuse freely through the liquid and, therefore, we detect all of its decays. Its daughters, however, are likely to be charged and attracted to surface materials. A factor to explain the differences in peak height is the lifetimes of the daughters. ^{218}Po has a half-life of only three minutes, so it would remain close to its parent. Some may have reached the walls in that time, and its peak is smaller than that of ^{222}Rn. The ^{214}Po, however, will last for a much longer time due to the intermediate ^{214}Pb, with a 30 minute half-life, giving it time to diffuse to a surface and remain there. This tells us that background from long-lived daughters, ^{210}Po, will be dominated by activity on detector walls.

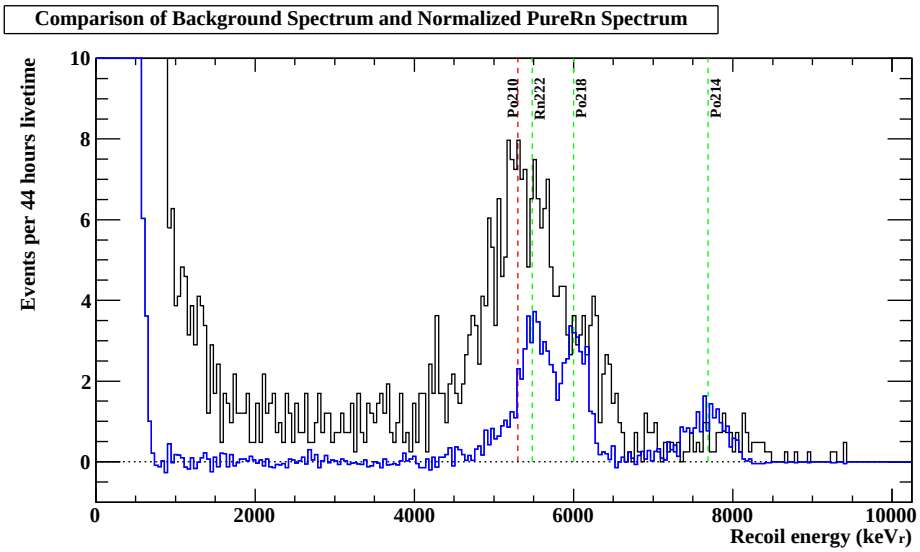

Figure 3.6: The background spectrum from before the boil-off is shown in black while the pure radon spectrum is in blue. This image comparatively shows the differences between the two spectra after normalisation.

Using the spectrum due purely to ^{222}Rn and short-lived daughters, we can probe the constant backgrounds present in DEAP-1 that are less well under-

stood: ^{210}Po and the other high F_{prompt} events. This spectrum was normalised by comparing the integrals of the outlying ^{214}Po peaks and then subtracted from the background data taken before the boil-off, described by Equation 3.1. The result is:

$$\frac{dN_{diff}}{dE} = \frac{dN_{Bg}^{Po210}}{dE} + \frac{dN^{other}}{dE} \tag{3.4}$$

A comparison of the background spectrum and the normalised pure radon spectrum is shown in Figure 3.6 while the result of the subtraction is shown in Figure 3.7. The result has a wide peak suggesting alpha interactions with variations in light yield. The over-subtraction visible in Figure 3.7 was believed to have been due to small shifts in energy between data collection runs. Work on improving energy calibration has been carried out and will be discussed in Chapter 4 where this analysis is revisited to test this hypothesis. All events at lower energies are left unchanged, and must not be related to the ^{222}Rn α decays. Separating the signals due to radon α decays is successful and we see that ^{210}Po may be treated as a distinct and constant background source.

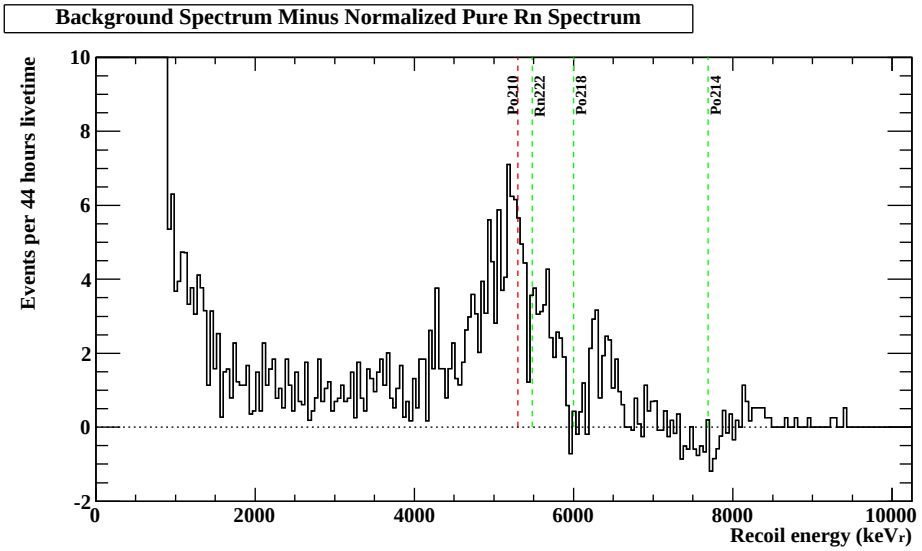

Figure 3.7: The result of subtracting the pure radon spectrum (Equation 3.3) from the background spectrum before the boil-off (Equation 3.1). The result is described by Equation 3.4. Over-subtraction is visible in some regions.

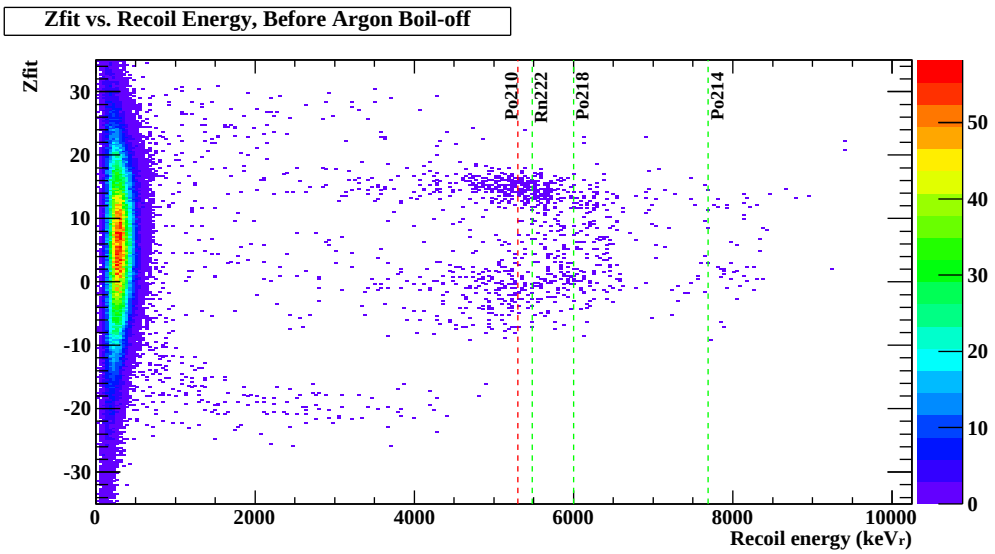

Figure 3.8: The Zfit versus recoil energy of the high-F_{prompt} events described by Equation 3.1 and shown in Figure 3.4. Band-like structures appear in the light guides at low energy and near the ends of the argon volume at all energies.

To probe the nature of the remaining events (especially between 1.5 and 4 MeV) we look to position reconstruction using Zfit. Due to variations in the reflective surface and the difference in efficiency of each PMT the detector centre lies at $5 \sim 6$ cm, while the windows are near -6 cm and 16 cm, and the light guides extend an additional 15 cm. The data described by Equation 3.4 was divided into regions of distinct energy and the Zfit of each region was studied. A plot of Zfit versus energy for the background events before the boil-off is shown in Figure 3.8. Structure formations are immediately visible, with events near the α energies forming bands at the windows, and lower energy backgrounds forming bands in the light guides and on the windows. The Zfit distribution of events for the pure radon spectrum, Figure 3.9, shows that the events due to ^{222}Rn and its short-lived daughters occur in the bulk of the argon, with a small dependence on the location of the windows. The Zfit distribution in Figure 3.10 is of events in the ^{210}Po peak, Equation 3.4. The Zfit distributions both before and after subtracting the pure radon backgrounds are

shown and we can see that ^{210}Po accumulates at the detector windows more than the detector centre. Events outside of the bulk are mostly unaffected by the subtraction. This may be due to a higher attraction from the glass than the acrylic (both surfaces are coated in TPB), or to a constant external electric field, which may account for the difference in the number of events at each window. Only the latter will be observed in DEAP-3600.

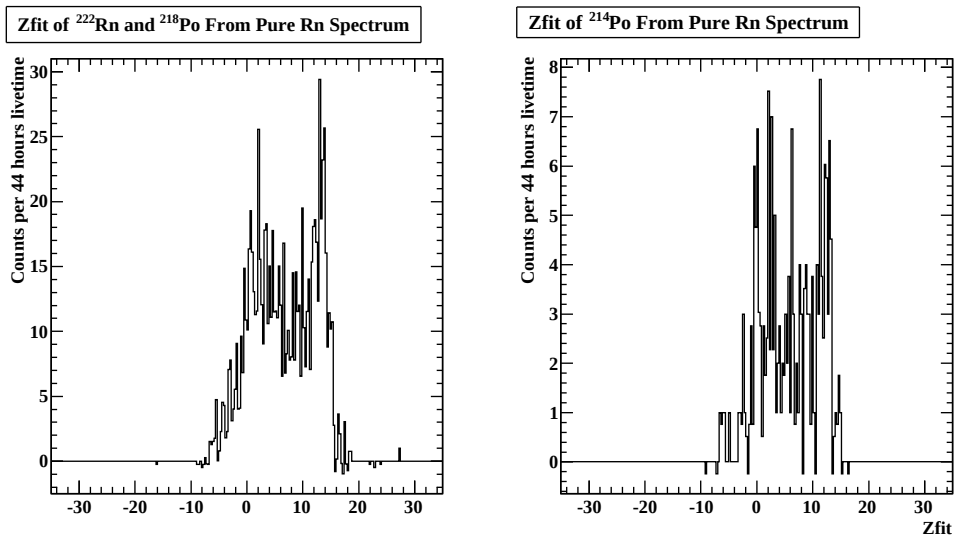

Figure 3.9: The Zfit distribution of events for the two peaks in Figure 3.5. The peak due to ^{214}Po and that due to ^{222}Rn and^{218}Po both show a concentration of events in the argon bulk.

The lower energy events, between 1.5 and 4 MeV accumulate in distinct regions, as shown in Figure 3.11. A significant number of events occur at the interface between the PMTs and the acrylic light guides. Their source has not been identified, but they do not interfere with WIMP studies because of their position. A Zfit dependence, as was found in the 2009 data, is not responsible for the events near the window because this behaviour is unique to high F_{prompt} events. Furthermore, the pure radon data shows that these events are largely centred in the chamber, with some drift towards the ends. The events beyond $\pm$15 cm may be due to Cherenkov light in the light guides or

scintillation from air, and it may be due to PMT noise. The events external to the bulk persist in 2010 operations, while Zfit behaves differently due to modifications made to the detector.

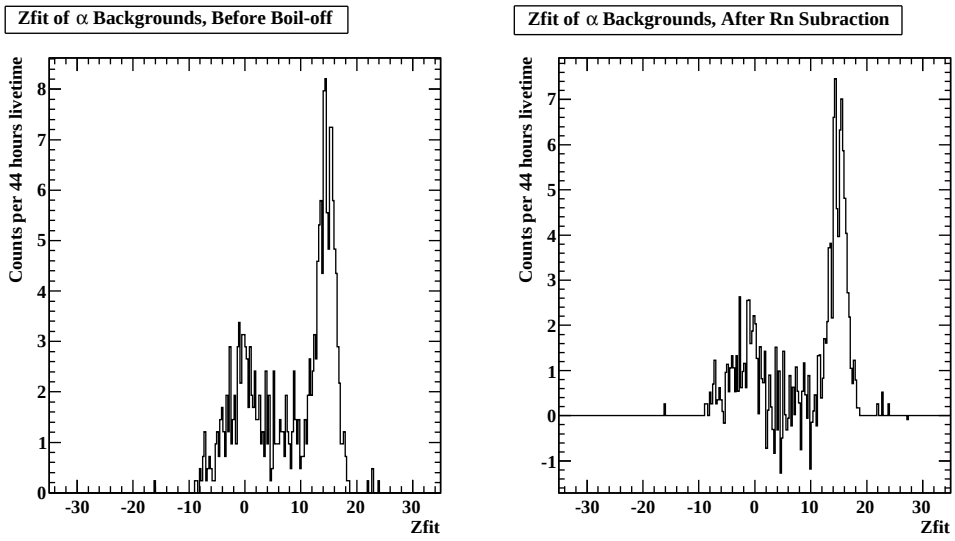

Figure 3.10: The Zfit distribution of events in the main α background peak. The plot on the left shows events from the background spectrum, Equation 3.1 and Figure 3.4, and the plot on the right shows the events to long lived ^{210}Po and other backgrounds, described by Equation 3.4 and shown in Figure 3.7. The pure radon spectrum has a negligible effect on events in this energy region.

3.2 Closing Remarks

This analysis successfully demonstrates that we can distinguish signals from ^{222}Rn and its short-lived daughters from the long-living ^{210}Po and the ^{210}Po may be treated as a distinct, constant background source. As a result, construction of new chambers focused on limiting the amount of ^{210}Po on the surfaces, and an activated charcoal trap was developed to prevent ^{222}Rn from argon sources from entering the chamber. High energy α backgrounds were reduced by a factor of 10, confirming the results of this study and confirming the hypothesis regarding the source of radon contamination. DEAP-3600 will have the ability to clean and resurface the inner detector walls, allowing built-up α

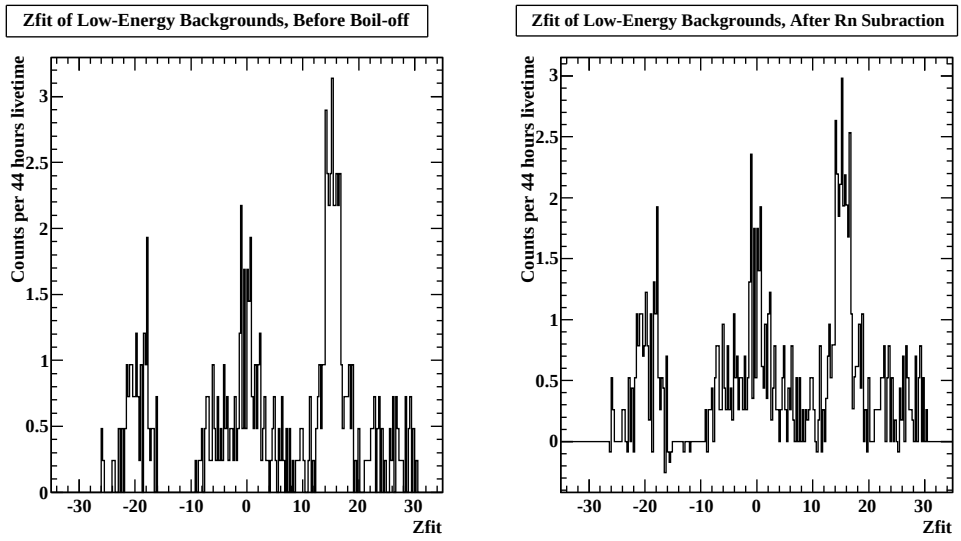

Figure 3.11: The Zfit distribution of lower energy events, between 1.5 and 4 MeV. The distinction between the left and right plots is the same as in Figure 3.10. Only events inside the argon bulk are affected.

sources to be removed. In the following chapter this analysis will be revisited after studying ways to make corrections to the energy calibration which was seen to drift over time during this work. These corrections will allow for more accurate calculations using the energy spectra presented in this chapter, and energy calibrations based on the high energy αs will be presented.

Chapter 4

Relative energy corrections for the DEAP-1 detector

The energy calibration in DEAP-1 drifts over time by a very small, but noticeable amount. Variations in the ^{22}Na peak position are observed in calibration runs, which are taken with significant amount of time between them. ^{40}K and ^{208}Tl are detector backgrounds with Compton edges that are visible in background runs independent of the voltage supplied to the PMTs. We present a novel function for fitting these Compton edges and results from its application. An example of the fitter results is shown in Figure 4.1 which shows the two Compton edges. The function does not use the TMinuit class since the χ^2 distribution has many local minima that stop iterations prematurely. Instead, we search through the χ^2 distribution curve manually to determine the most accurate value that will align the Compton edges from different runs. A run with a known energy scale can now be used to determine an accurate keV$_r$/pe calibration constant for several runs. Using these calibration constants the energy resolution is improved by between 1$\sim$3%. The function can also reveal information about the nature of the calibration drift and allow us to predict and minimise it in the future and for the DEAP-3600 detector.

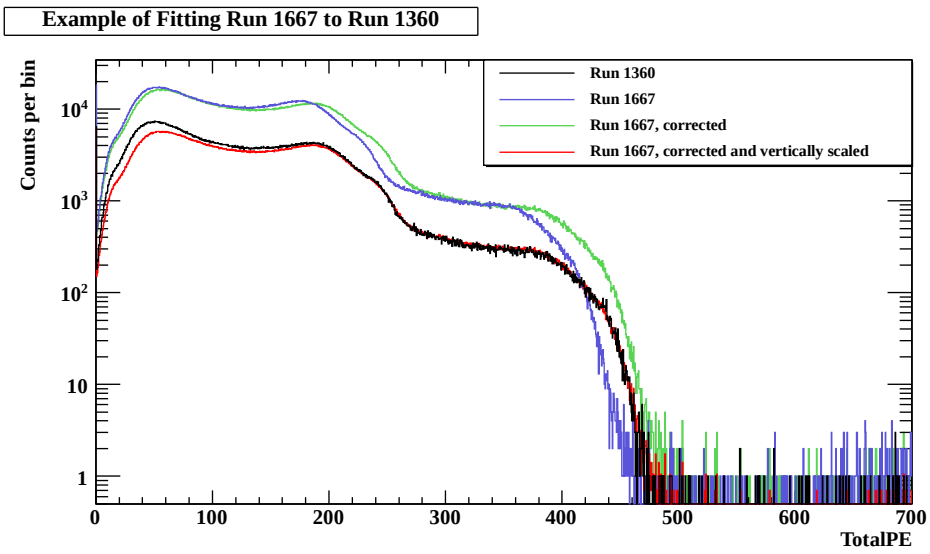

Figure 4.1: An example of the results of the fitter function. Run 1667 is fit to run 1360, a correction factor of 1.061 is returned. The spectrum is also vertically scaled for illustrative purposes.

4.1 Fitting Mechanism

The code was developed primarily by Minchang Zhang, a summer student from 2009, while the work presented herein uses the tool for analysis and background studies. The fitting function calculates a spectrum $F(E;\xi)$ of the number of detected photons (TotalPE) from a reference spectrum $F_{ref}(E)$ and a scaling factor ξ

$$F(E;\xi) = n\, F_{ref}\left(\frac{E}{\xi}\right) \tag{4.1}$$

where n is an arbitrary scaling factor. The calculated histogram $F(E;\xi)$ will have features that match an energy spectrum that we are fitting the reference spectrum to. The code was created for use with the ROOT data analysis framework [137], which provides a multitude of useful classes for building data structures and performing analysis tasks. The function is user defined and accessed through the TFitter class by creating a TF1 object. A call to the TH1::Fit function is never explicitly made since the TFitter and TMinuit ap-

proach return results dependent on the TF1 object's initial parameters. This is because the distribution of χ^2 values for varying parameters is not smooth and contains many local minima which TFitter finds and returns (Figure 4.2). Since the initial parameters define where in the distribution TFitter begins to look for the lowest χ^2 value we can get inconsistent results. Many attempts were made to overcome this, such as smoothing the 1D TotalPE histograms that define the TF1 object, convoluting it with a Gaussian function, and modifying TFitter's behaviour, but it was decided to bypass TFitter and perform the χ^2 search manually based on a known range that depends on the nature of the DEAP-1 detector results. We evaluate χ^2 as:

$$\chi^2 = \sum_{x=0}^{n} \frac{\big(S_k(E) \; - \; F_k(E;\xi)\big)^2}{S_k(E) \; + \; F_k(E;\xi)} \tag{4.2}$$

where $S_k(E)$ is a static spectrum that F_{ref} is being fit to. In this calculation $S_k(E)$ and $F_k(E)$ both represent histograms corresponding to a the number of counts at a given energy, so the dependence of the χ^2 calculation on a standard deviation of the operation is of order $\sqrt{S_k(E) \; + \; F_k(E)}$. The fitting function returns ξ, the linear modification to TotalPE required to align the Compton edges of the runs and uses an arbitrary vertical scaling factor n. It is easily modified to also incorporate a horizontal translation. The vertical scaling factor is defined by the integral of the histograms within the range of the TF1 object.

The code is composed of four parts: the fitting function, a sorting function, a function that calculates the χ^2 result, and a main function. The sorting function determines the lowest χ^2 value calculated and the fitting function defines the TF1 object created in the main function. The main function uses user defined arguments to get the runs being analysed, determine whether they were high-voltage (HV) or low-voltage (LV) background runs, and create TChain objects used to create the 1D TotalPE histograms that are fit to each other.

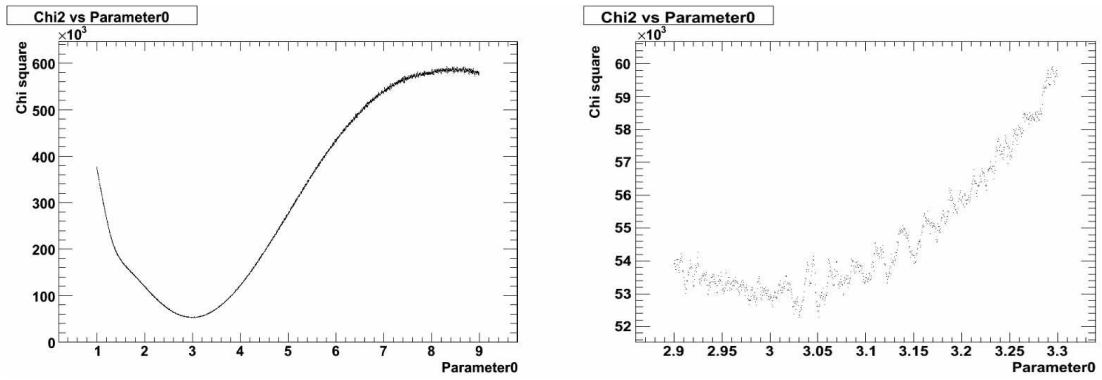

Figure 4.2: χ^2 distribution showing large number of local minima which prematurely stop the TFitter iterations when fitting with TMinuit in ROOT. The two panels are the same distribution with changes to the range of Parameter0 = ξ to show detail about the minimum.

The range of fitting depends on the voltage supplied to the PMTs and can be changed if the function fails to fit given runs. The range of the horizontal correction result that we are searching for is also determined manually for the TF1 object. The initial width of this range also depends on PMT voltage and can be adjusted if a fit fails. For example, when fitting runs of the same type from the same operational period (2008 or 2009) we expect the Compton edges, and the $\mathrm{keV_r}$/pe value, to be very close. Therefore we use a range of 0.95 to 1.05 with a 0.001 step size. When comparing runs from different operation periods this range is increased to between 0.8 and 1.2 which increases the number of steps needed for the calculations. For each step of this range the χ^2 value is calculated and stored in an array. The code may be modified to use a smaller step size and more iterations to improve accuracy, but it was determined that such resolution would be beyond our level of uncertainty. The sorting function searches the χ^2 distribution curve to find the lowest values. A grid search is used with coarse intervals used first to reduce the range and then a finer search returns the correction factor. For fitting LV to other LV runs, the fitting interval is [200 pe, 400 pe] and the integral is taken over [220 pe,

480 pe]. For fitting LV runs to HV runs or fitting HV runs to other HV runs the fitting interval is [1100 pe, 2500 pe] and the integral is taken over the same range. We give both LV and HV histograms the same bin size and define the range of the histograms to be from 0 pe to 700 pe (LV) or 7500 pe (HV). If we are fitting LV runs to HV runs the LV histogram is given the same range as the HV run.

The code is capable of fitting sets of DEAP-1 runs chained together. However, taking into account the relative corrections between the runs in a chain has not been included. This is because recalculating the correction factors is inefficient and a method of storing those results has not yet been decided. We identify and use runs in sets, determined by when the data was collected. For example, run set 2197 is a LV background run taken from April 24-27, 2009, and consists of runs 2197 to 2202. For this set we would take each run and fit them to 2197 (or 2198 if the first run in a set is very short). The most efficient way to incorporate these correction factors (without modifying the code) is to generate a set of corrected ntuple files, which store each event's calculated variables from the waveforms, and then analysing the larger run sets.

4.2 Limitations

When the code is implemented, the fit is not always reliable and there are limitations on what data can be analysed. The code creates an image containing the two original histograms, and the corrected histogram in order to diagnose the goodness of fit. Often the issue is that the Compton edges have different shapes. This can be overcome by adjusting the fitting interval manually. There are several reasons why the shapes of the TotalPE spectra would differ: if a run is very short and has low statistics, or whether there was a problem setting up the data collection (while commissioning the VME crate, for example). Difficulties can also show up when fitting certain LV runs to HV

runs or mixing the 2008 and 2009 data runs. ^{22}Na PSD runs cannot be fit at all using this method due to the implementation of SCA cuts which effectively veto the high energy events in the region of the Compton edges. The ^{22}Na calibration runs taken to analyse PSD do not have these Compton edges in their TotalPE spectra. This is the strongest limitation, since these runs make up the scientific regime of DEAP-1 operations. The tool will become very useful for DEAP-3600 when the background runs are used to achieve the primary scientific goals. Quality assurance checks should be carried out before results of the fitting function are used in analysis.

The code has not been adapted to work with new Midas data, which requires determining new ranges of integration. The next adaptation of the code will likely be for use with the 20 inch test vessel mentioned in Section 2.5, or with DEAP-3600.

4.3 Applications and Results

The fitting function has been primarily used in three fashions: fitting all runs to a single run, fitting all runs to a run in their respective run sets, and fitting the run sets to each other. Fitting the runs to a single run allows us to investigate the way in which correction factors change over time. This can reveal variations in detector performance and degradation of the light yield of the liquid argon. Fitting the runs in a run set to each other and fitting between the run sets improves the energy resolution of the detector and is useful for background studies. Current use has been limited to low-voltage runs and non-Midas data acquisition.

4.3.1 Correction Factors

All the low voltage background runs from 2008 and 2009 (pre-MIDAS) where fit to run 1360. Run 1360 was taken on July 31, 2008, and has a livetime of

16.19 hours. It is among the earliest runs analysed. It was chosen so that we may investigate the way the correction factors change from the start of data taking. The variation among correction factors may be seen in Figure 4.3 with notable events labelled.

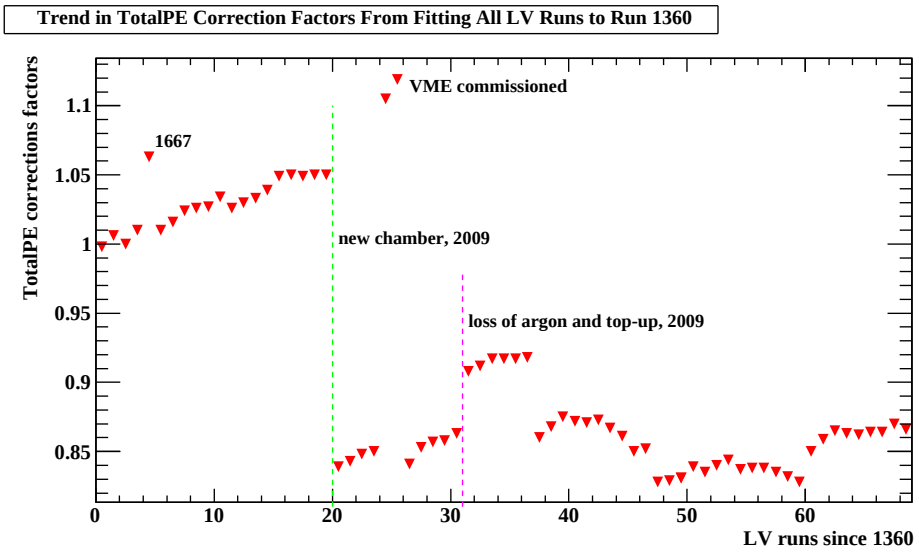

Figure 4.3: TotalPE correction factors from fitting every run analysed to run 1360. Steady degradation of argon light yield is seen in the 2008 run. Note that the argon loss event labelled is separate from that discussed in Chapter 3. This event was in 2009, no argon spike was seen.

Figure 4.3 shows the effects that changing detector parameters have on the TotalPE. The effects of altering the detector, such as installing the new chamber, changing DAQ hardware, and altering the liquid level of the argon, are quite substantial. In the 2008 data there is a steady trend of increasing correction factors which signifies a change in the light yield from liquid argon. Evidence of this trend has also been seen in standard detector operation and analysis, which was a contributing factor to the decision to replace the argon chamber and target volume. In the 2009 data we see rises and falls, which are also seen when fitting runs in a run set to a specific run. The loss of argon shown in graph is during 2009 and is a distinct event from that discussed in

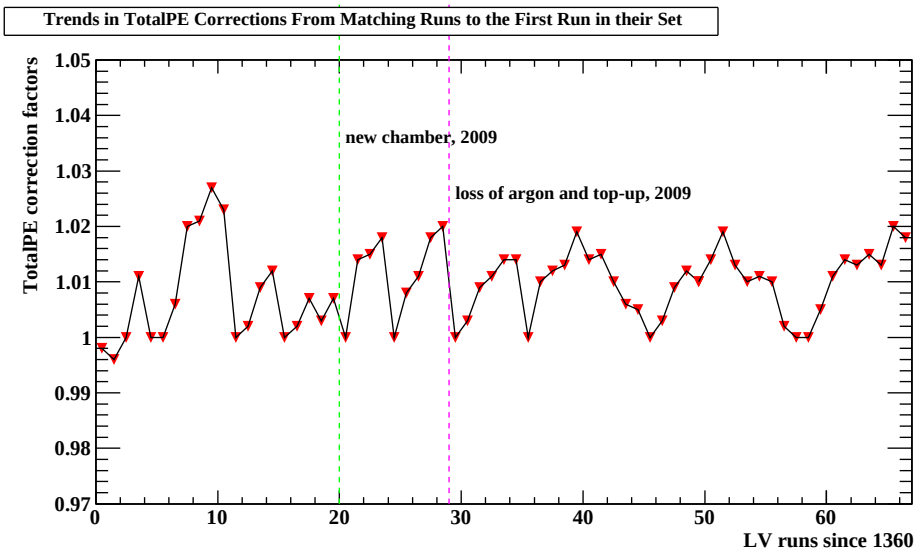

Figure 4.4: TotalPE correction factors from fitting each run in a run set to the first run in their respective sets. These factors will be useful combining the runs together.

Chapter 3. A combination of Easter holidays and a mine-wide fire alarm kept operators out of the lab for several days, during which a vent valve began to malfunction, not closing properly after restoring nitrogen coolant levels, resulting in a small loss of argon. When the argon mass was restored the rate of α events from radon was not significant.

Figure 4.4 shows the result of comparing each run in a set to the first run in that set, a list of these results is given in Appendix C. The breaks in the trend signify a change between run sets (correction factors return to 1). The trends visible in the correction factors differ between the 2008 and 2009 runs in that they steadily increase for run sets taken in 2008 but exhibit a rise and fall pattern in the data taken with the new chamber in 2009. This is only observed in two sets of runs, which are distinct in their length, and the variations may oscillate. The cause of the distinction between the two underground periods is most likely due to changes made to the electronics, process systems and chamber.

4.3.2 Calibration of 2008 Data

Applying the correction factors plotted in Figure 4.4 to the data and then combining runs together can improve the energy resolution of the detector by up to 4%. We can use the radon spike discussed in Chapter 3, which is run set 1950, to provide an accurate calibration factor for the 2008 data. Fitting Gaussian curves to the peaks of known radionuclides, Figure 4.5, a calibration factor for the number of photoelectrons (TotalPE) per keV_r can be calculated. The calibration factor is only valid for this run set, or runs corrected to fit it. Run set 1950 was, therefore, additionally corrected to fit run 1360, as are other runs, for the purpose of redoing the analysis presented in Chapter 3. These correction factors are given in Appendix B. The radon spike data has three distinct peaks from ^{222}Rn, ^{218}Po, and ^{214}Po. The results are plotted in Figure 4.6 and a linear fit was performed to determine the calibration factor. The y-intercept of the fit is consistent with zero (18 ± 127 pe) so the intercept parameter was fixed at zero and the fit was repeated. This resulted in a calibration factor with lower uncertainty that preserves the position equivalence of the known α energies and the visible peaks in the run set's calibrated energy spectrum. The peak energies and keV_r/pe results are summarised in Table 4.3.2. For run sets corrected to run 1360 a keV_r/pe calibration factor of 7.20 ± 0.13 keV_r/pe was found.

Radionuclide	α energy (MeV_r)	TotalPE (pe)	Width	keV_r/pe
^{222}Rn	5.489	760 ± 3	33 ± 3	7.22 ± 0.31
^{218}Po	6.002	837 ± 3	21 ± 2	7.17 ± 0.18
^{214}Po	7.687	1062 ± 3	34 ± 3	7.23 ± 0.23

Table 4.1: Summary of results from fitting Gaussian functions to peaks from known radionuclides in the TotalPE spectrum of run set 1950, after correcting each run in the set to fit run 1950 and correcting the entire run set to fit run 1360.

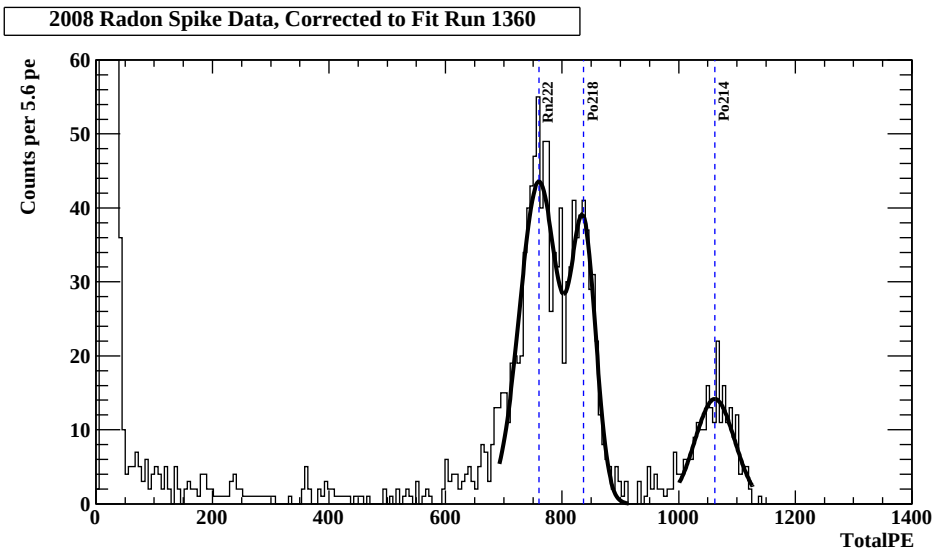

Figure 4.5: Corrected run set 1950, taken shortly after the 2008 argon top up. The peaks are fit with Gaussian functions. The effect of the corrections can be seen by comparing with Figure 3.4.

4.3.3 Analysis of α Backgrounds After Corrections

Using these correction factors the analysis presented in Chapter 3 can be redone to see whether small changes in energy calibration account for the over-subtraction seen before (Figure 3.7). Each run had its TotalPE corrected and was then added to a composite spectrum for its run set. These composite spectra were fit to run 1360 and combined to form a background spectrum for the 2008 data. Cuts were applied to F_{prompt} and other data cleaning characteristics (see Appendix A) and they were normalised by livetime. The background spectrum was subtracted from run set 1950 to remove backgrounds common to all 2008 detector runs and leave backgrounds introduced during the argon top-up, resulting, once again, in a spectrum consisting of only the fast-lived daughters of ^{222}Rn. This pure radon spectrum was then normalised so that its ^{214}Po peak contained the same number of events as the same peak in the background spectrum. Subtracting the pure radon spectrum from the background spectrum results in the spectrum of backgrounds that are not

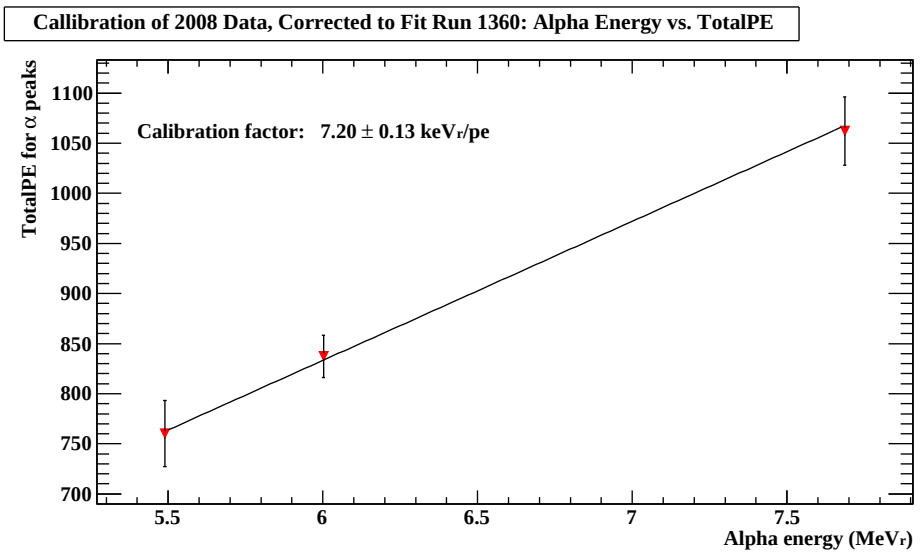

Figure 4.6: Energy calibration of corrected 2008 TotalPE spectrum using α energies. The error bars represent the widths of the Gaussian distribution fit to the peaks.

associated with ^{222}Rn in the argon, it is dominated by long lived ^{210}Po on the detector walls.

As seen in Figure 4.7, redoing the analysis after making corrections to TotalPE does remove the over-subtraction seen in Figure 3.7. This is a significant example of the usefulness of the fitting function results and demonstrates that corrections to the energy resolution are needed to perform detailed analysis of the energy spectra obtained by the detector. The remaining ^{210}Po peak in Figure 4.7 exhibits an asymmetry in its appearance, with more events on the left and sharper fall on the right. This may be due to some remaining over-subtraction from the analysis, or detector backgrounds unrelated to radon contamination from the top up. However, detailed studies of the TPB have been carried out within the collaboration in which the effects of α radiation emitted from below the surface of the TPB is investigated [138, 139].

Firstly, the peak is now centred at 5.097 ± 0.021 keV$_r$ which is a 3.9% loss of energy. Calculations performed with the SRIM computer program [140]

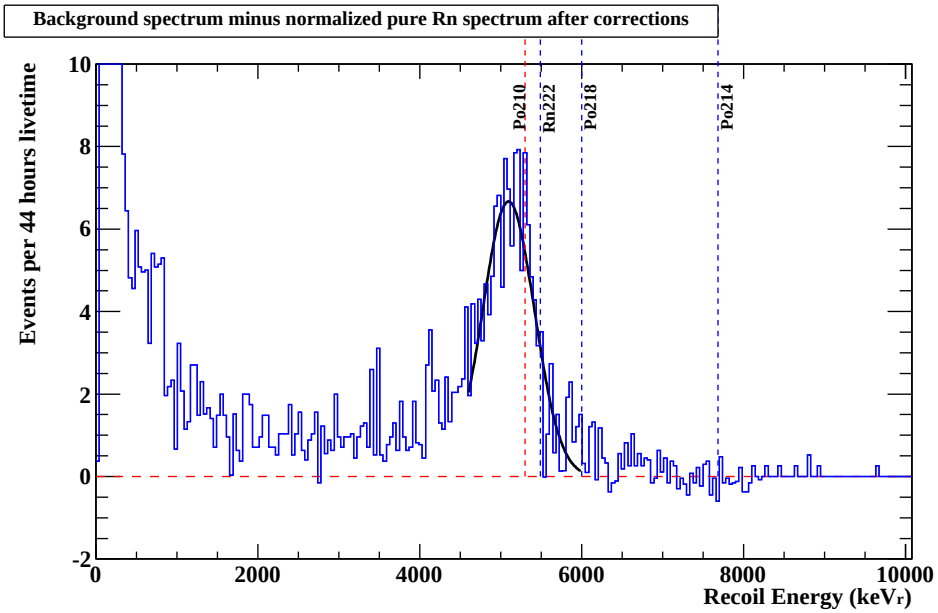

Figure 4.7: Corrected energy spectrum after subtracting the pure radon spectrum. Large over-subtractions are seen in Figure 3.4 are no longer visible.

where done to determine the energy loss of a 5.3 MeV alpha as a function of TPB depth and found that a loss of 207 keV corresponds to a depth of about 2 μm, which implies that the ^{210}Po may be on, or very near, the surface of the acrylic sleeve, and that αs pass through the entire layer of TPB. Secondly, the α leakage into the WIMP region of interest from several radionuclide-surface geometries was investigated. Calculations of ^{210}Po on the acrylic sleeve ejecting αs at varying angles through the TPB show a non-Gaussian drop in α energy below the maximum energy of the peak, consistent with the non-linearity exhibited in all the plots presented here. Thus the asymmetry is most likely a real effect, due to radionuclides buried beneath the TPB, and causes α peaks to be more washed out below the peak energy due to αs taking longer paths through the TPB. It must be emphasised that the result of this analysis is only those ^{210}Po events that are long-lived detector backgrounds, activity in the LAr introduced in the spike is removed, so ^{210}Po decays with a full α energy are minimised. This result is also seen in the more recent detector

runs, although with significantly reduced α rates since new detector chamber were constructed with the goal of reducing the amount of ^{210}Po on the walls.

4.3.4 Calibration of 2009 Data

Calibrating the 2009 data is much more difficult because there is no event in which a known α source was introduced during the background runs. Furthermore, we cannot rely on the 2008 calibrations since the construction process of the new chamber has changed and the background sources are different. We also cannot use the argon spike data since, in general, the light yield is different and variations in the shape of the Compton edges appear between operational periods. Methods of introducing radon to DEAP-1 towards the end of the current underground run have been discussed, as it has proven to be a valuable analysis tool and the long lasting effects of ^{210}Po do not matter since DEAP-1 will be dismantled and rebuilt with a new chamber.

Much work has been done to determine the sources of background radiation in the new chamber and this calibration attempt builds off of that work. Current models described in [141] show that the spectrum of high energy and high F_{prompt} background events may be attributed to a combination of daughters of ^{224}Ra from the decay chain of ^{232}Th, as well as those from ^{222}Rn seen before. Figure 4.9 shows the results of such a model as derived from the 2009 background data, and Figure 3.1 shows the decay chain of ^{232}Th, with energies and half-lives. These background sources are believed to exist in the detector materials before the chamber is constructed and deployed underground, rather than be linked to the argon. Studies of the low-F_{prompt}, α-like events in the previous run showed that there are two related sources of high energy α particles: the detector walls and the bulk argon, while utmost care was taken to reduce the amount of contamination for the 2009 underground run.

As in section 4.3.2, each run in a set was fit to the first run in the set, and

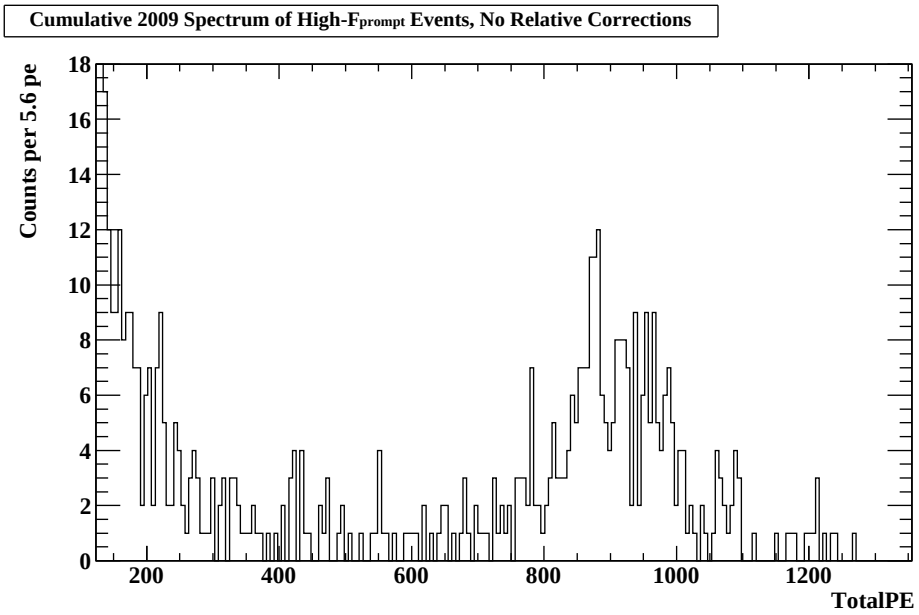

Figure 4.8: The cumulative spectrum of high-F_{prompt} events from the 2009 underground run, before corrections from the fitter function are applied. Peaks from αs are not well resolved.

the runs were combined into a single TotalPE spectrum. Each of these spectra were then fit to a common run and a cumulative background spectrum was built. The initial effect of the energy corrections is seen in Figure 4.10. Peak positions and widths are better resolved after applying corrections and show a well defined peak at ≈ 860 pe. The uncorrected spectrum is shown in Figure 4.8. A set of Gaussian functions was fit to the spectrum and calibration factors were extracted as before. These results are presented in Table 4.2. Since the peaks may represent multiple radionuclides, weighted averages were calculated based of the predicted number of decays from each source in [141]. The peak positions were plotted against the suspected α energies and a linear fit was performed. The y-intercept was consistent with zero again (-18 ± 197) so this parameter was again fixed at zero to prevent the results from being offset.

The ^{210}Po peak is not well resolved in this spectrum and a Gaussian was not well fit to it. This results in an artificially low width with a large uncertainty.

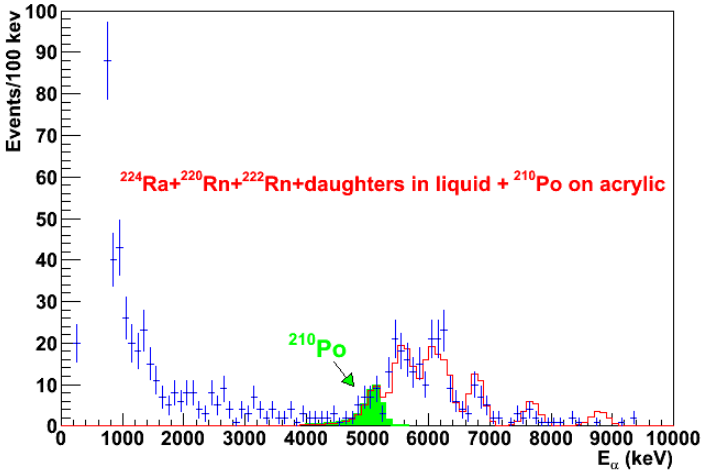

Figure 4.9: Model of potential background sources seen in the 2009 detector run showing the effect of including daughters of ^{224}Ra. From [141].

Radionuclide	α energy (MeV$_r$)	TotalPE (pe)	Width	keV$_r$/pe
^{210}Po	5.304	823 ± 14	13 ± 11	6.45 ± 0.11
^{222}Rn & ^{224}Ra	5.620	888 ± 7	45 ± 8	6.33 ± 0.05
^{218}Po & ^{220}Rn & ^{212}Bi	6.206	989 ± 6	23 ± 5	6.28 ± 0.04
^{216}Po	6.778	1082 ± 9	26 ± 14	6.26 ± 0.05
^{214}Po	7.687	1217 ± 33	60 ± 72	6.31 ± 0.17

Table 4.2: Summary of results from fitting Gaussian functions to peaks from proposed radionuclides in the cumulative TotalPE spectrum from background runs taken in 2009, after applying corrections to each run.

That the ^{210}Po peak is overlapping the ^{222}Rn & ^{224}Ra peak is consistent with the results from 2008. With this point omitted, the fit returns a calibration factor of 6.36 ± 0.07 keV$_r$/pe for corrected data.

There may be another peak observed below 800 pe in Figure 4.10 with a lower energy than a ^{210}Po α decay that is not predicted in our models. A Gaussian was fit to this peak after calibrating the spectrum, the peak has a mean energy of 4.92 ± 0.18 MeV$_r$. While there are some radionuclides that produce α radiation within 2σ of the observed peak, its integrated area is not statistically significant compared to the background spectrum at lower

energies. In the decay chain of ^{238}U, the top two parent nuclei of ^{222}Rn both produce radiation in this energy region. However, the half-lives of these decays are far too long to produce significant peaks within the time scale of the spectrum in Figure 4.10. ^{230}Th has a half-life of 7.5×10^4 y and produces a 4.687 MeV α. Its daughter is ^{226}Ra which has a half-life of 1600 y and produces a 4.871 MeV α when decaying into ^{222}Rn. Another candidate is ^{210}Bi, which can α-decay from an excited state, but, this state is very rare and has a half-life of 3.04×10^6 y and produces a 4.946 MeV α. Its ground state, which has a half-life of only 5.01 d, may also α-decay, but is only observed to do so on the order of 10^{-4}% of the time. The ejected α will have an energy of either 4.656 MeV (60%) or 4.694 MeV (40%). Other candidates are also either too rare in nature or have too small of a chance of occurring. While the peak may contain a couple of α events from radionuclide known to exist in the LAr, it is more likely due to noise or is an artifact of the analysis.

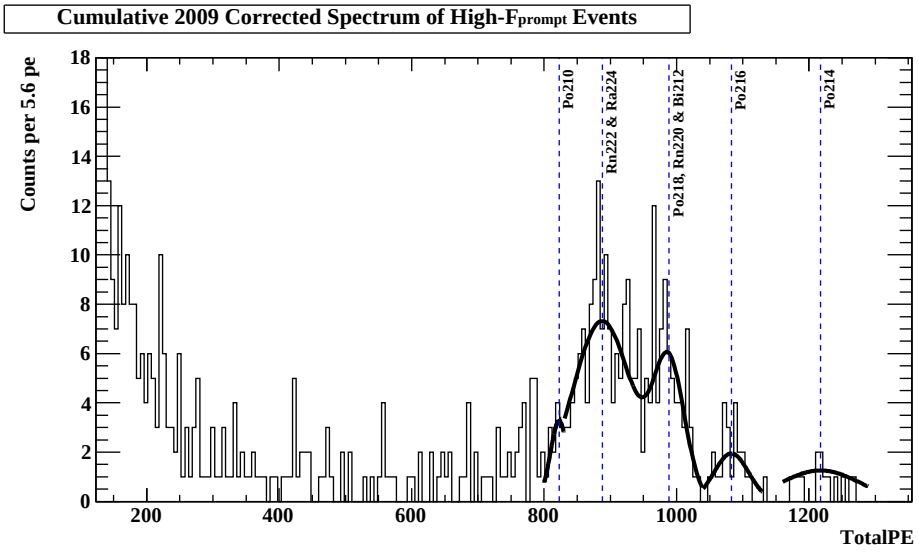

Figure 4.10: Background spectrum from 2009 after corrections, Gaussian functions fit to notable peaks. The effect of the corrections can be seen by comparing with Figure 4.8.

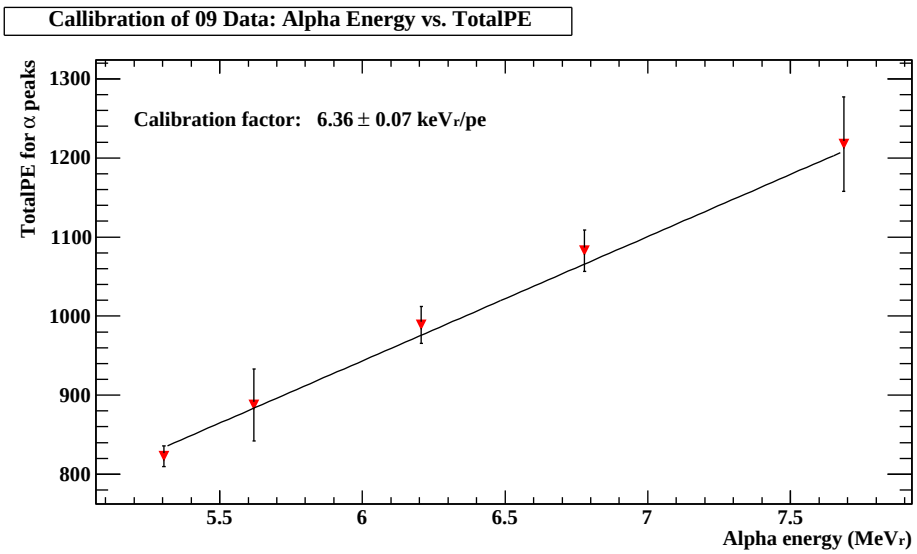

Figure 4.11: Energy calibration of corrected 2009 TotalPE spectrum using α energies. The error bars represent the widths of the Gaussian distribution fit to the peaks.

4.4 Closing Remarks

In this chapter, a novel tool for making small run-by-run corrections to the TotalPE spectrum was presented. This tool was shown to have unexpected, yet useful, applications; notably, its results can stand alone to qualitatively monitor DEAP-1. The tool leads to improvements to the the energy resolution, improving analyses based on the TotalPE variable.

We returned to the analysis presented in Chapter 3 under the prediction that corrections to TotalPE would reduce the oversubtraction seen. It was hoped that this effect was not due to actual events in the energy spectrum, but an artifact left by the analysis, which was demonstrated by repeating the analysis using the corrections. I went further and measured the peak positions of the known α energies and determined energy calibration factors for these data sets. These results can be combined with the results from the fitter function and the $\mathcal{L}_{\text{eff}}$ to determine accurate energy calibration factors for individual runs in future analyses.

Chapter 5

Measurement of High Efficiency Hamamatsu R877-100 PMT

A high-efficiency Hamamatsu R877-100 PMT has been delivered to the University of Alberta for evaluation by the DEAP collaboration. The increase in efficiency could lead to a much greater light yield, but other experiments have reported a slower rise time [142],[143]. We have placed the PMT in a small dark box and had a base and preamplifier built by the Department of Physics' Electronic Shop which will be run into either an oscilloscope or a multi-channel analyser. With this setup we have demonstrated the PMT's ability to distinguish single photoelectrons (SPE) and characterised the PMT by measuring the SPE pulse height spectrum, the peak-to-valley ratio, the dark pulse rate, the baseline, time resolution and SPE efficiency for varying the high voltage supplied to the PMT.

A high efficiency PMT is desired for DEAP-3600 where light yield has a strong effect on PSD. How well we can characterise an event depends on the amount of light collected which makes up the pulse-shape. Many of the design choices of DEAP-3600 have been based on how they affect light yield. It is important to understand how these new PMTs respond to SPE, which make up the late section of the waveforms. Understanding and correcting for the portions of a signal due to the PMTs is crucial to PSD. Besides knowing

the behaviour of each PMT, detailed studies of the baselines of the DEAP-3600 PMTs will be carried out and incorporated into the waveform analysis, which was previously done in DEAP-1 with the Electron Tubes PMTs, and is currently undergoing with the 8" DEAP-3600 PMTs now installed on DEAP-1.

5.1 Experimental Setup and Procedure

A single event in the DEAP-3600 detector will produce the same number of photons as the same event in the DEAP-1 detector. In DEAP-1 these photons are incident on only two PMTs whereas in DEAP-3600 the light will be divided among the entire array of 266 PMTs that surround the 3600 kg target mass of liquid argon. In order to get the most accurate results we wish to collect as many photons as possible; how well we can characterise an event depends on the amount of light collected which makes up the pulse-shape. DEAP-3600 will use PMTs with higher quantum efficiency than those currently used on DEAP-1. We wish to understand the effects of a higher quantum efficiency on the light yield of the detector and the effects that a higher light yield will have on our ability to understand and reject background signals. A PMT with a specifications desirable for DEAP-3600 that will fit on the smaller 5" light guides of DEAP-1 was selected for evaluation. The increased efficiency would lead to increased noise and the PMTs need to be understood before deployment. This work presents a series measurements performed on the selected Hamamatsu R877-100 5" flat-faced PMT. PMTs selected for the DEAP-3600 detector will have a spherical face and large, 8" diameter. The R877-100 PMT is similar in construction and geometry to the Electron Tubes 9390B PMTs currently deployed on DEAP-1, using borosilicate glass and a bialkali photocathode. The Hamamatsu PMT uses an advanced photocathode construction that is calls super-bialkali (SBA) that allows the R877-100 to achieve much higher quantum efficiency than PMTs using standard bialkali photocathodes.

At normal operating voltages and with ideal light sources, the Hamamatsu R877-100 is expected to have a higher quantum efficiency of 34% compared to 28% for the ET PMT. The Hamamatsu PMT also has a much lower gain. The PMTs are compared at their nominal voltages, which they would operated near on DEAP-1 and are 1250 V and 1500 V for the Hamamatsu and ET PMTs respectively.

The PMTs are powered by a variable power supply housed in a NIM crate and we have tested the full voltage range that is specified for the PMTs. The output of the PMT will first run through a custom built base consisting mostly of voltage splitters for the dynodes and fewer high-voltage filters, then the signal passes through a custom built preamplifier. The preamplifier and base were designed at the University of Alberta. Circuit diagrams for these components are shown in Appendix E. Several spare boards (Figures. 5.1, 5.2) were obtained for both so we remain flexible to alter the design and specifications of either. The preamplifier is designed to produce signals desirable for DEAP-3600; the output consists of fast pulses ($\approx$ 100 ns) with small amplitudes for SPE. The output of the Hamamatsu PMT is much smaller than that of the Electron Tubes PMT, since it has a much lower gain, so a linear amplifier is also employed when using the Hamamatsu PMT. This allows very small pulses due to SPE (≈ -10 mV) to be recognised by the discriminators which often have thresholds of -30 mV. The preamplifier is incorporated into the circuit shown in Figure 5.3, which allows us to measure the response of the PMT in several ways. From the preamplifier the signal is passed to a fan-in/fan-out module and then either to an oscilloscope, directly to a multi-channel analyser, or through a series of NIM logic units to count pulses or logically determine whether the signal and was in coincidence with a light source. The MCA and DAQ software were both developed at the University of Alberta for the radon monitoring system to be installed in the clean-room that is under construction.

Depending on what we are measuring, we incorporate a discriminator, logic units, a counter and a time to pulse height converter (TPHC). See Appendix D for component details.

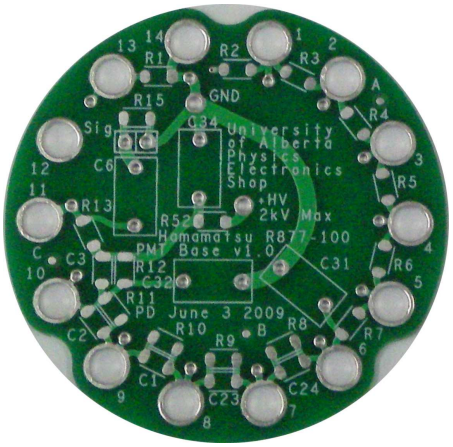

Figure 5.1: An unpopulated PMT base.

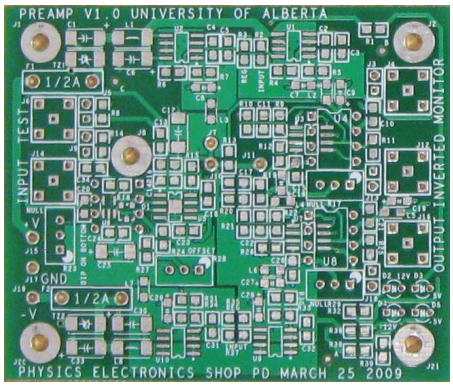

Figure 5.2: An unpopulated preamplifier board.

A single setup was used for the majority of the tests, with changes to outputs depending on the measured quantity. The fan-in/fan-out module allowed output from several stages to be viewed on the oscilloscope which allowed for easy measurements and sanity checks of the data throughout the procedure. The setup was modified when looking at time resolution to incorporate the TPHC and an additional multi-channel analyser with different shaping characteristics than our own custom designed MCA. These components were not kept online at all times since the preamplifier discriminator was needed to set up coincidence logic on the oscilloscope. When using the Hamamatsu PMT, a vital component of the setup was a second channel of the fan-in/fan-out used to control the offset of the baseline of the pulses. With careful tuning this allowed the discriminator, with a threshold of -30 mV, to recognise very small amplitude pulses (this was not necessary for the ET PMT). A comprehensive schematic of the entire setup is shown in Figure 5.3 with the TPHC included. The spectra were measured in 50 V steps, varying the voltage supplied to the

PMT from 1050 V to 1600 V for the Hamamatsu PMT and from 1300 V to 1750 V for the ET PMT. The range of HV used for the ET PMT is limited to the range of channels that the MCA can use for its very large pulses. The higher gain of the ET PMT can also produce large enough raw pulses to saturate the preamplifier which sets a limit on the range of HV at around 1800 V, still below the maximum rating. The effects of this can be seen in Section 5.2.1.

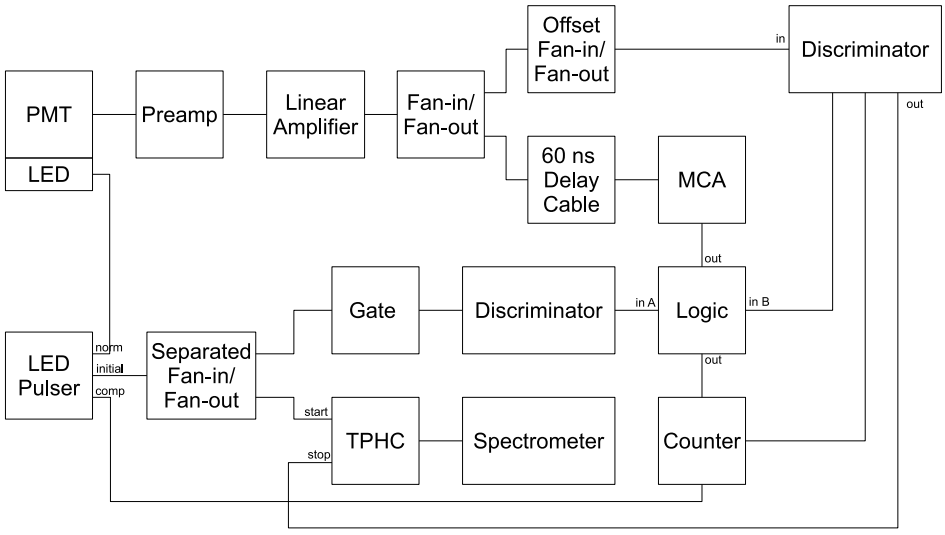

Figure 5.3: Schematic of electronics used to test the Hamamatsu and Electron Tubes PMTs. See Appendix D for details about the components used.

Testing was conducted in three stages, the first being in a completely dark state, followed by the use of an LED and then a test of the timing resolution. The first measurements were of the dark pulse rate and the spectrum of dark pulse amplitudes. The PMT signal was passed through the preamplifier (and linear amp for the Hamamatsu tube) and then through the fan-in/fan-out and into the discriminator and MCA. The discriminator output pulses were counted with the counter for each supplied high-voltage (HV) increment and a spectrum of dark pulses was generated by the MCA and recorded on a

computer.

The PMT response to single photoelectrons was measured in the second set of measurements. An LED was used to produce SPE and a precise coincidence test was set up using a logic unit. Since the time between LED flashes and PMT pulses varies with the HV supplied to the PMTs, the timing of pulses and gates had to be changed for each HV. An output of the LED's pulse generator was passed through a fan-in/fan-out module and then to a gate stretcher and discriminator. This allowed for narrow pulses corresponding to the LED flashes that occur within the time interval of the PMT response. A logic unit takes this modified LED signal and the discriminated PMT signal and is used as a trigger for the MCA. The oscilloscope also triggers on the coincidence between the modified PMT pulses and the PMT response. Pulse traces for 10,000 triggered events were averaged with an oscilloscope. The averaged traces show the PMT response to SPE. Signals due to noise and multiple photons are statistically suppressed in the average. This allows us to measure the baseline, and, by comparing the pulses from both PMTs, a qualitative assessment of the effect due to electronics (base and preamplifier) can be made. The data from both the MCA and oscilloscope will be used to determine the average pulse amplitude due to SPE. A further test of the relative efficiency was be done using the trigger. The LED amplitude was set to produce about one PMT trigger for every 50 LED flashes at nominal voltage (1250 V and 1500 V for the Hamamatsu and ET PMTs, respectively). With the LED amplitude fixed, the PMT high voltage was varied and the change in the ratio was recorded. This gave a measurement of how much the signal yield for a consistent amount of light varies with HV.

The third set of measurements investigates the relationship between varying HV and the time response of the PMTs. The LED flashes are passed to the 'start' input of the TPHC and the PMT discriminator pulses are passed to

the 'stop' input. The TPHC delivers pulses whose amplitude depends on the time difference between the 'start' and 'stop' signals to a Spectrum Techniques computer spectrometer which generates a spectrum of time differences.

5.2 Measurements and Results

5.2.1 Dark Pulse Height Spectrum

In each run pulses were collected by the MCA for four minutes at each HV. The spectra of amplitudes for each HV are shown in Figures 5.5 and 5.6 for the Hamamatsu and ET PMTs, respectively. The MCA is calibrated using pulses whose amplitudes are measured independently. A calibration factor of -0.5320 ± 0.0003 mV/channel with an offset of 103.4 ± 0.7 channels was determined. The signals from the PMT preamplifier (and linear amplifier in the case of the Hamamatsu PMT) split with a fan-in/fan-out module and passed directly into the MCA for this test. A simplified schematic of this setup can be seen in Figure 5.4.

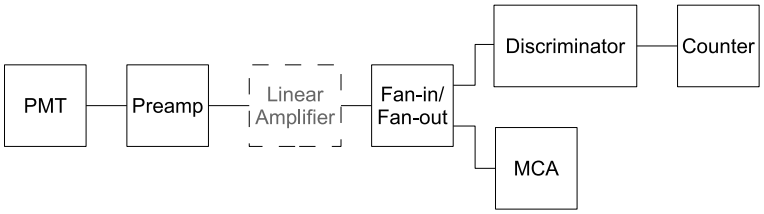

Figure 5.4: Schematic of the NIM configuration for measuring the dark pulse rate with a discriminator and counter and for collecting the dark spectra with an MCA. The linear amplifier is only used in conjunction with the Hamamatsu R877-100 PMT. See Appendix D for details about the components used.

These spectra are composed of two distinct peaks: a low voltage noise peak with a large number of events, and a higher voltage event peak, which is emphasised by the range of the plots. An ideal PMT would have all PE

signals in the event peak and no noise. As HV increases, the position of the event peak moves to a higher voltage. Using ROOT, a polynomial of degree four was fit to the local maximum and minimum at amplitudes above the noise peak, and from these the peak-to-valley ratios were determined for each voltage increment. This is a suitable fit since we are only trying to determine amplitude positions within the spectrum noise. Gaussian functions were not used because these peaks follow an unknown distribution since the events that make up the spectrum are unknown. For instance, pulses may be due to light in the dark box (from scintillation, for instance) or purely electronic in nature. The trends are plotted in Figures 5.7 and 5.8. Note the features at the highest amplitudes of the ET spectra. This effect is due to the high gain of the ET PMT and the corresponding high amplitude of the output signal. The ET signals are large enough to saturate the preamplifier, giving a maximum output. These are due primarily to high amplitude noise pulses.

The Hamamatsu PMT has a relatively steady peak-to-valley ratio until operated at 1400 V at which point the rate of change of the height of the valley decreases and the separation between noise and pulses becomes very broad. Conversely, the ET PMT exhibits a rise and fall trend, an operating voltage between 1450 V and 1650 V maximises the peak-to-valley ratio and offers the strongest ability to tell event pulses from noise pulses. While the trend in peak positions is very similar between the two PMTs, the largest difference affecting the peak-to-valley ratios is the position of the noise peak in the Hamamatsu PMT's dark pulse spectrum. As HV is increased, the position of the noise peak moves to higher voltage. Thus, the voltage position of the intersection between the noise peak and the event peak follows the position of the event peak, reducing the peak-to-valley ratio.

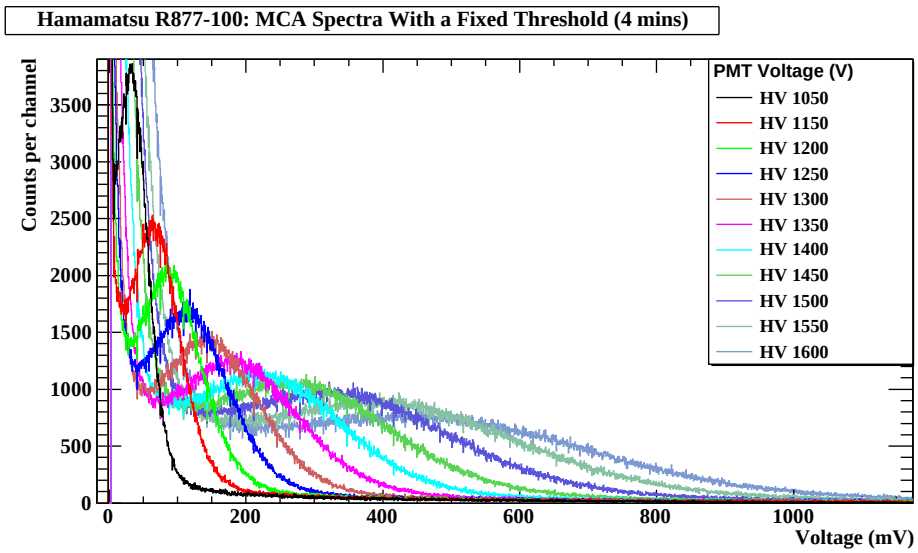

Figure 5.5: Pulse height spectra from the Hamamatsu R877-100 SBA PMT for different operating voltages. Nominal voltage is 1250 V (blue).

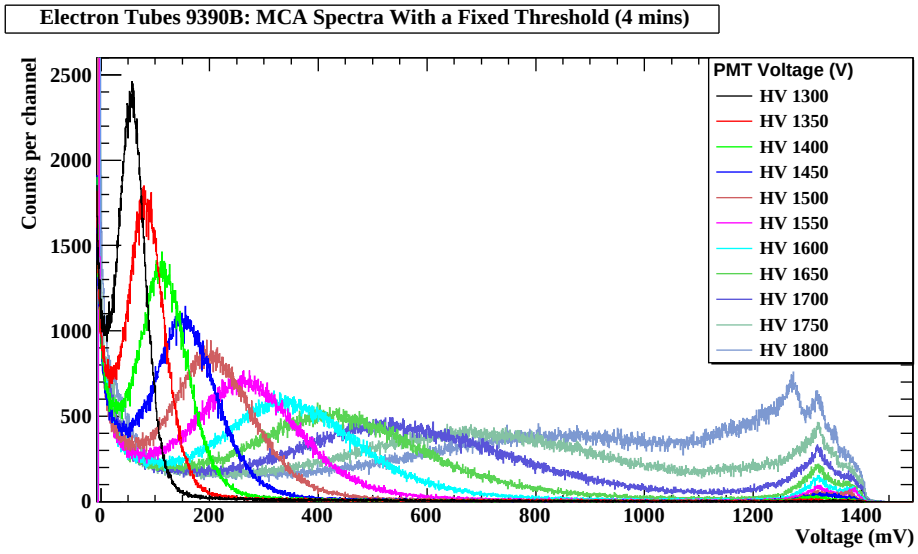

Figure 5.6: Pulse height spectra from the Electron Tubes 9390B PMT for different operating voltages. Nominal voltage is 1500 V (brown). Note the difference in the noise peak position compared to Figure 5.5.

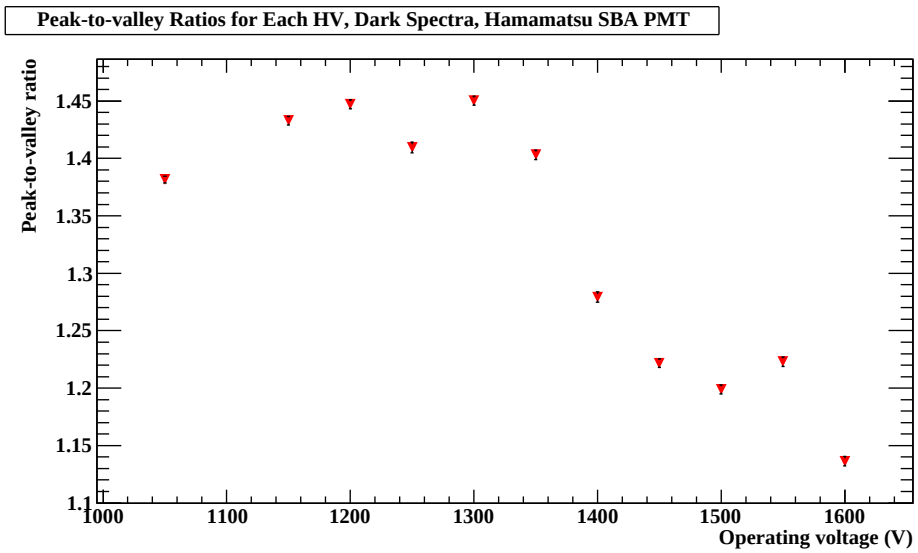

Figure 5.7: Peak-to-valley ratios for the Hamamatsu PMT. The maximum rated voltage for the Hamamatsu PMT is 1500V. The ratio drops off for higher operating voltages.

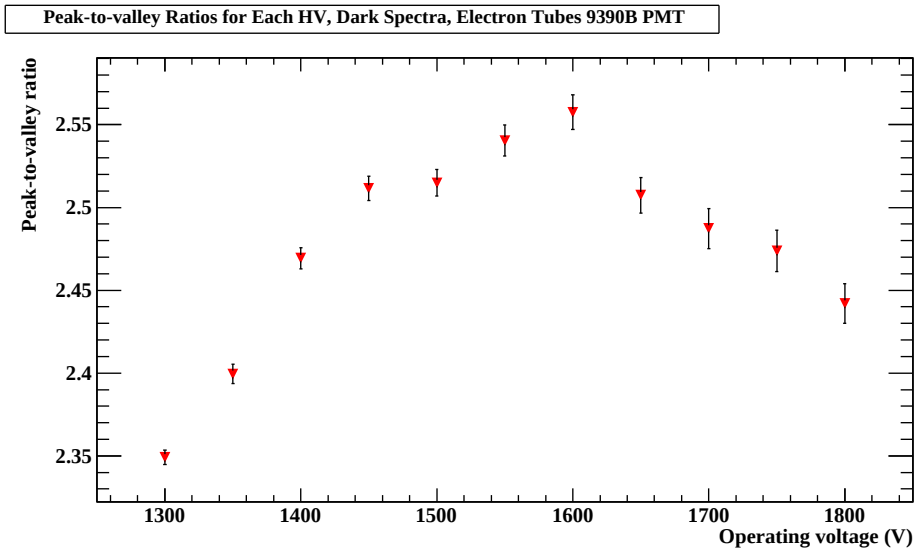

Figure 5.8: Peak-to-valley ratios for the ET PMT for different operating voltages. The maximum for the ET PMT is not reached, but a distinct peak can be discerned.

5.2.2 Dark Pulse Rate

The rate of dark pulses that the PMTs produce is a very important consideration when choosing a model, or testing those to be deployed. Random noise pulses will not trigger DEAP electronics since they are unique to individual PMTs, but will appear in the waveforms of actual events, most likely in the late portion. These pulses will directly affect F_{prompt} calculations by increasing the number of pe counted in the late light region. A dark rate of 10 kHz would be unacceptable for DEAP-3600 since for each event we may see around 25 additional SPE from noise:

$$10\,\mu s \times 10\,kHz = 0.1\,\text{noise pulses per event per PMT}$$

A rate between one and 4 kHz is acceptable, which returns between one and ten noise pulses per event. Dark noise rates are highly sensitive to operating temperature and may be reduced by cooling the PMTs and lab temperature could be monitored for the DEAP experiments. Individual PMTs will each behave slightly differently in this regard, and each of the 266 delivered for DEAP-3600 will be measured in temperature controlled environment. PMTs with undesirably high dark noise rates would need to be discarded. If the high QE PMTs cannot be demonstrated to have a low enough dark noise rate at normal operating voltages, the model will not be considered for use on DEAP experiments.

The dark pulse rate is measured by running the PMT discriminator output pulses to a counter and counting over 96 second intervals (maximum allowed). When using the Hamamatsu PMT, the PMT signal is run through a linear amplifier as well as the preamplifier. Counts were taken while the MCA was collecting the dark pulse height spectrum. The discriminator threshold is held constant at its minimum setting of -30 mV. As the HV is increased more noise pulses are allowed to cross the threshold and the dark pulse rate

increased rapidly. At nominal voltage the dark pulse rate was 2.7 kHz for the Hamamatsu PMT (1250 V) and 1.27 kHz for the ET PMT (1500 V). These rates may give rise to between three and seven noise pulses for an event in DEAP-3600.

Rates may also be calculated from the dark MCA spectra for varying thresholds. Using the determined positions of the peak and valley, rates were calculated for each HV with thresholds set at the valley, the peak and at 1/4 and 1/2 of the peak position. For the Hamamatsu PMT, the 1/2 peak position closely lines up with the valley position and rate calculated at either position appear closely related. The 1/4 peak position encroaches on the noise peak resulting in larger rates, at very low HV the rate increase dramatically to > 10 kHz.

The dark pulse rates counted with a constant voltage threshold are shown in Figures 5.9 and 5.10 and the rates calculated from the spectra are shown in Figures 5.11 and 5.12 for the Hamamatsu and ET PMTs respectively. As expected, the Hamamatsu PMT exhibits higher dark rates than the ET PMT due to its higher quantum efficiency. The rates calculated from the MCA data are much lower than those from counting the PMT discriminator pulses. This is partly due to the higher deadtime of the MCA, but also suggests that many noise pulses trigger the discriminator at low HV, which must be taken into account when setting up triggers for data taking. It is important to note that the rates determined from the counter depend on the fixed threshold of the discriminator, whereas those determined from integrating the spectra have a floating threshold. This causes the rates from the counter to increases for higher HV at much greater rate than those with the floating threshold. Generally, we find a lower dark pulse rate for the ET PMT. This was expected and the chosen Hamamatsu PMT is known to have the highest dark current among all of Hamamatsu's high quantum efficiency PMTs [144]. The ET

PMT exhibits a rise in dark pulse rate more closely following an exponential function, that rises more steeply at higher HV than the Hamamatsu PMT.

5.2.3 Triggered SPE Pulse Height Spectrum

Using the LED pulser and logic unit, a second set of spectra were taken with the MCA. These spectra are useful for calibrating DEAP electronics. Triggered, recorded events will always be due to light so the PMT response will be very similar, especially in DEAP-3600 where an event's waveforms will be produced by a small number of SPE in each PMT. The spectra collected for this measurement show how low voltage thresholds can be set to trigger on SPE, despite being in the noise region of the dark pulse spectra presented in Section 5.2.1.

The electronics between the PMT and the MCA are similar to the setup in Section 5.2.1 with two important additions, which can be seen in Figure 5.13. The first is the inclusion of a delay cable long enough to slow the PMT signals arrival at the MCA by 60 ns. For these measurements the MCA will dedicate an input to a trigger signal, from the logic unit. When this input amplitude crosses a threshold the MCA begins looking for a signal in the other inputs, the PMT signal. The trigger signal, however, comes from passing the same signal that the MCA is looking for (the PMT signal) through several NIM modules, which will take several ns. Thus the delay cable is needed, since the trigger signal would otherwise arrive at the MCA after the PMT signal. The second addition is a second fan-in/fan-out stage before the PMT signal enters the discriminator and is sent to the logic unit. We wish to be sensitive to pulses over a full range of amplitudes, but with such a setup the logic unit will only recognise pulses that cross the discriminator's -30 mV threshold, which is unacceptable when studying the Hamamatsu PMT. The fan-in/fan-out has an offset adjustment that can be adjusted such that even the smallest pulses

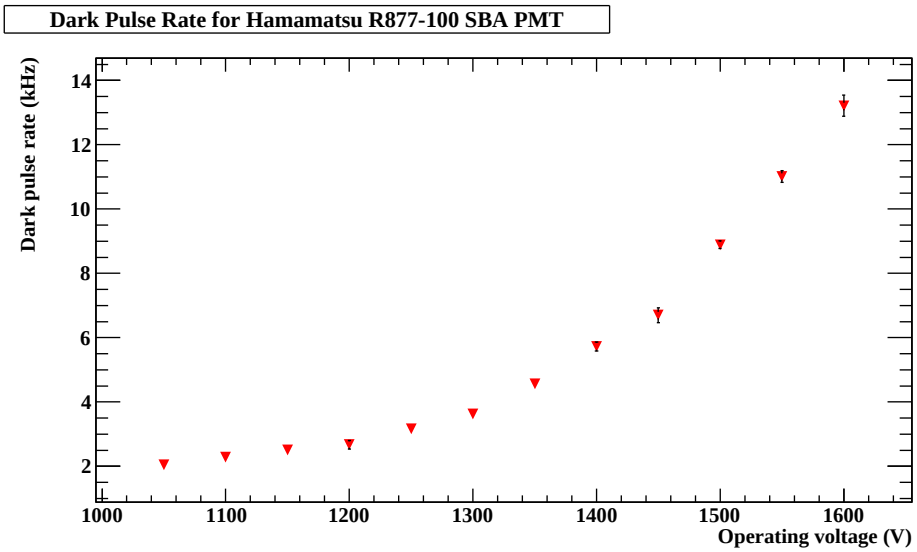

Figure 5.9: Hamamatsu PMT: dark rate for different operating voltages determined by counting PMT discriminator pulses with a minimal, constant threshold.

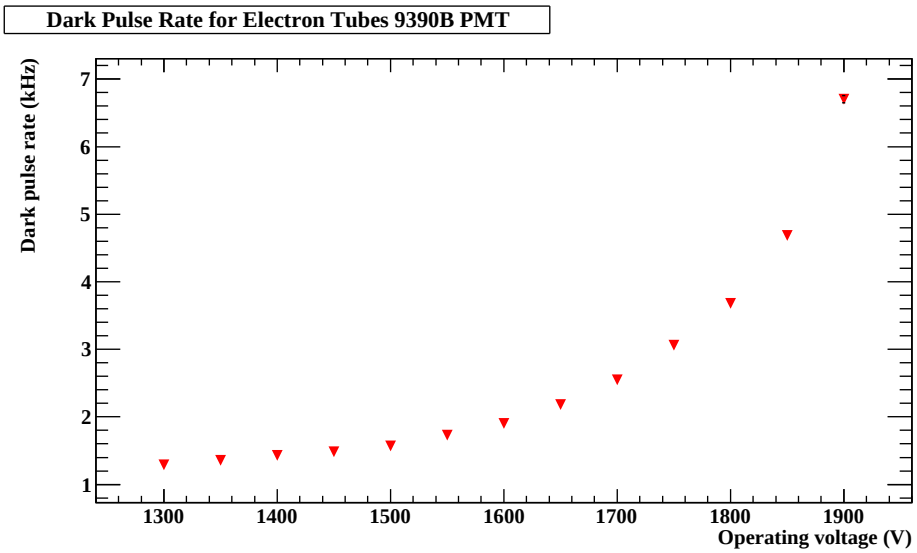

Figure 5.10: Electron Tubes PMT: dark rate for different operating voltages determined by counting PMT discriminator pulses with a minimal, constant threshold.

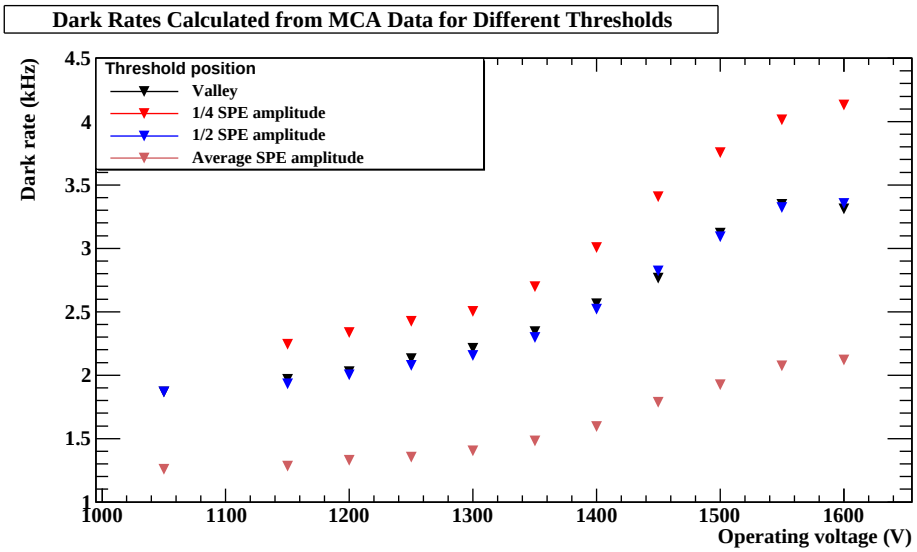

Figure 5.11: Hamamatsu PMT: rate of MCA dark spectrum events determined for varying thresholds at different operating voltages.

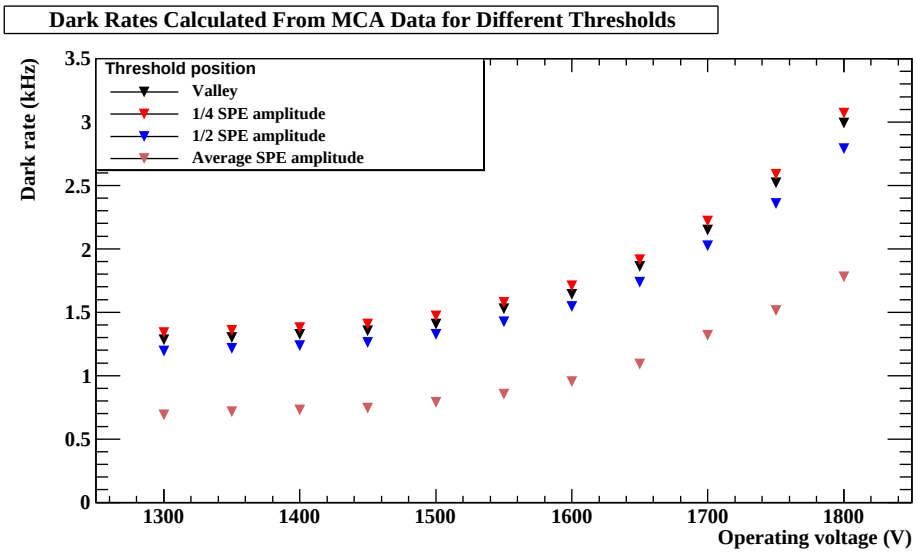

Figure 5.12: Electron Tubes PMT: rate of MCA dark spectrum events determined for varying thresholds at different operating voltages.

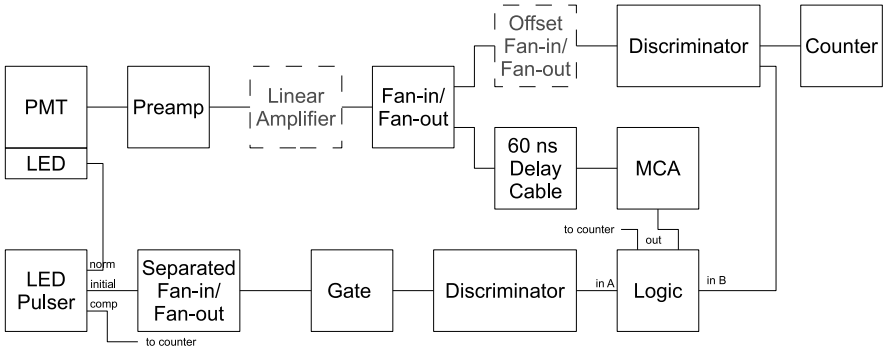

Figure 5.13: Schematic of the NIM configuration for using the LED to produce SPE and to determine when the PMT response is in coincidence with the pulser. The components in gray are only used in conjunction with the Hamamatsu R877-100 PMT. See Appendix D for details about the components used.

from the PMT can have a total amplitude greater than the threshold of the discriminator which will begin triggering on them. Moving the offset further will cause the discriminator to begin triggering on noise and miss real pulses until the rate of discriminator pulses reaches a maximum and then falls quickly to zero. A typical response plot is shown in Figure 5.14. The offset is adjusted to maximise the discriminator rate such that error due to real pulses being missed is less than 1%, carefully adjusted by observing the outputs on the oscilloscope.

A signal generator was used to supply low-amplitude, square pulses with a width of 20 ns to an LED placed inside the dark box. Due to the high current produced by the LED pulser, it was kept separate from other NIM modules in order to avoid noise being produced in other signals. This was not a perfect solution and evidence of its effect remains visible in the averaged SPE pulses taken by the oscilloscope in Section 5.2.4 (see Figure 5.23). The pulser has three output channels. The 'norm' was used to power the LED. The 'comp' output was sent to the counter to determine the rate of LED pulses. The

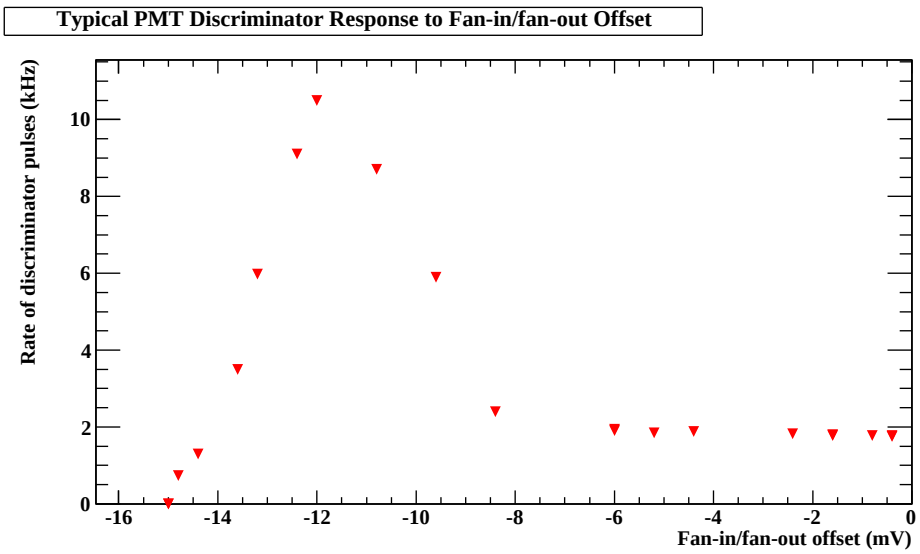

Figure 5.14: Typical response curve of the fan-in/fan-out offset on the rate of PMT discriminator pulses. The rate flattens off to the dark pulse rate corresponding to the HV supplied to the PMT when the offset amplitude decreases.

'initial' output, with a delay of 0 ns, was used by the logic unit to test when pulses generated a PMT response in coincidence.

This was done by comparing the count rate of the PMT to that of the pulser and reducing the pulse LED amplitude until we were confident that only SPE were being produced.

There is a measurable time difference between the LED flashes and the PMT response, which is investigated in Section 5.2.7. The logic unit requires both signals to overlap within a pulse width. The LED signal was delayed to achieve this. It was passed though a gate generator, which stretched the pulse, and into a discriminator channel. This had the effect of producing a narrow pulse at the same time as the PMT response. The widths of the gate and discriminators were tuned with the oscilloscope. The gate was 130 to 175 ns wide for the Hamamatsu PMT and longer for the ET PMT. The width of the LED discriminator was made wide, 54 ns, allowing the time of the PMT discriminator pulse to vary, while still being recognised as in-coincidence by

the logic unit. The LED discriminator was set narrower, 21 ns, and fell within the PMT discriminator signal. Widths were set as small as possible, such that the error in counting pulses was less that 1% as determined by viewing a large sample of random oscilloscope traces. This was done with the LED amplitude set very high, with a coincidence rate of one PMT pulse for every two LED flashes, so that the position of PMT pulses relative to LED flashes was clear. Once widths were adjusted, the offset of the second fan-in/fan-out stage that the linear amplifier runs into was adjusted when using the Hamamatsu PMT.

The counter measures the ratio between the rate of output signals from the logic unit and the rate of the LED pulser, which was ≈ 100 kHz. The rate counted for the PMT discriminator was fairly consistent for the entire HV range at about ≈ 20 kHz. This is much larger than the dark rate measured for each HV and is due to a very low discriminator threshold. The amplitude of the LED pulser is reduced until the ratio between in-coincidence PMT responses and LED flashes is $\approx 1/50$. Such a low rate of PMT responses ensures that when the LED is sent a signal it generates one or fewer photoelectrons. In general LED flashes will produce very little light. While there is no guarantee that multiple photons were not produced, the number of pulses analysed will statistically limit the analysis to SPE.

The spectra collected show the PMT response to SPE, with either very small noise peaks visible, or none at all. The noise reduction is not due to the coincidence setup, low amplitude noise pulses will still occur in coincidence with the LED at a very low rate. Since the MCA is being triggered with a coincidence between the LED pulse and the PMT response, the MCA will not collect pulses that are not large enough to trigger the discriminator used in the coincidence setup. The spectra for each PMT are shown in Figures 5.15 and 5.16. The MCA threshold was set to the minimum channel possible and the voltage at which the hardware thresholds come in can be seen in the spectra.

The threshold of the PMT hardware, though minimised, was greater than that of the MCA.

Gaussian curves were fit to the peaks, and the mean in mV was calculated. A measure of the average SPE pulse height is also obtained from the averaged waveforms captured with the oscilloscope (Section 5.2.4). Averaging the SPE pulses was done concurrently with this test, with coincidence logic being handled by the oscilloscope's internal triggers. The two measurements differ, and the cause was thoroughly investigated. A very careful calibration of the MCA was undertaken, and the oscilloscope traces were analysed in ROOT, with baseline offsets accounted for. The measurements were determined to be sound, and differences are due to hardware, likely being attributed to the way the MCA may measure maxima in signal noise, the way the averaged waveforms have noise removed, and the way that pulse triggers on the oscilloscope have a fixed position. Additionally, the mode of the MCA spectrum can be measured to compliment the mean given by the Gaussian curve.

A fourth set of measurements are the peak positions of the dark MCA spectra (Section 5.2.1). The average SPE pulse heights are shown in Figure 5.17. Uncertainties are only visible for the mean of the LED triggered spectra, and are the standard deviation (sigma) of the Gaussian function fit to the spectrum. This standard deviation is the best measurement of dispersion of PMT signal amplitudes attributed to SPE and is applicable as the uncertainty to all of the measurements of average SPE pulse amplitude done. The uncertainties in the measurements are very small since they are statistical in nature and the sample size is very large. Peak-to-valley ratios show a very significant improvement over those found from the dark spectra, however, accurately identifying the position of the valley at low HV is not possible since the amount of noise is small. The peak-to-valley ratios at higher HV follow the same trend as the dark spectra, described in Section 5.2.1 and seen in Figure 5.7.

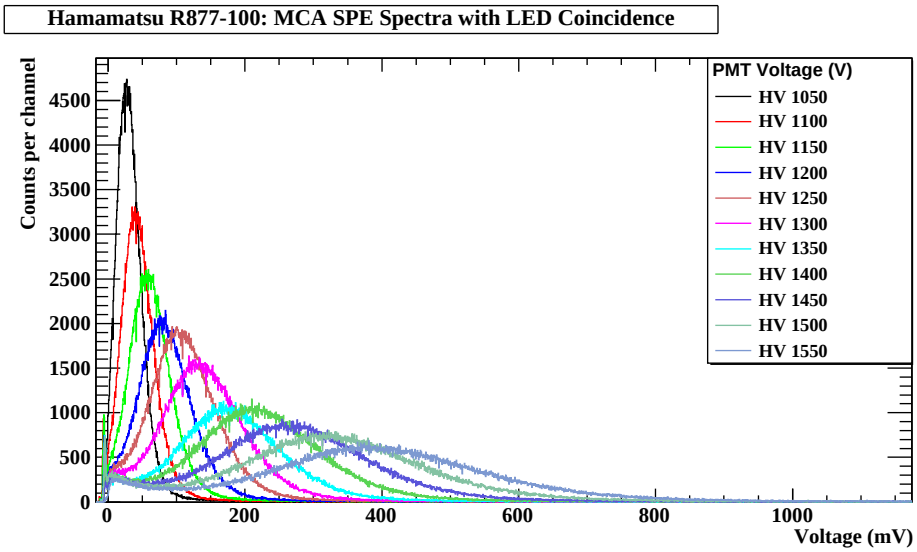

Figure 5.15: With the SPE trigger setup and an LED flasher, the pulse height spectra from the Hamamatsu R877-100 SBA PMT for different operating voltages.

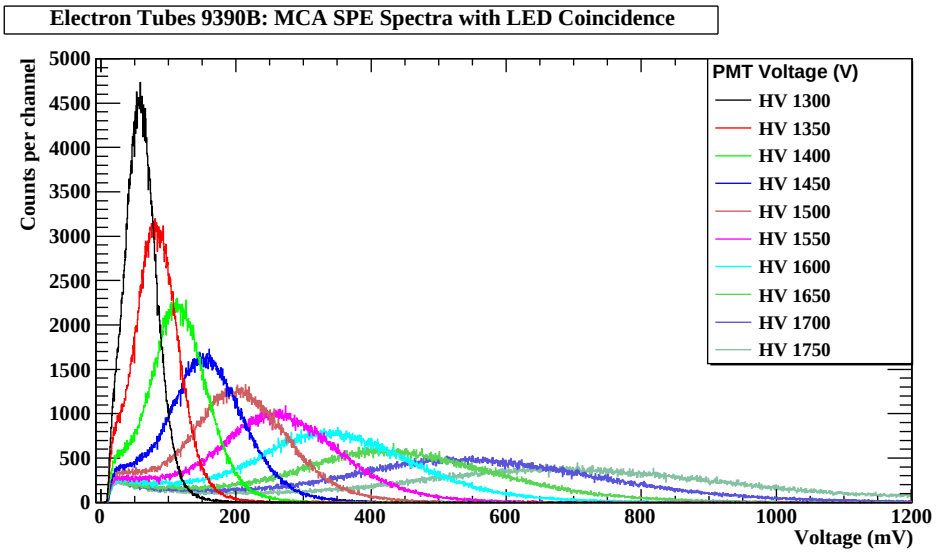

Figure 5.16: With the SPE trigger setup and an LED flasher, the pulse height spectra from the Electron Tubes 9390B PMT for different operating voltages.

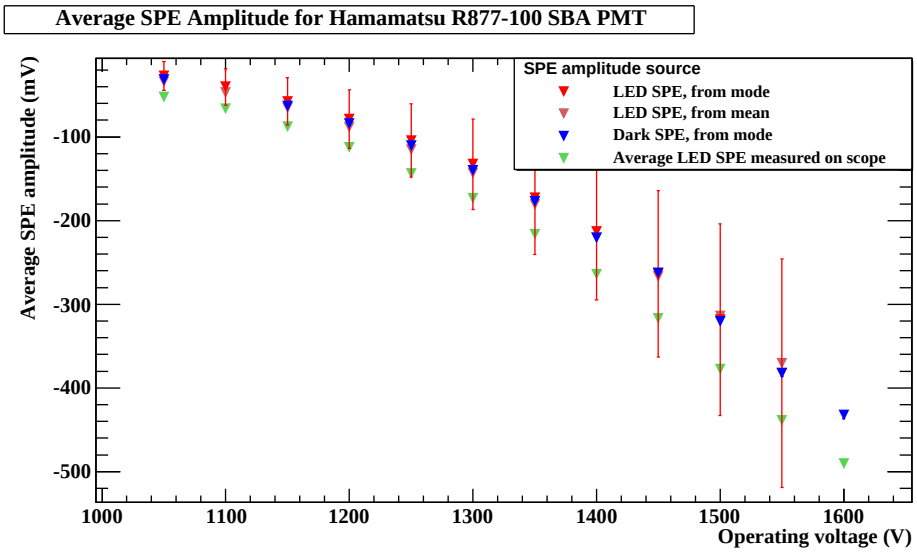

Figure 5.17: Average SPE amplitudes determined from analysing pulses averaged with an oscilloscope and by integrating the MCA data, both dark and in coincidence with the LED, Hamamatsu R877-100 SBA PMT.

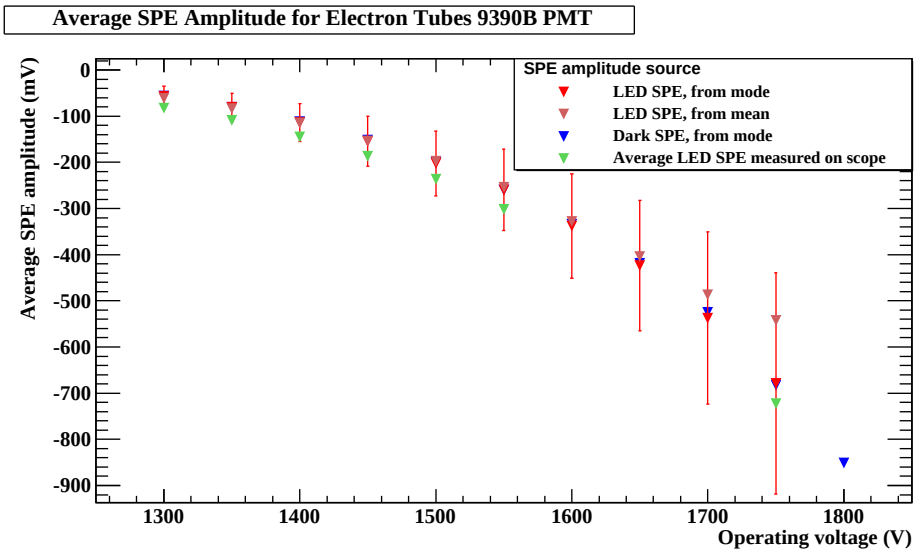

Figure 5.18: Average SPE amplitudes determined from analysing pulses averaged with an oscilloscope and by integrating the MCA data, both dark and in coincidence with the LED, ET 9390B PMT.

PMT responses that are not due to the LED may still trigger the coincidence setup and be counted. The test was additionally run with the LED disconnected and a spectrum of only dark pulses in coincidence with the LED pulser was obtained. The event rate is very small, < 0.1 kHz for every HV. Once the spectra are smoothed, the trend appears to follow that of the dark spectra observed in Section 5.2.1 as one would expect. There are too few pulses in the time intervals used to affect the shape of the SPE spectra. To determine whether the noise observed in the SPE spectra was due to the LED, such as residual light from previous pulses, or our electronics, the dark pulse spectrum was scaled so that the signal peaks were aligned and the LED spectrum was subtracted:

$$N_n(V) = sN_d(V) - N_S(V) \tag{5.1}$$

where $N(V)$ represents a pulse height spectrum, s is the scaling factor, and the subscripts n, d, and S represent noise, dark, and SPE, respectively. At higher amplitudes than that of an SPE, a positive difference remains in the spectrum. This consists of large amplitude signals due to multiple SPE and must be composed of several Gaussian distributions corresponding to 2 pe, 3 pe and so on. The difference is shown in Figure 5.19. Note the asymmetry in the remaining peak to the right of the SPE peak. What is surprising in this analysis is the remaining event to the left of the SPE peak, since they cannot be attributed to fractions of a pe. Suspecting that the LED may be producing these events through electronic coupling, the noise spectrum taken with the LED disconnected was smoothed and also scaled to the height of the SPE spectra and had the SPE spectrum subtracted (also seen in Figure 5.19). This shows that the noise artifacts are present independently of the LED and are intrinsic to the detector and our electronics. To see whether such events are due to the PMT, the same analysis was carried out with the ET PMT spectra. In Figure 5.20 the same features can be seen to a lesser extent. A

noticeable distinction of the ET PMT is that the widths of the dark spectra and the LED coincidence spectra are very similar, when the difference of the two is taken the result is very diminutive compared to that of the Hamamatsu PMT. Since both tests were performed under conditions designed to be as similar as possible, the much larger difference between the SPE spectrum and the dark spectrum seen in the Hamamatsu PMT, Figure 5.19, must also be partially due to noise. If the remaining peak was due to two or three pe, a similar number of events would be visible in Figure 5.20 for the ET PMT, provided the test setups were similar enough for a source to be the same for each PMT.

The implication of this analysis is that the Hamamatsu has the ability to produce noise at amplitudes over the range of SPE pulses. This will be problematic for DEAP-3600, since the larger noise pulses will be difficult to identify and correct for (in terms of the baseline). The larger amplitude also has a larger effect on F_{prompt} calculations. Near 50 mV, the portion of the spectra between the low amplitude noise and the SPE amplitude exhibits a similar linear trend, but it is very small and distinct from a spectrum of noise events below the SPE amplitude, which peaks at about 100 mV. This suggests that some events in this low amplitude region may be attributed to the electronics but the large effect seen in Figure 5.19 must largely be due to the Hamamatsu PMT. Dark noise in the PMTs comes from many sources, the most significant is thermionic emission of electrons from the photocathode and dynodes, which is dominant near the nominal operating voltage and increases exponentially with operating voltage. At very low voltage ohmic leakage (current passed to the anode via imperfect insulation) is significant, but likely not applicable in this case. At very high voltage field emission, the emission of electrons from dynodes due to the strong electric fields, becomes prominent. Other noise sources such as gamma rays, scintillation in the glass envelope, ion feedback, or radiation from

impurities in the glass are other not considered significant in comparison, generally. The most likely increase is due increased thermionic emission from the new material used for the SBA photocathode, combined with differences in the Hamamatsu's geometry. The R877-100's dynode structure, focusing electrode (which helps steer photoelectrons from the photocathode to the first dynode), and the geometry of the glass envelope before the dynodes all may contribute to an increased probability that an electron released by thermionic emission may produce the same signal as a photoelectron. Furthermore, this result may imply a lower uniformity of the Hamamatsu PMT, where photoelectrons emitted from a different area of the photocathode produce position-dependent noise amplitudes. The triggered SPE spectrum is inherently uniform, the LED is in a fixed position and incident photons are always focused on the centre of the photocathode. Dark noise, on the other hand may come from a source at any point on the glass envelope, such as thermionic emissions from the sides, rather than the photocathode, which may be amplified. Tests of uniformity should be undertaken with the Hamamatsu R5912 HQE PMTs currently installed in DEAP-1.

5.2.4 Averaged Waveforms and Baseline Determination

The baseline is the portion of a waveform before a pulse. An important quantity for accurate F_{prompt} calculation is how well the waveform returns to the baseline after a pulse. The average waveform after a pulse can be offset from the baseline by a small percent of the pulse amplitude. This is often a negligible effect, but becomes significant when occurring thousands of times for each SPE in a DEAP event. Currently, the F_{prompt} for DEAP-1 is calculated by integrating the waveforms. If the baseline shifts over the range of integration, the integrated charge due an SPE late in the tail will not be equivalent to that in the prompt region, which directly affects F_{prompt}. The baseline effects due to

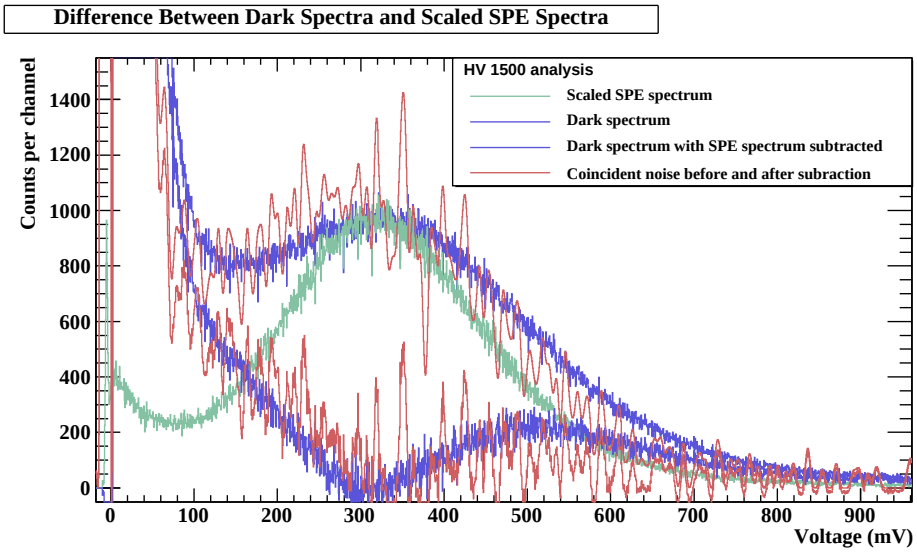

Figure 5.19: Analysis of noise sources by examining the difference between a spectrum taken with the LED in coincidence and a spectrum taken dark. The results of the same analysis taken with dark noise pulses in coincidence with the LED pulser is also shown. Performed on data collected for the Hamamatsu R877-100 SBA PMT.

the DEAP-1 PMTs have been measured and the changes are subtracted along the waveforms before F_{prompt} is calculated. Another important factor is how quickly the pulse will return to the baseline. If the pulse is too slow to return, it can affect the next pulse, changing its amplitude and therefore impacting the number of pe detected. Signal processing boards are being developed for DEAP-3600 PMTs that will minimise these effects. It is important, therefore, to understand whether the effects I see in these tests are due to the electronics used to test the PMTs, or the PMTs themselves.

While measuring the SPE pulse height spectrum (Section 5.2.3), pulses were also averaged and stored with an oscilloscope. The oscilloscope had channels devoted to the same inputs as the logic unit; the discriminators for the LED pulser and the PMT. An internal logic function was used for the trigger, which used these inputs. The oscilloscope was used for both quality control and to set up the logic unit that triggers the MCA. This involved

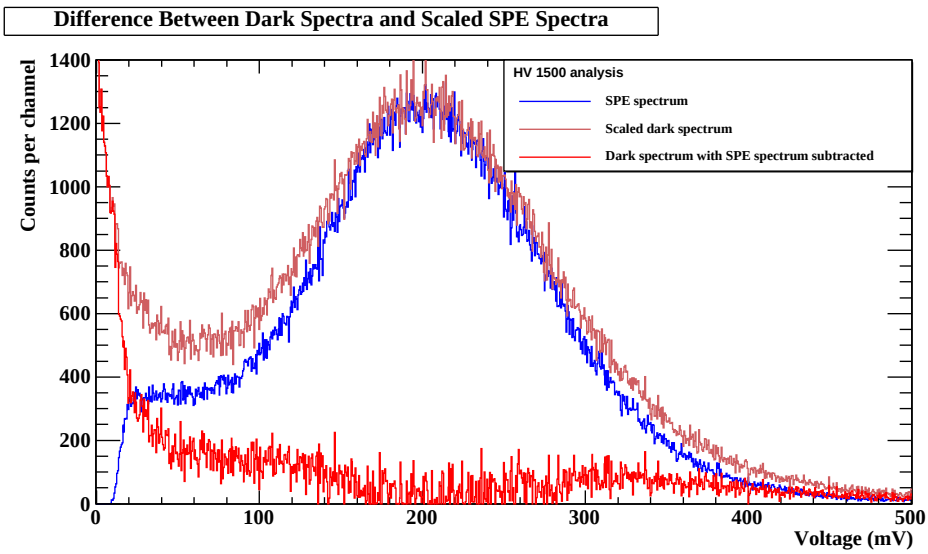

Figure 5.20: A comparison of the analysis presented in Figure 5.19 done with the ET 9390B PMT. An examination of the difference between a spectrum taken with the LED in coincidence and a spectrum taken dark.

adjusting gate widths and pulse widths to ensure that the LED pulser and the PMT discriminator occur within the same time interval, and ensuring that the number of missed pulses was minimised. The coincidence circuit's performance was evaluated using the oscilloscope's logic. An average of 10,000 waveforms was created and analysed in ROOT. Waveforms were recorded both for the linear amplifier and the preamplifier for the Hamamatsu PMT (the linear amplifier was not used with the ET PMT). The voltage per division on the oscilloscope was kept constant and was set such that at large HV, high-amplitude pulses would not be clipped on the oscilloscope. To see the full pulse tail and make good measurements of the baseline, traces were made 5 μs long, and the rate of LED pulses was 100 kHz (one pulse every 10 μs). The traces were stored with 5000 points in 100 divisions of 50.0 ns, which corresponds to 1.00 giga-samples per second. Pulses are $\approx$ 150 ns wide and their tails are characterised by a non-smooth undershoot. A sample of pulses for different HV (increasing HV corresponding to increasing pulse amplitude) for both PMTs

is shown in Figure 5.21. The common preamplifier produces very similar pulse risetime in both PMTs. The most notable difference between the two is the much longer tail of the ET waveforms. The preamplifier was designed to create as close to a Gaussian-shaped pulse as possible for the Hamamatsu PMT. The longer fall time of the ET PMT is due to greater overall charge stored in the PMT and transferred to the electronics, a result of the high gain.

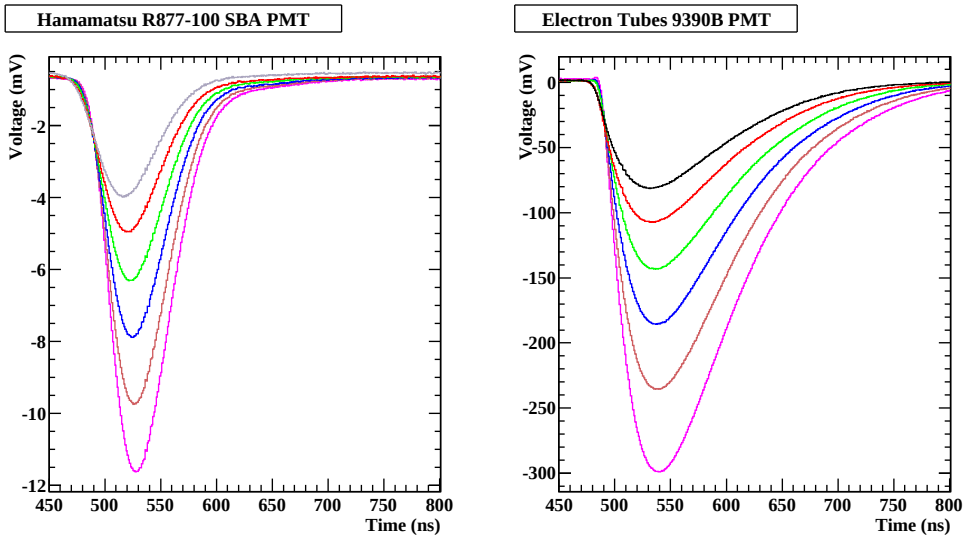

Figure 5.21: A sample of the average waveforms due to SPE taken with the oscilloscope for increasing HV. The ET PMT exhibits a much longer fall time than the Hamamatsu PMT and has a long tail. The risetime is dominated by the preamplifier and the fall time is dominated by the PMTs.

Attempts to fit an exponential function generally fail (large χ^2/ndf) due to features at the end of the pulse. Upon comparing the pulses from both the Hamamatsu and ET PMTs similarities in tail shape are seen. The portions of the waveform that are the same can be attributed to the electronics common to both PMTs, mainly the preamplifier. Effects are much more visible in the Hamamatsu PMT because of its lower gain. The signal from the ET PMT is much larger than the baseline effects due to the electronics and so the baseline effects are less visible. Because of this, the effects are easiest seen

at low HV on the ET PMT, whereas they become more observable at higher HV on the Hamamatsu PMT with increasing gain. When operating the ET PMT at very high HV fluctuations in the baseline are observed which are caused by overloading the preamplifier as seen in Section 5.2.3. A qualitative investigation can be done by directly comparing a waveform from each PMT. For maximum visibility of the features, a low HV ET waveform and a high HV Hamamatsu waveform are presented in Figures 5.22 and 5.23. The Hamamatsu waveform has been scaled to the same amplitude as that of the ET PMT for comparative purposes and the baselines prior to the pulse are normalised to correspond to zero. Figure 5.22 shows the entire pulses with a narrow time scale. An exponential function is fit to both pulses. The longer tail of the ET PMT's pulse follows its fit line well signifying that the pulse returns to the baseline in a smoothly exponential fashion. The tail of the SPE pulse of the Hamamatsu PMT, on the other hand, shows immediate signs of a non-exponential decay. There is instead a portion of the pulse that looks linear between 600 and 700 ns where the curve has flattened out before returning to the baseline.

Figure 5.23 takes a closer look at the features by expanding the time range and reducing the range of the voltage axis to regard the pulse noise. The difference between the fit line and the SPE waveform produced by the Hamamatsu PMT is greatly exaggerated with these axis limits. The features that do not follow an exponential trend are clearly visible and are followed by a slow rise back to the baseline. The shape of the features can also be seen in the SPE waveform produced by the ET PMT at these scales, although they are much larger and have a much longer time range. The baseline effects must be due to the common electronics and can be reduced in future versions on the preamplifier or signal processing boards. The increased magnitude of the effects seen when using the ET PMT suggests that the effects are charge de-

pendent and are of greater concern when using PMTs with high gain. The effects prevent analytic baseline calculations which would be used to correct data from either DEAP-1 or DEAP-3600. An event waveform from the detectors would consist of a great number of SPE pulses and each would contribute to the overall baseline, so even a small effect would need to be corrected for. Baseline corrections are currently numerically evaluated using detector data.

5.2.5 Gain

A measurement of the gain of both PMTs at different HV was made by integrating averaged waveforms to determine the charge of an SPE. To eliminate the effects of pulse shaping, the preamplifier was not used for this calculation and only raw pulses were integrated. Since the raw PMT pulses of the Hamamatsu PMT are too small to accurately measure it was analysed with the linear amplifier, which does not change the shape of the incoming pulses. The gain of the linear amplifier was measured using the averaged SPE waveforms from Section 5.2.4. As the averaged waveforms were collected, the smaller waveforms from the preamplifier were also collected and averaged in parallel. The pulse amplitudes of both amplifiers were compared, and a linear function was fit to the data. The fit showed that output pulses were 16.14 ± 0.05 times larger than the input pulses, with an offset of 3.9 ± 0.9 mV.

Waveforms for SPE are obtained using the LED and coincidence setup at the highest HV used during other tests; 1600 V and 1750 V for the ET PMT and the Hamamatsu PMT respectively. To obtain raw pulses a splitter was used at the PMT with one channel sent to the preamplifier and logic setup, to determine which pulses are due to SPE, and the other channel sent directly to the oscilloscope. The oscilloscope triggers on the amplified pulses like normal, and averages of the raw pulses are made. The waveforms obtained are seen in Figure 5.24, where the larger pulse is that on the Hamamatsu PMT which

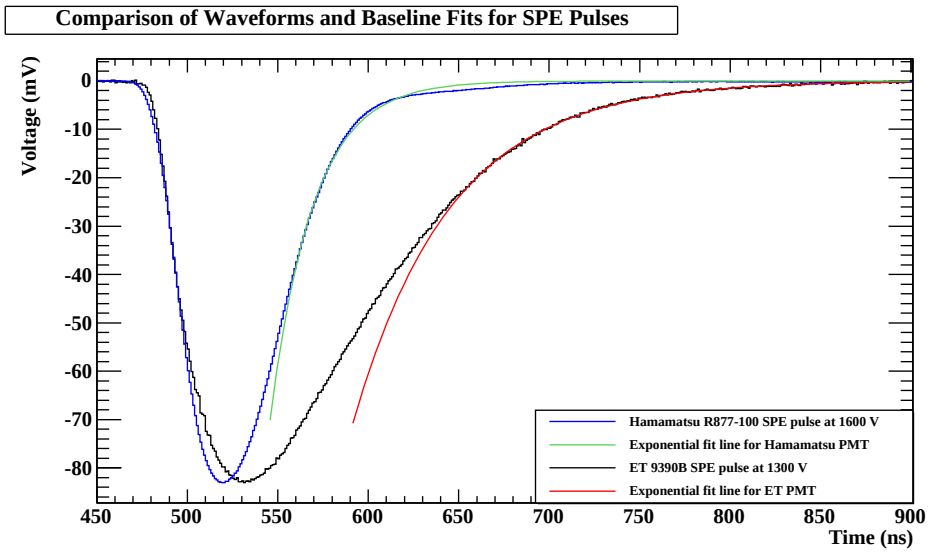

Figure 5.22: A comparison of the SPE waveforms and exponential baseline fits of the Hamamatsu (blue) and ET (black) PMTs. Features preventing reliable fits are clearly visible in the waveform collected for the Hamamatsu PMT. Note the difference in pulse width and fall time.

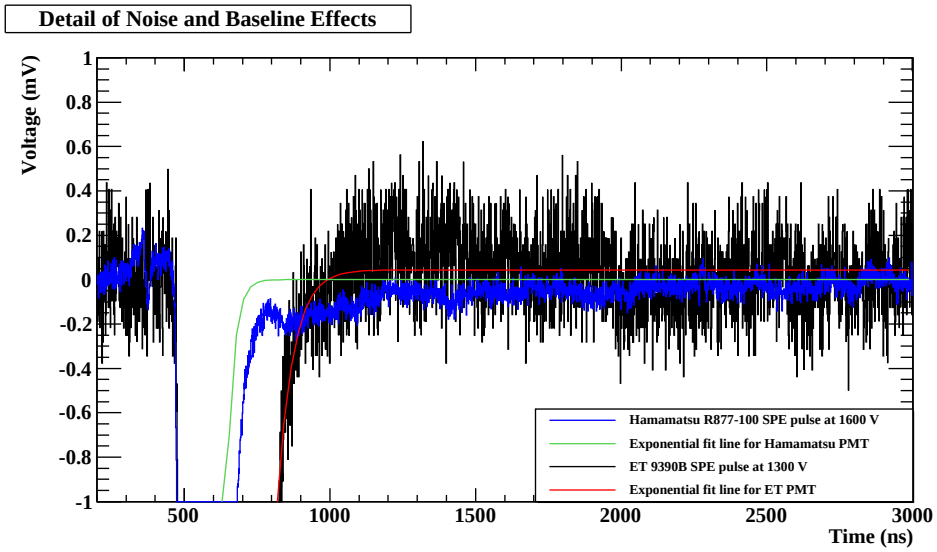

Figure 5.23: Zoom on the y-axis of Figure 5.22, and looking at both the pulses and tails. The same features preventing a baseline fit for the Hamamatsu PMT (near 750 ns) can be seen in different proportions on the ET PMT (between 900 and 1500 ns). Issues with the Hamamatsu PMT's baseline fit are exaggerated at this scale. Noise caused by the high current LED pulser is visible at 350 ns.

passes through the linear amplifier. Note the jagged shape and large overshoot of the raw ET PMT pulse, these characteristics are generally seen in single ET waveforms.

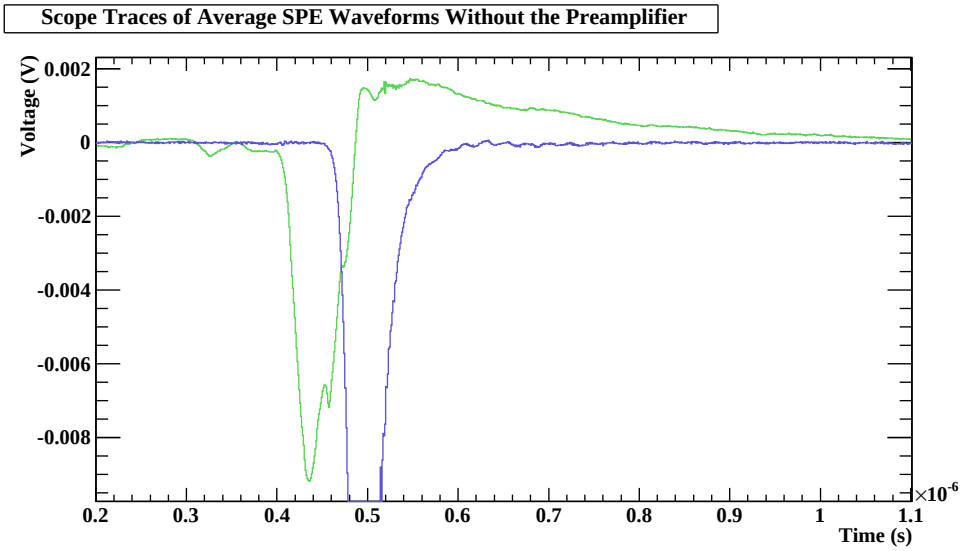

Figure 5.24: Averaged raw pulses from the Hamamatsu PMT (blue) and the Electron Tubes PMT (green).

The oscilloscope traces are the time-dependent voltage $V(t) = I(t)R$ of the averaged pulse and are related to current $I = dQ/dt$. The average charge produced in a PMT due to an SPE is calculated by integrating the averaged waveforms.

$$Q = \int \frac{V(t)}{R}\, dt \tag{5.2}$$

The number of electrons that must be accelerated inside the PMTs by an SPE to produce the observed charge is the gain:

$$G_{PMT} = \frac{\int V(t)\, dt}{eRG_{amp}} \tag{5.3}$$

where e is the electric charge and G_{amp} is the gain of any amplifiers used: 1 for the ET PMT and 16.14 for the Hamamatsu PMT.

For the Hamamatsu PMT the gain at 1600 V was found to be $7.52 \pm 0.08 \times 10^6$ and for the ET PMT the gain at 1750 V was found to be $5.45 \pm 0.05 \times 10^7$.

As expected there is an order of magnitude difference. How the gain varies with HV will follow that of the average SPE amplitude and is shown in Figures 5.25 and 5.26. Hamamatsu reports a typical gain for the R877-100 of 3.1×10^5 [144] at 1250 V which is about one fifth of our projected measurement of $1.5 \pm 0.1 \times 10^6$ at the same HV. Electron Tubes reports a typical gain of $2.7 \pm 0.1 \times 10^6$ for its 9390B PMT when operating at 1000 V [145]. Our measurements do not reach such a low HV, but our projection suggests that the gain will be $< 4.6 \times 10^6$, the measurement at our lowest HV of 1300 V. Both of the reported values for gain are lower than those I measured but within a small enough range to be acceptable. This discrepancy is acceptable since there is very little known about the test methods used by Electron Tubes and Hamamatsu and we are not using standard bases which affects the gain. It is known that the PMTs are produced with varying characteristics.

5.2.6 SPE Efficiency

The SPE efficiency is a measure of how easily the PMT can identify SPE at different operational voltages. For this set of measurements the light source is kept constant, and the number of SPE that the PMT detects is studied. At lower HV photons are still incident on the PMT but many go undetected, which is undesirable for F_{prompt} calculation. If the SPE efficiency drops off at a certain HV, DEAP experiments could not effectively deploy PMTs operating below that voltage.

To measure the SPE efficiency we use the LED pulser and the coincidence setup described in Section 5.2.3. At nominal voltage the LED amplitude is adjusted until the ratio of PMT responses to LED flashes is $\approx 1/50$. Efficiency of the PMT varies with HV and is reflected by the changing rate of PMT responses, R, for a fixed LED rate ($R_{LED} = 100$ kHz). The HV is varied and the change in ratio is recorded. As discussed in Section 5.2.2, data taken

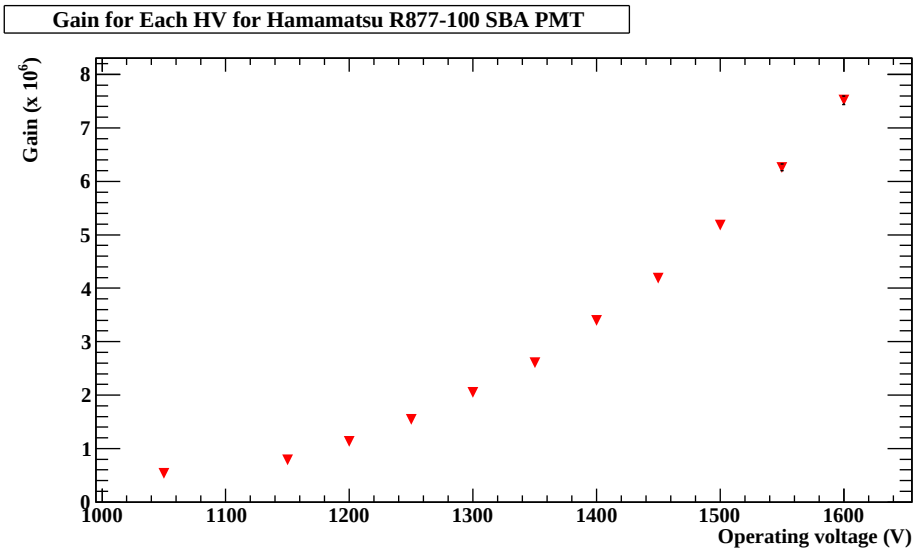

Figure 5.25: Gain of the Hamamatsu R877-100 SBA PMT for different operating voltages.

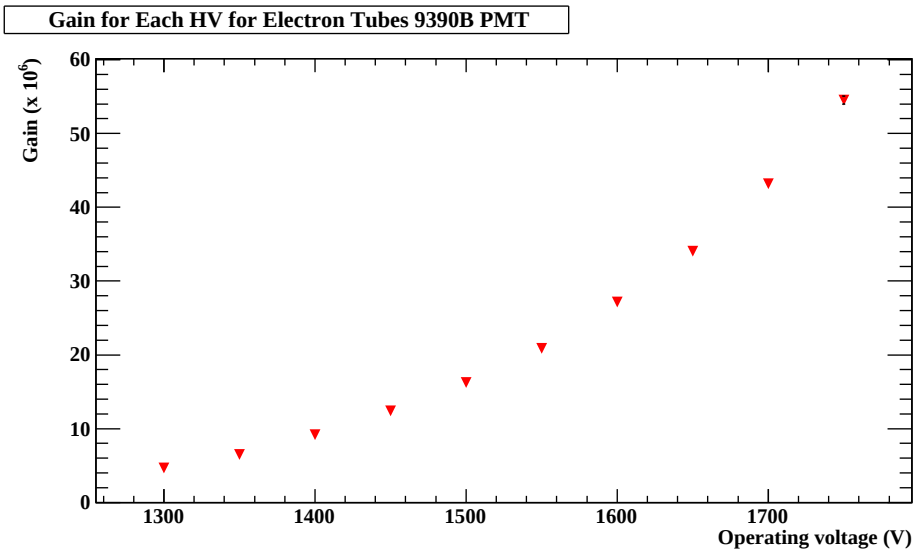

Figure 5.26: Gain of the Electron Tubes 9390B PMT for different operating voltages.

with the counter is subject to the constant threshold of the discriminator. A correction factor is derived from the ratio of total PMT pulses to PMT pulses above a floating threshold. These values, I_{tot} and I_{thresh}, are determined by integrating the MCA spectra taken in coincidence with the LED (Section 5.2.3). The corrected rate from the counter becomes:

$$R \rightarrow R' = R\frac{I_{thresh}}{I_{tot}} \tag{5.4}$$

$$\Rightarrow Eff = \frac{R}{R_{LED}} \rightarrow Eff' = \frac{R'}{R_{LED}} = \frac{R}{R_{LED}}\frac{I_{thresh}}{I_{tot}} \tag{5.5}$$

The threshold used in integration is 1/2 of the position of the SPE peak. The position of this floating threshold is arbitrarily chosen, but suitably reflects the a proportion of pulses not counted by the counter due to the discriminator threshold and modifies the ratio found by the counter to account for a greater amount of low amplitude pulses being ignored by the coincidence setup at lower HV. Results are plotted in Figures 5.27 and 5.28. Changes are generally very small, but, are greatest between lower voltages. For the Hamamatsu PMT, the ratio varies within a range of only 1/49 to 1/55 LED responses per PMT flash while the ET PMT exhibited larger range 1/45 to 1/58.

5.2.7 Time Resolution

The difference in time between the LED flash and the PMT response is generally larger than the width of the amplified PMT pulse and varies with HV. A TPHC was used to create a spectrum of pulse widths to determine how the time difference varies with HV, and how wide the range of signal delays is for each HV. The signals from the LED pulser and the PMT discriminator were run into the TPHC, and the TPHC output was collected by another MCA, a Spectrum Techniques UCS-30 universal computer spectrometer (see Figure 5.29). The change was made to accommodate the large amplitude and width of the TPHC output pulses and to use more standard pulse shaping. The signal

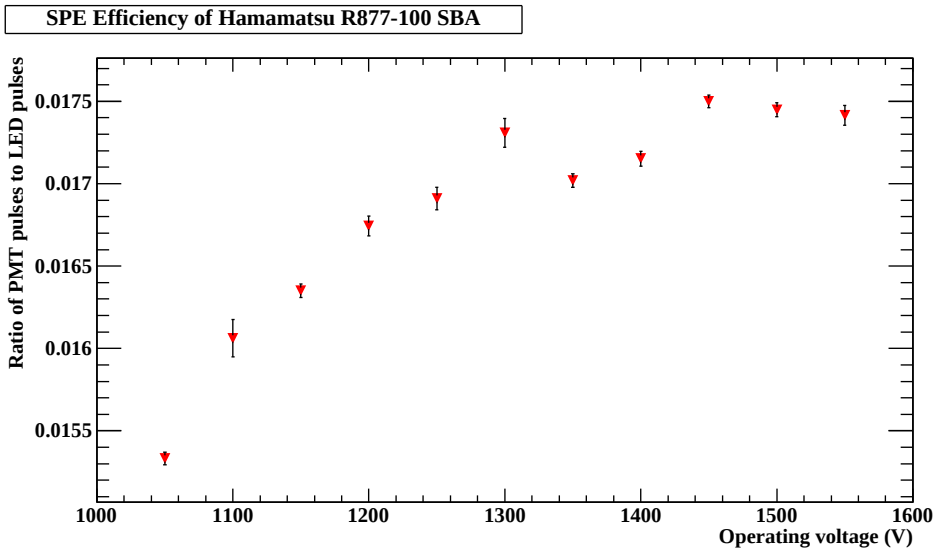

Figure 5.27: Relative efficiency of Hamamatsu R877-100 SBA PMT determined from the ratio of PMT responses to LED pulses for each HV corrected for deadtime.

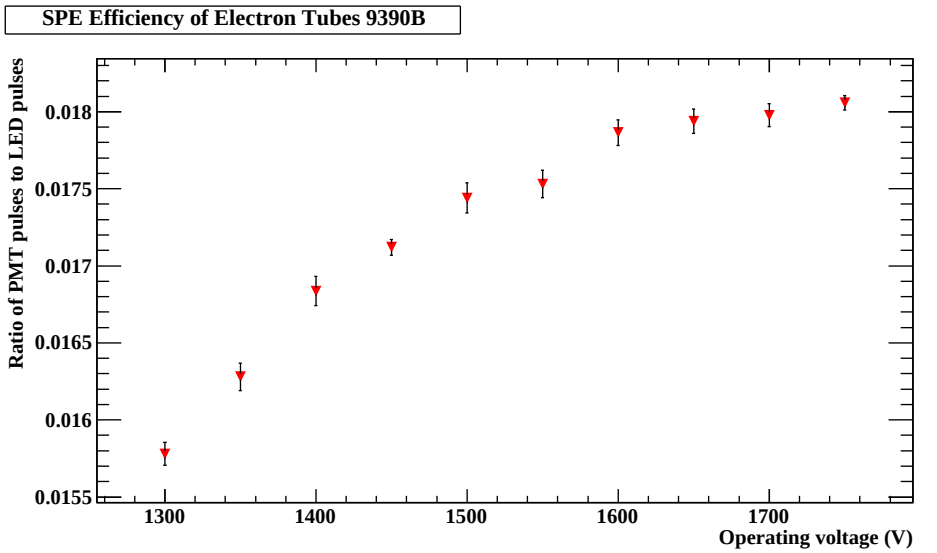

Figure 5.28: Relative efficiency of Electron Tubes 9390B PMT determined from the ratio of PMT responses to LED pulses for each HV corrected for deadtime.

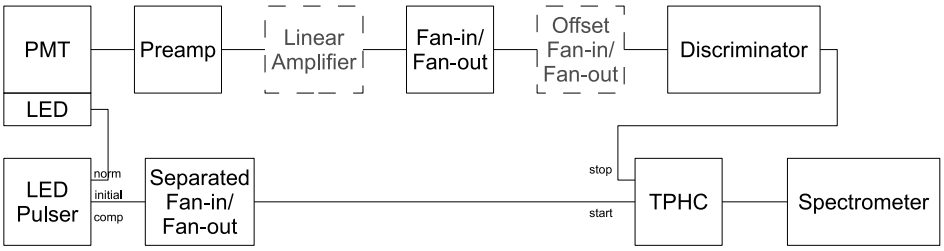

Figure 5.29: A simplified flowchart of the DAQ setup for measuring the time resolution of the PMTs using a TPHC.

from the LED uses the 'start' input which tells the TPHC to begin looking for a pulse from the PMT discriminator in the 'stop' input. The TPHC produces a pulse whose amplitude depends on the time interval between the two measurements. In order to understand the relationship between the pulse heights and the time difference the UCS spectrometer was calibrated by using a delay generator and the PMT discriminator. The discriminator pulse was sent to the TPHC 'start' and a second discriminator output was delayed and then sent to the TPHC's 'stop' input. The time difference between the two discriminator pulses was measured with an oscilloscope, allowing the calculation of a calibration factor of 0.185 ± 0.001 ns/channel with an offset of -21 ± 1 channels. Since the trigger places a restriction on the time interval width, none is used, although the LED is used to produce SPE in the same manner as other tests.

The collected spectra for the two PMTs are shown in Figures 5.30 and 5.31. The behaviour of the PMT response for both PMTs is characterised by a fast risetime and long tail which will contain noise pulses. The background is flat since noise pulses occur at random times after the LED flash. The spectra imply that there is a fixed delay between an event and the response of PMT - at a given HV a pulse within this time interval cannot be attributed to the event. The slower falltime indicates that later pulses should be expected. The

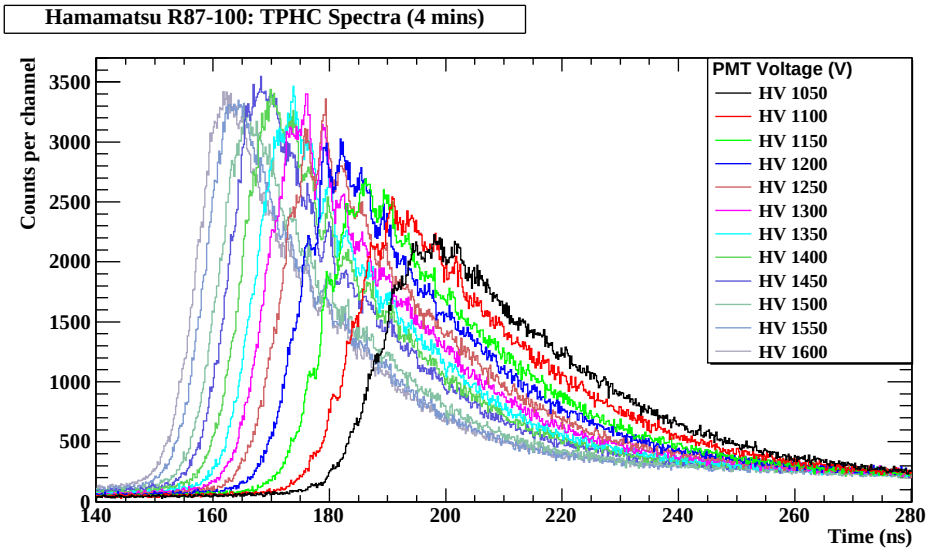

Figure 5.30: Spectra of time differences between the LED flash and the PMT response for the Hamamatsu R877-100 PMT. The time difference is shorter as HV increases. The tail settles to a flat line corresponding to a background of random pulses at any time.

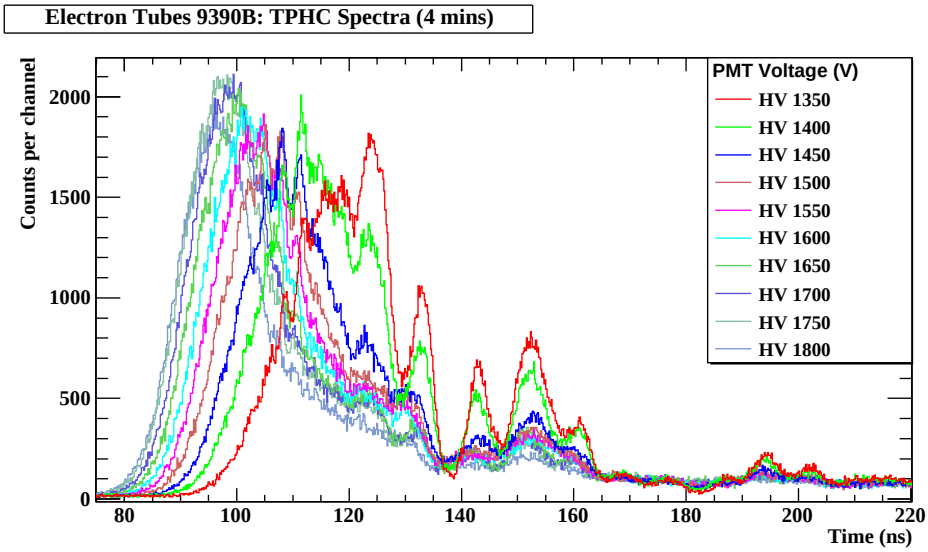

Figure 5.31: Spectra of time differences between the LED flash and the PMT response for the Electron Tubes 9390B PMT. A very distinct source of noise is highly visible that occurs at the same channels of the UCS independent of the PMT HV. This is likely due to cable reflections between the TPHC and the UCS and is also visible in Figure 5.30.

Hamamatsu PMT has the slower response of the two, with a shortest time interval of 162 ± 5 ns at 1600 V and a longest time interval of 197 ± 8 ns at 1050 V. Comparatively, the ET PMT's responses are between 96 ± 6 ns and 119 ± 9 ns at operating voltages of 1800 V and 1300 V, respectively. A significant source of noise shows up in the spectra collected for the ET PMT. The noise peaks occur at the same channel for each HV and is likely due to an undetected signal reflection either between the UCS and the TPHC. This behaviour was undetected on the oscilloscope prior to making the measurements. The noise is very large at low HV when using the ET PMT which renders calculations made between 1300 V and 1400 V unreliable.

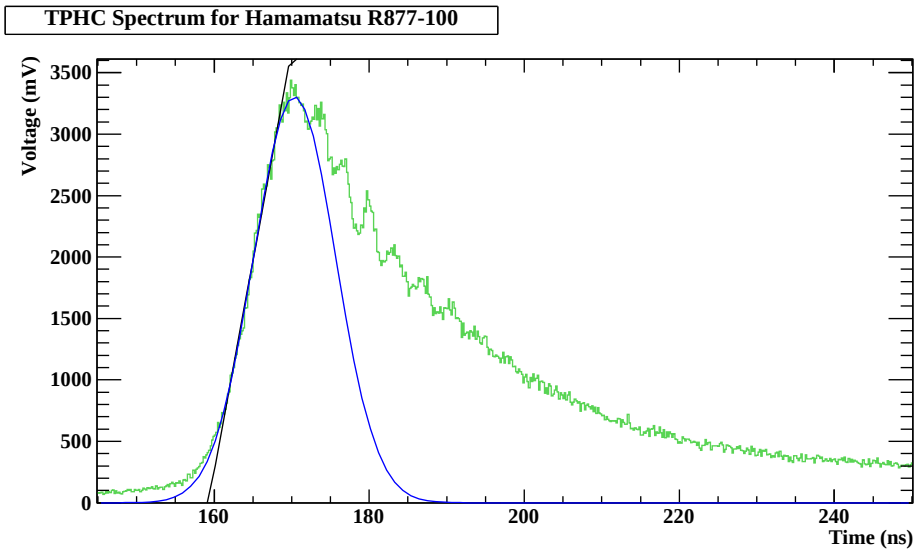

Figure 5.32: An example of the fits made to a TPHC spectrum. A line is fit between 10% and 90% of the peak amplitude to measure the risetime. A Gaussian function is fit to the rise of the peak to measure its width which corresponds the range of time differences to expect at a given HV. This spectrum was from the Hamamatsu PMT operating at 1150 V.

The risetimes of the spectra were calculated by fitting a straight line to the rise of the peak. A standard range of between 10% and 90% of the peak amplitude was used. From the slope of the fit line the time displacement over the range is taken to be the risetime. This risetime measurement is dominated

by the preamplifier, and is similar for both PMTs. An example of the fits and analysis done with the TPHC spectra is shown in Figure 5.32. For both PMTs the risetime becomes smaller with increasing HV. The range of risetimes for both PMTs is only $\approx$ 4 ns and the value levels off above the nominal operating voltages for both PMTs. The trend of the calculated risetimes for the Hamamatsu PMT is shown in Figure 5.33 and that of the ET PMT is shown in Figure 5.34. The Hamamatsu PMT has a faster risetime in general with a range of between 12.6 ± 0.2 ns at 1050 V and 7.8 ± 0.1 ns at 1600 V. The risetimes measured for the ET PMT range from 13.8 ± 0.5 ns at 1800 V to 10.5 ± 0.1 ns at 1300 V.

The second measurement was made to characterise the range of time differences between the LED and PMT events. It was known that the time difference was non-steady as discussed in Section 5.2.3. Previous measurements took this into account by allowing for coincidences to be counted within a small interval. The spectra in Figures 5.30 and 5.31 allow for a good measurement of the range of time differences to expect. A Gaussian function was fit to the rising edge of the peak and its calculated sigma (or width) is taken to be the expected range of time differences expected with a high certainty that the event is not noise. The results are plotted in Figures 5.35 and 5.36 for the Hamamatsu and ET PMTs, respectively. At higher HV the response is faster and the widths are smaller. The widths calculated for the Hamamatsu PMT are between 5.38 ± 0.03 ns at 1600 V and 7.9 ± 0.1 at 1050 V. The widths of the ET PMT are slightly larger, between 6.41 ± 0.04 ns at 1800 V and 8.8 ± 0.2 ns at 1300 V.

5.3 Closing Remarks

The Hamamatsu super-bialkali R877-100 PMT behaves well for a wide range of operating voltages. The PMT obeys an exponential relationship between

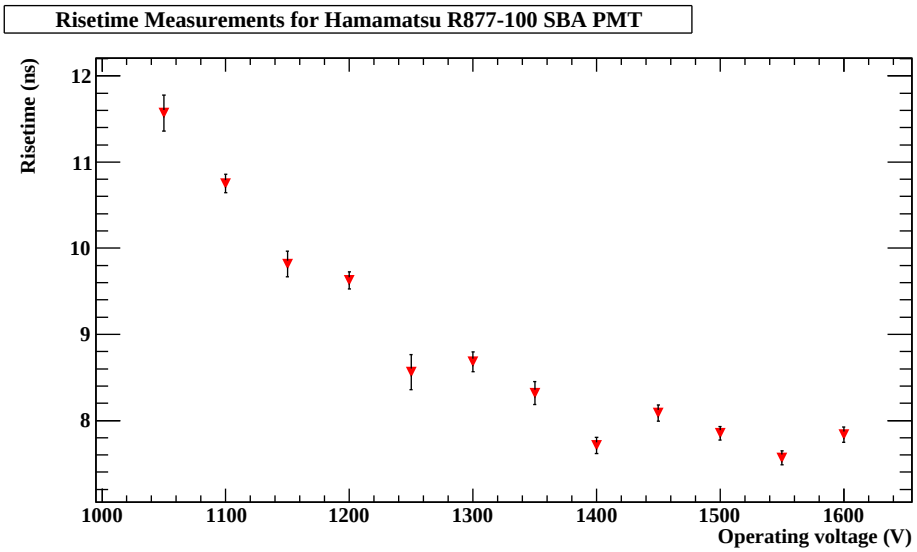

Figure 5.33: Risetime measurement for the Hamamatsu R877-100 SBA PMT calculated from the spectra collected using the TPHC.

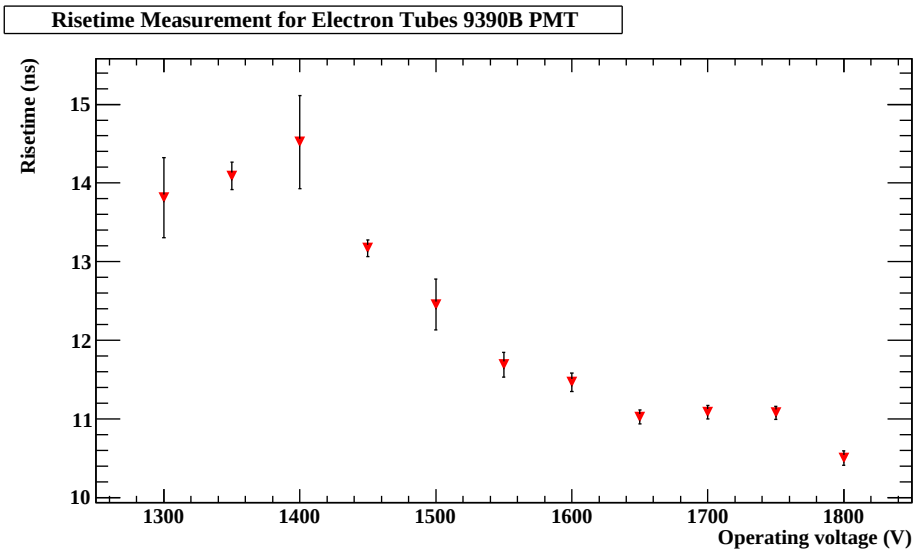

Figure 5.34: Risetime measurement for the Electron Tubes 9390B PMT calculated from the spectra collected using the TPHC.

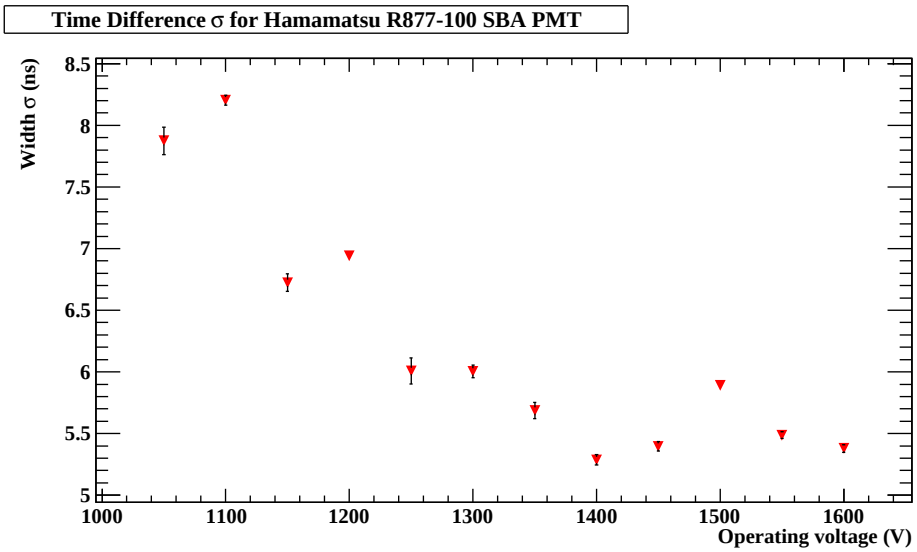

Figure 5.35: Widths of the TPHC spectra measured for the Hamamatsu R877-100 SBA PMT by fitting a Gaussian curve to the rising edge of the spectra in Figure 5.30. The width represents the range of time differences between two similar events.

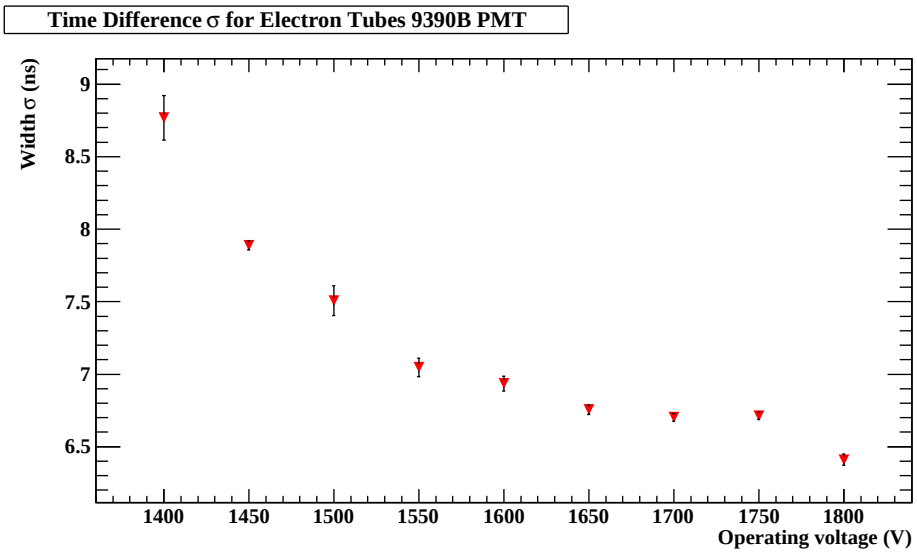

Figure 5.36: Widths of the TPHC spectra measured for the Electron Tubes 9390B PMT by fitting a Gaussian curve to the rising edge of the spectra in Figure 5.31. The width represents the range of time differences between two similar events.

operating high voltage and both dark pulse rate and gain. The range of dark pulse rates observed is between 2.04 ± 0.02 and 13.2 ± 0.3 kHz and is greater than for the R1408 SNO PMTs, which had a range less that 5 kHz [146]. At the nominal operating voltage and below the R877-100 PMT stays within a noise threshold below 10 kHz. The Electron Tubes 9390B PMT is much quieter, with a range of 1.29 ± 0.01 to 6.70 ± 0.05 kHz. The increased efficiency of the Hamamatsu PMT should offset the larger noise by providing an increase in light collection capability. The ET PMT has larger peak-to-valley ratios and its noise is of lower amplitude independent of HV. It also has a faster response time on the order of 100 ns compared to nearly 200 ns for the Hamamatsu PMT. At higher operating voltages the PMTs respond quicker but have lower energy resolution characterised by wide peaks in their spectra. The differences are well understood, however, and the slower response of the Hamamatsu R877-100 PMT should not be a problem for the applications we are considering. This PMT follows a strongly linear relationship between the magnitude of the source and its output voltage. The higher efficiency will improve the sensitivity and light yield of our detectors and should not present many difficulties in its operation and analysis.

Chapter 6

Conclusion

DEAP-3600 aims to either set the next lowest limit on WIMP scattering cross-sections or make the first measurements of, and first direct detection of galactic dark matter. It will be the lowest-background WIMP search to date, and among the first to reach tonne-scale. The success of the experiment depends on the PSD and most of the development work revolves around the requirements set by it, including the work presented herein.

In Chapter 3 I analysed high-energy α backgrounds in DEAP-1. My study helped to identify and confirm sources of backgrounds which could interfere with WIMP signals. The result led to improvements to the detector design and construction that will have a direct impact on DEAP-3600. These improvements resulted in a reduction of high-energy, high-F_{prompt} backgrounds by a factor of ten, quite significant. This analysis led also to the conclusion that the ^{22}Na calibration techniques we employ could be improved, since drift was easily noticeable in the high-energy backgrounds: αs presented in Chapter 3, and the Compton edges from βs presented in Chapter 4. A tool was developed to align the Compton edges of background runs which leads to an improvement in energy resolution of 1$\sim$3%, which will significantly improve a WIMP search in DEAP-3600 with continued development. The tool has shown that it can be used to track the light-yield degradation of LAr and monitor other

changes to the detector.

Chapter 5 presented a detailed study of several PMT traits. These characterisations will lead to a benchmark testing regime for the 8" Hamamatsu PMTs that will be deployed on DEAP-3600. The direct comparison of the Electron Tubes 9390B PMTs originally deployed on DEAP-1 and the high-QE Hamamatsu R877-100 super-bialkali PMT has given the collaboration a strong indication of what to expect when moving to high-QE PMTs for DEAP-3600. There are two properties of the SBA PMTs that cause concern which were investigated and measured. The first was a higher dark noise rate, found to be approximately double that of the ET PMT. The second was a slow risetime, which results in slower PMT responses from LED flashes. This was also shown to be about double that of the ET PMT. The dark noise rate has been shown to be within an acceptable range for deployment, 2.7 kHz at nominal voltage. Pulses not observed by both DEAP-1 PMTs are vetoed, and the chance of having noise pulses in the tail of a proper signal will be small. A larger concern with the noise is reflected in measurements of the peak-to-valley ratios, which imply that the Hamamatsu PMT has significantly more noise at increasing HV, which is more likely to cross electronic thresholds and be considered an actual pulse. The voltage response to SPE was very comparable, with similar trends in spectrum widths. Trends in gain, relative efficiency, and SPE amplitude were all similar as well.

DEAP-3600 will be operated with custom built signal processing boards, which will provide pulse-shaping and amplification. It will also be run at slower speeds, to reduce the amount of incoming data. Combined with the smaller amount of light incident on the PMTs, these will be able to accommodate the slower response and lower gain of the Hamamatsu SBA PMT, and the increase in light yield resulting from the increased quantum efficiency will improve PSD, and WIMP sensitivity.

Over the course of this work we have seen reductions to the backgrounds in DEAP-1, improved our analysis methods, and seen the capability of PSD increase by orders of magnitude. Much work is done in preparation for the construction, commissioning, and data analysis of DEAP-3600. To that end, my main focus has been on the PMTs. Understanding the SPE response of the PMTs is crucial to PSD, since any pulse-tail effects will affect F_{prompt} calculations. For instance, larger dark noise rates result in a greater number of noise pulses in an event waveform, almost always in the late light region. Analysis of the 8" DEAP-3600 PMTs is ongoing on site and at collaborating institutions, and a new result for the discrimination power is forthcoming.

Bibliography

[1] Kapteyn, J. C. First attempt at a theory of the arrangement and motion of the sidereal system. *Astrophys. J.* **55**, 302 (1922).

[2] Oort, J. The force exerted by the stellar system in the direction perpendicular to the galactic plane and some related problems. *Bull. Astron. Inst. Netherlands* **6**, 249 (1932).

[3] Zwicky, F. Die Rotverschiebung von extragalaktischen Nebeln. *Helvetica Physica Acta* **6**, 110–127 (1933).

[4] Zwicky, F. Republication of: The redshift of extragalactic nebulae. *General Relativity and Gravitation* **41**, 227–224 (2009). English translation by A. Ehlers.

[5] Briel, U. G., Henry, J. P. & Boehringer, H. Observation of the Coma cluster of galaxies with ROSAT during the all-sky survey. *Astro. Astrophys.* **259**, L31–L34 (1992).

[6] White, S. D. M., Navarro, J. F., Evrard, A. E. & Frenk, C. S. The baryon content of galaxy clusters: a challenge to cosmological orthodoxy. *Nature* **366**, 429–433 (1993).

[7] Kubo, J. M. *et al.* The mass of the Coma Cluster from weak lensing in the Sloan Digital Sky Survey. *Astrophys. J.* **671**, 1466–1470 (2007). 0709.0506.

[8] Okabe, N., Okura, Y. & Futamase, T. Weak-lensing mass measurements of substructures in Coma Cluster with Subaru/Suprime-cam. *Astrophys. J.* **713**, 291–303 (2010). 1001.2402.

[9] van Albada, T. S., Bahcall, J. N., Begeman, K. & Sancisi, R. Distribution of dark matter in the spiral galaxy NGC 3198. *Astrophys. J.* **295**, 305–313 (1985).

[10] Babcock, H. W. The rotation of the Andromeda Nebula. *Lick Obs. Bull.* **19**, 41–51 (1939).

[11] Rubin, V. C. & Ford, W. K., Jr. Rotation of the Andromeda Nebula from a Spectroscopic Survey of Emission Regions. *Astrophys. J.* **159**, 379 (1970).

[12] Rubin, V. C. & Ford, W. K., Jr. Radial Velocities and Line Strengths of Emission Lines across the Nuclear Disk of M31. *Astrophys. J.* **170**, 25 (1971).

[13] Freeman, K. C. On the Disks of Spiral and so Galaxies. *Astrophys. J.* **160**, 811 (1970).

[14] Rubin, V. C., Ford, W. K., Jr. & D'Odorico, S. Emission-Line Intensities and Radial Velocities in the Interacting Galaxies NGC 4038-4039. *Astrophys. J.* **160**, 801 (1970).

[15] Roberts, M. S. & Rots, A. H. Comparison of Rotation Curves of Different Galaxy Types. *Astro. Astrophys.* **26**, 483 (1973).

[16] Einstein, A. Über den Einfluß der Schwerkraft auf die Ausbreitung des Lichtes. *Ann. Phys.* **340**, 898–908 (1911).

[17] Dyson, F. W., Eddington, A. S. & Davidson, C. A Determination of the Deflection of Light by the Sun's Gravitational Field, from Observations Made at the Total Eclipse of May 29, 1919. *Phil. Trans. R. Soc. A* **220**, 291–333 (1920).

[18] Einstein, A. Lens-Like Action of a Star by the Deviation of Light in the Gravitational Field. *Science* **84**, 506–507 (1936).

[19] Zwicky, F. On the probability of detecting nebulae which act as gravitational lenses. *Phys. Rev.* **51**, 679 (1937).

[20] Walsh, D., Carswell, R. F. & Weymann, R. J. 0957 + 561 A, B - Twin quasistellar objects or gravitational lens. *Nature* **279**, 381–384 (1979).

[21] NASA, ACS Science Team & ESA. URL `http://hubblesite.org/gallery/album/the_universe/pr2003001e`.

[22] Bacon, D. J., Refregier, A. R. & Ellis, R. S. Detection of weak gravitational lensing by large-scale structure. *Mon. Not. R. Astron.* **318**, 625–640 (2000). `arXiv:astro-ph/0003008`.

[23] Wittman, D. M., Tyson, J. A., Kirkman, D., Dell'Antonio, I. & Bernstein, G. Detection of weak gravitational lensing distortions of distant galaxies by cosmic dark matter at large scales. *Nature* **405**, 143–148 (2000). `arXiv:astro-ph/0003014`.

[24] Van Waerbeke, L. *et al.* Detection of correlated galaxy ellipticities from CFHT data: first evidence for gravitational lensing by large-scale structures. *Astro. Astrophys.* **358**, 30–44 (2000). `arXiv:astro-ph/0002500`.

[25] Alcock, C. *et al.* The MACHO Project: Microlensing Results from 5.7 Years of Large Magellanic Cloud Observations. *Astrophys. J.* **542**, 281–307 (2000). `arXiv:astro-ph/0001272`.

[26] Tisserand, P. *et al.* Limits on the Macho content of the Galactic Halo from the EROS-2 Survey of the Magellanic Clouds. *Astro. Astrophys.* **469**, 387–404 (2007). arXiv:astro-ph/0607207.

[27] NASA & WMAP Science Team. URL http://map.gsfc.nasa.gov/media/101080/index.html.

[28] Penzias, A. A. & Wilson, R. W. A Measurement of Excess Antenna Temperature at 4080 Mc/s. *Astrophys. J.* **142**, 419–421 (1965).

[29] Samtleben, D., Staggs, S. & Winstein, B. The Cosmic Microwave Background for Pedestrians: A Review for Particle and Nuclear Physicists. *Annu. Rev. Nucl. Part. Sci.* **57**, 245–283 (2007). 0803.0834.

[30] Komatsu, E. *et al.* Seven-Year Wilkinson Microwave Anisotropy Probe (WMAP) Observations: Cosmological Interpretation. *ArXiv e-prints* (2010). 1001.4538.

[31] NASA & WMAP Science Team. URL http://map.gsfc.nasa.gov/media/080999/index.html.

[32] Lange, A. E. *et al.* Cosmological parameters from the first results of Boomerang. *Phys. Rev. D* **63**, 042001 (2001). arXiv:astro-ph/0005004.

[33] Tucker, W. H., Tananbaum, H. & Remillard, R. A. A search for 'failed clusters' of galaxies. *Astrophys. J.* **444**, 532–547 (1995).

[34] Tucker, W. *et al.* 1E 0657-56: A Contender for the Hottest Known Cluster of Galaxies. *Astrophys. J. Lett.* **496**, L5 (1998). arXiv:astro-ph/9801120.

[35] Clowe, D., Gonzalez, A. & Markevitch, M. Weak-Lensing Mass Reconstruction of the Interacting Cluster 1E 0657-558: Direct Evidence for the Existence of Dark Matter. *Astrophys. J.* **604**, 596–603 (2004). arXiv:astro-ph/0312273.

[36] Clowe, D. *et al.* A Direct Empirical Proof of the Existence of Dark Matter. *Astrophys. J. Lett.* **648**, L109–L113 (2006). arXiv:astro-ph/0608407.

[37] Bradač, M. *et al.* Strong and Weak Lensing United. III. Measuring the Mass Distribution of the Merging Galaxy Cluster 1ES 0657-558. *Astrophys. J.* **652**, 937–947 (2006). arXiv:astro-ph/0608408.

[38] NASA, Chandra X-ray Observatory Center & Space Telescope Science Institute. URL http://hubblesite.org/newscenter/archive/releases/2006/39/image/a/.

[39] Milgrom, M. A modification of the Newtonian dynamics as a possible alternative to the hidden mass hypothesis. *Astrophys. J.* **270**, 365–370 (1983).

[40] Milgrom, M. A modification of the Newtonian dynamics - Implications for galaxies. *Astrophys. J.* **270**, 371–384 (1983).

[41] Milgrom, M. A Modification of the Newtonian Dynamics - Implications for Galaxy Systems. *Astrophys. J.* **270**, 384–389 (1983).

[42] Bradač, M. *et al.* Revealing the Properties of Dark Matter in the Merging Cluster MACS J0025.4-1222. *Astrophys. J.* **687**, 959–967 (2008). 0806.2320.

[43] Jee, M. J. *et al.* Discovery of a Ringlike Dark Matter Structure in the

Core of the Galaxy Cluster Cl 0024+17. *Astrophys. J.* **661**, 728–749 (2007). 0705.2171.

[44] Abazajian, K. N. *et al.* The Seventh Data Release of the Sloan Digital Sky Survey. *Astrophys. J. Suppl.* **182**, 543–558 (2009). 0812.0649.

[45] Sloan Digital Sky Survey. URL http://www.sdss.org/includes/sideimages/sdss_pie2.html.

[46] Seldner, M., Siebers, B., Groth, E. J. & Peebles, P. J. E. New reduction of the Lick catalog of galaxies. *Astro. J.* **82**, 249–256 (1977).

[47] de Lapparent, V., Geller, M. J. & Huchra, J. P. A slice of the universe. *Astrophys. J. Lett.* **302**, L1–L5 (1986).

[48] Geller, M. J. & Huchra, J. P. Mapping the universe. *Science* **246**, 897–903 (1989).

[49] Colless, M. *et al.* The 2dF Galaxy Redshift Survey: spectra and redshifts. *Mon. Not. R. Astron.* **328**, 1039–1063 (2001). arXiv:astro-ph/0106498.

[50] Skrutskie, M. F. *et al.* The Two Micron All Sky Survey (2MASS). *Astro. J.* **131**, 1163–1183 (2006).

[51] Jones, D. H. *et al.* The 6dF Galaxy Survey: final redshift release (DR3) and southern large-scale structures. *Mon. Not. R. Astron.* **399**, 683–698 (2009). 0903.5451.

[52] Tegmark, M. *et al.* The Three-Dimensional Power Spectrum of Galaxies from the Sloan Digital Sky Survey. *Astrophys. J.* **606**, 702–740 (2004). arXiv:astro-ph/0310725.

[53] Tegmark, M. *et al.* Cosmological parameters from SDSS and WMAP. *Phys. Rev. D* **69**, 103501 (2004). arXiv:astro-ph/0310723.

[54] Dodelson, S. & Liguori, M. Can cosmic structure form without dark matter? *Phys. Rev. Lett.* **97**, 231301 (2006).

[55] Jenkins, A. *et al.* Evolution of Structure in Cold Dark Matter Universes. *Astrophys. J.* **499**, 20 (1998). arXiv:astro-ph/9709010.

[56] Massey, R., NASA & ESA. URL http://hubblesite.org/newscenter/archive/releases/2007/16/image/p/.

[57] Scoville, N. *et al.* The Cosmic Evolution Survey (COSMOS): Overview. *Astrophys. J. Suppl.* **172**, 1–8 (2007). arXiv:astro-ph/0612305.

[58] Massey, R. *et al.* Dark matter maps reveal cosmic scaffolding. *Nature* **445**, 286–290 (2007). arXiv:astro-ph/0701594.

[59] Leauthaud, A. *et al.* Weak Gravitational Lensing with COSMOS: Galaxy Selection and Shape Measurements. *Astrophys. J. Suppl.* **172**, 219–238 (2007). arXiv:astro-ph/0702359.

[60] Bertone, G., Hooper, D. & Silk, J. Particle dark matter: evidence, candidates and constraints. *Phys. Rep.* **405**, 279–390 (2005). arXiv:hep-ph/0404175.

[61] Jungman, G., Kamionkowski, M. & Griest, K. Supersymmetric dark matter. *Phys. Rep.* **267**, 195–373 (1996). arXiv:hep-ph/9506380.

[62] Weinberg, S. Approximate symmetries and pseudo-goldstone bosons. *Phys. Rev. Lett.* **29**, 1698–1701 (1972).

[63] Birkedal, A., Noble, A., Perelstein, M. & Spray, A. Little higgs dark matter. *Phys. Rev. D* **74**, 035002 (2006).

[64] Bergström, L. Non-baryonic dark matter: observational evidence and detection methods. *Rep. Prog. Phys.* **63**, 793–841 (2000). arXiv:hep-ph/0002126.

[65] Ahlen, S. *et al.* The Case for a Directional Dark Matter Detector and the Status of Current Experimental Efforts. *Int J. Mod. Phys. A* **25**, 1–51 (2010). 0911.0323.

[66] Wikström, G. & Edsjö, J. Limits on the WIMP-nucleon scattering cross-section from neutrino telescopes. *J. Cosmol. Astropart. Phys.* **4**, 9 (2009). 0903.2986.

[67] Brunner, J. The antares neutrino telescope–status and first results. *Nucl. Instr. Meth. Phys. Res. A* **In Press**, – (2010).

[68] EDELWEISS Collaboration. First results of the EDELWEISS-II WIMP search using Ge cryogenic detectors with interleaved electrodes. *Phys. Lett. B* **687**, 294–298 (2010). 0912.0805.

[69] Cebrián, S. *et al.* First results of the ROSEBUD dark matter experiment. *Astropart. Phys.* **15**, 79–85 (2001). arXiv:astro-ph/0004292.

[70] Angloher, G. *et al.* Commissioning run of the CRESST-II dark matter search. *Astropart. Phys.* **31**, 270–276 (2009). 0809.1829.

[71] Kraus, H. *et al.* EURECA - The Future of Cryogenic Dark Matter Detection in Europe. In *Identification of Dark Matter 2008* (2008).

[72] Felizardo, M. *et al.* First Results of the Phase II SIMPLE Dark Matter Search. *ArXiv e-prints* (2010). 1003.2987.

[73] Behnke, E. *et al.* Spin-Dependent WIMP Limits from a Bubble Chamber. *Science* **319**, 933 (2008). 0804.2886.

[74] Ahmed, B. *et al.* The NAIAD experiment for WIMP searches at Boulby mine and recent results. *Astropar. Phys.* **19**, 691–702 (2003). arXiv:hep-ex/0301039.

[75] Lee, H. S. *et al.* Limits on Interactions between Weakly Interacting Massive Particles and Nucleons Obtained with CsI(Tl) Crystal Detectors. *Phys. Rev. Lett.* **99**, 091301 (2007). 0704.0423.

[76] Lippincott, W. H. *et al.* Calibration of liquid argon and neon detectors with $^{83}\mathrm{Kr}^{m}$. *Phys. Rev. C* **81**, 045803 (2010). 0911.5453.

[77] Lippincott, W. H. *et al.* Scintillation time dependence and pulse shape discrimination in liquid argon. *Phys. Rev. C* **78**, 035801 (2008).

[78] Sekiya, H. for the XMASS collaboration. XMASS. *ArXiv e-prints* (2010). 1006.1473.

[79] Acciarri, R. *et al.* The WArP experiment. *J. Phys. Conf. Ser.* **203**, 012006 (2010).

[80] Regenfus, C. for the ArDm Collaboration. The argon dark matter experiment (ArDM). *J. Phys. Conf. Ser.* **203**, 012024 (2010). 0912.2962.

[81] URL http://dmtools.brown.edu/. DM Tools.

[82] Savage, C., Gelmini, G., Gondolo, P. & Freese, K. Compatibility of DAMA/LIBRA dark matter detection with other searches. *J. Cosmol. Astropart. Phys.* **4**, 10 (2009). 0808.3607.

[83] Ahmed, Z. for the The CDMS Collaboration. Results from the Final Exposure of the CDMS II Experiment. *ArXiv e-prints* (2009). 0912.3592.

[84] Aprile, E. *et al.* New measurement of the relative scintillation efficiency of xenon nuclear recoils below 10 keV. *Phys. Rev. C* **79**, 045807 (2009). 0810.0274.

[85] Aprile, E. *et al.* First Dark Matter Results from the XENON100 Experiment. *ArXiv e-prints* (2010). 1005.0380.

[86] Lebedenko, V. N. *et al.* Results from the first science run of the ZEPLIN-III dark matter search experiment. *Phys. Rev. D* **80**, 052010 (2009). 0812.1150.

[87] URL http://cdms.berkeley.edu/. The CDMS collaboration homepage.

[88] Angle, J. *et al.* Limits on Spin-Dependent WIMP-Nucleon Cross Sections from the XENON10 Experiment. *Phys. Rev. Lett.* **101**, 091301 (2008). 0805.2939.

[89] Lebedenko, V. N. *et al.* Limits on the Spin-Dependent WIMP-Nucleon Cross Sections from the First Science Run of the ZEPLIN-III Experiment. *Phys. Rev. Lett.* **103**, 151302 (2009). 0901.4348.

[90] UK Dark Matter Collaboration. Limits on WIMP cross-sections from the NAIAD experiment at the Boulby Underground Laboratory. *Phys. Lett. B* **616**, 17–24 (2005). arXiv:hep-ex/0504031.

[91] Archambault, S. *et al.* Dark matter spin-dependent limits for WIMP interactions on ^{19}F by PICASSO. *Phys. Lett. B* **682**, 185–192 (2009). 0907.0307.

[92] Cooley, J. for the CDMS Collaboration. Results from the CDMS II experiment. *J. Phys. Conf. Ser.* **203**, 012004 (2010). 0912.1601.

[93] The CDMS II Collaboration. Dark Matter Search Results from the CDMS II Experiment. *Science* **327**, 1619 (2010).

[94] Barnabé-Heider, M. *et al.* Response of superheated droplet detectors of the PICASSO dark matter search experiment. *Nucl. Instr. Meth. Phys. Res. A* **555**, 184–204 (2005). arXiv:physics/0508098.

[95] Aubin, F. *et al.* Discrimination of nuclear recoils from alpha particles with superheated liquids. *New J. Phys.* **10**, 103017 (2008). 0807.1536.

[96] URL http://xenon.astro.columbia.edu/. The XENON website at Columbia.

[97] Angle, J. *et al.* First Results from the XENON10 Dark Matter Experiment at the Gran Sasso National Laboratory. *Phys. Rev. Lett.* **100**, 021303 (2008). 0706.0039.

[98] Bernabei, R. *et al.* First results from DAMA/LIBRA and the combined results with DAMA/NaI. *Eur. Phys. J. C* 167 (2008). 0804.2741.

[99] Aalseth, C. E. *et al.* Results from a Search for Light-Mass Dark Matter with a P-type Point Contact Germanium Detector. *ArXiv e-prints* (2010). 1002.4703.

[100] Collar, J. I. & McKinsey, D. N. Comments on "First Dark Matter Results from the XENON100 Experiment". *ArXiv e-prints* (2010). 1005.0838.

[101] Savage, C., Gelmini, G., Gondolo, P. & Freese, K. XENON10/100 dark matter constraints in comparison with CoGeNT and DAMA: examining the Leff dependence. *ArXiv e-prints* (2010). 1006.0972.

[102] Acciarri, R. *et al.* Oxygen contamination in liquid Argon: combined effects on ionization electron charge and scintillation light. *J. Inst.* **5**, 5003 (2010). 0804.1222.

[103] Acciarri, R. *et al.* Effects of Nitrogen contamination in liquid Argon. *J. Inst.* **5**, 6003 (2010). 0804.1217.

[104] Kubota, S. *et al.* Recombination luminescence in liquid argon and in liquid xenon. *Phys. Rev. B* **17**, 2716 (1978).

[105] Kubota, S., Hishida, M. & Nohara, A. Variation of scintillation decay in liquid argon excited by electrons and alpha particles. *Nucl. Instrum. and Methods* **150**, 561–564 (1978).

[106] Himi, S., Takahashi, T., Ruan, J. & Kubota, S. Liquid and solid argon, and nitrogen-doped liquid and solid argon scintillators. *Nucl. Instrum. and Methods* **203**, 153–157 (1982).

[107] Hitachi, A. *et al.* Effect of ionization density on the time dependence of luminescence. *Phys. Rev. B* **27**, 5279 (1983).

[108] Lide, D. R. *CRC Handbook of chemistry and physics : a ready-reference book of chemical and physical data,* 90^{th} *Edition* (CRC Press, 2009).

[109] Doke, T., Masuda, K. & Shibamura, E. Estimation of absolute photon yields in liquid argon and xenon for relativistic (1 MeV) electrons. *Nucl. Instr. Meth. Phys. Res. A* **291**, 617–620 (1990).

[110] Nikkel, J. A., Hasty, R., Lippincott, W. H. & McKinsey, D. N. Scintillation of liquid neon from electronic and nuclear recoils. *Astropart. Phys.* **29**, 161–166 (2008).

[111] Boulay, M. G. & Hime, A. Technique for direct detection of weakly interacting massive particles using scintillation time discrimination in liquid argon. *Astropart. Phys.* **25**, 179 (2006).

[112] Kubota, S., Hishida, M., Suzuki, M. & Ruan, J. Dynamical behavior of free electrons in the recombination process in liquid argon, krypton, and xenon. *Phys. Rev. B* **20**, 3486–3496 (1979).

[113] Boulay, M. G. *et al.* Measurement of the scintillation time spectra and pulse-shape discrimination of low-energy β and nuclear recoils in liquid argon with DEAP-1 (2009). `astro-ph/0904.2930v1`.

[114] Gastler, D. *et al.* Measurement of scintillation efficiency for nuclear recoils in liquid argon. *ArXiv e-prints* (2010). `1004.0373`.

[115] Doke, T. *et al.* Let dependence of scintillation yields in liquid argon. *Nucl. Instr. Meth. Phys. Res. A* **269**, 291–296 (1988).

[116] Doke, T. *et al.* Absolute Scintillation Yields in Liquid Argon and Xenon for Various Particles. *Jpn. J. Appl. Phys.* **41**, 1538 (2002).

[117] Brunetti, R. *et al.* WARP liquid argon detector for dark matter survey. *New Astron. Rev.* **49**, 265–269 (2005). `arXiv:astro-ph/0405342`.

[118] Pasuthip, P. *Characterization os pulse-shape discrimination for background reduction in the DEAP-1 detector.* Master's thesis, Queen's University (2009).

[119] Lippincott, W. H. *Direct detection of dark mater with liquid argon and neon.* Ph.D. thesis, Yale University (2010).

[120] Artna-Cohen, A. Nuclear Data Sheets for A = 228. *Nucl. Data Sheets* **80**, 723 (1997). Data extracted from the ENSDF database, revision of Jan. 2, 1997.

[121] Artna-Cohen, A. Nuclear Data Sheets for A = 224. *Nucl. Data Sheets* **80**, 227 (1997). Data extracted from the ENSDF database, revision of Nov. 18, 1996.

[122] Artna-Cohen, A. Nuclear Data Sheets for A = 216, 220. *Nucl. Data Sheets* **80**, 157 (1997). Data extracted from the ENSDF database, revision of Oct. 25, 1997.

[123] Wu, S. C. Nuclear Data Sheets for A = 216. *Nucl. Data Sheets* **108**, 1057–1092 (2007). Data extracted from the ENSDF database, revision of March. 3, 2007.

[124] Browne, E. Nuclear Data Sheets for A = 212. *Nucl. Data Sheets* **104**, 427–496 (2005). Data extracted from the ENSDF database, revision of Nov. 29, 2004.

[125] Martin, M. J. Nuclear Data Sheets for A = 208. *Nucl. Data Sheets* **108**, 1583–1806 (2007). Data extracted from the ENSDF database, revision of June. 27, 2007.

[126] Browne, E. & Tuli, J. K. Nuclear Data Sheets for A = 234. *Nucl. Data Sheets* **108**, 681–772 (2007). Data extracted from the ENSDF database, revision of Nov. 9, 2006.

[127] Akovali, Y. A. Nuclear Data Sheets for A = 230. *Nucl. Data Sheets* **69**, 155 (1993). Data extracted from the ENSDF database, revision of March 4, 1993.

[128] Akovali, Y. A. Nuclear Data Sheets for A = 226. *Nucl. Data Sheets* **77**, 433 (1995). Data extracted from the ENSDF database, revision of March 6, 1996.

[129] Akovali, Y. A. Nuclear Data Sheets for A = 222. *Nucl. Data Sheets* **77**, 271 (1996). Data extracted from the ENSDF database, revision of Jan. 16, 1996.

[130] Jain, A. K. & Singh, B. Nuclear Data Sheets for A = 218. *Nucl. Data Sheets* **107**, 1027–1074 (2006). Data extracted from the ENSDF database, revision of Dec. 15, 2005.

[131] Wu, S. C. Nuclear Data Sheets for A = 214. *Nucl. Data Sheets* **110**, 681–748 (2009). Data extracted from the ENSDF database, revision of Nov. 1, 2007.

[132] Browne, E. Nuclear Data Sheets for A = 210. *Nucl. Data Sheets* **99**, 483–753 (2003). Data extracted from the ENSDF database, revision of March 26, 2003.

[133] Kondev, F. G. Nuclear Data Sheets for A = 206. *Nucl. Data Sheets* **109**, 1557–1654 (2008). Data extracted from the ENSDF database, revision of March 24, 2008.

[134] Benetti, P. *et al.* Measurement of the specific activity of ^{39}Ar in natural argon. *Nucl. Instr. Meth. Phys. Res. A* **574**, 83–88 (2007). `arXiv:astro-ph/0603131`.

[135] Acosta-Kane, D. *et al.* Discovery of underground argon with low level of radioactive ^{39}Ar and possible applications to WIMP dark matter detectors. *Nucl. Instr. Meth. Phys. Res. A* **587**, 46–51 (2008).

[136] Mei, D. *et al.* Prediction of underground argon content for dark matter experiments. *Phys. Rev. C* **81**, 055802 (2010). `0912.5368`.

[137] Brun, R. & Rademakers, F. ROOT - An object oriented data analysis framework. *Nucl. Instr. Meth. Phys. Res. A* **389**, 81–86 (1997).

[138] Cai, B., Pollman, T. & Boulay, M. Surface backgrounds in the DEAP-3600 detector. DEAP internal document.

[139] Pollamn, T., Boulay, M. & Kuźniak, M. Scintillation of thin tetraphenyl butadiene films under alpha particle excitation. *Submitted for publication* (2010).

[140] URL `http://www.srim.org/`. Stopping and Range of Ions in Matter (SRIM).

[141] Boulay, M. DEAP high and low-energy backgrounds. (2009). URL `https://www.snolab.ca/deap/private/TWiki/bin/view/Main/BackgroundNotesAug72009`. Entry on DEAP TWiki.

[142] FAT Results for high-QE DOMs. Tech. Rep. (2009). From the IceCube wiki.

[143] Kauer, M. Calorimeter R&D for the SuperNEMO double beta decay experiment. In *XIII Int. Conf. on Calorimetry in High Energy Physics*, vol. 160, 012031 (IOP Publishing Ltd, London, 2009).

[144] Hamamatsu. *UBA SBA Photomultiplier tube series* (2008).

[145] Electron Tubes. *130mm (5in) photomultiplier 9390B series data sheet* (2009).

[146] The SNO detector: the photomultiplier tubes. URL `http://sno.phy.queensu.ca/sno/sno2.html`. From the SNO homepage at Queen's University.

Appendix A

Data Cleaning Cuts and Zfit Corrections

All corrections and cuts were performed while events were being selected from the ntuples and before being placed into histogram bins. This includes the corrections to TotalPE. All spectra showing α peaks have a cut placed on F_{prompt}, only events with $F_{prompt} > 0.6$ are considered.

Standard data cleaning cuts were performed while events were selected from ntuples:

- abs(Edge0-1000) $<$ 200 & abs(Edge0-Edge1) $<$ 20
- HLatePE0 $<$ 0 & HLatePE1 $<$ 0
- HPromptPE0 $<$ 0 & HPromptPE1 $<$ 0
- EventCutID = 1
- PmtCutID0 = 7 & PmtCutID1 = 7
- abs(PreSignal0) $<$ 0.5 & abs(PreSignal1) $<$ 0.5

In addition to these cuts, a Zfit correction was applied to the data from 2009:

- Zfit = Zfit/(0.962-0.0013$\times$Zfit+0.0005$\times$Zfit^2)

Appendix B

Run List

In Chapters 3 and 4, the following run sets were analysed. The livetime and result from fitting the entire run sets, which use the run-by-run corrections in Appendix C, to run 1360 are both given.

2008				
Run	(to)	Date	Livetime	Fit to run 1360
1360	1361	July 31-Aug 1	56.85	1.000
1667		Sept 24	48.825	1.061
1818	1823	Oct 20-21	19.774	1.006
1871	1874	Oct 28-29	38.497	1.027
1950	1954	Nov 24-25	44.053	1.064
2009				
2102	2105	March 24	37.300	1.000
2151	2155	April 7	41.661	1.011
2197	2202	April 24-27	57.277	1.089
2300	2312	May 21-27	88.86	1.000

Table B.1: list of low-voltage runs from 2008 and 2009 used in the analyses presented in Chapters 3 and 4. Included are correction factors from fitting the run sets to run 1360.

Appendix C

Fitter Results

The following tables are a list of individual runs analysed in Chapter 4 and the results determined by the fitter function to line up their Compton edges with the first run in each set.

2008	
Run	Correction factor
1356	0.998
1357	0.996
1360	1.000
1361	1.011
1667	1.000
1818	1.000
1819	1.006
1820	1.020
1821	1.021
1822	1.027
1823	1.023
1871	1.000
1872	1.002
1873	1.009
1874	1.012
1950	1.000
1951	1.002
1952	1.007
1953	1.003
1954	1.007

2009			
Run	Correction factor	Run	Correction factor
2102	1.000	2279	1.006
2103	1.014	2280	1.005
2104	1.015	2300	1.000
2105	1.018	2301	1.003
2151	1.000	2302	1.009
2152	1.008	2303	1.012
2153	1.011	2304	1.010
2154	1.018	2305	1.014
2155	1.020	2306	1.019
2197	1.000	2307	1.013
2198	1.003	2308	1.010
2199	1.009	2309	1.011
2200	1.011	2310	1.010
2201	1.014	2311	1.002
2202	1.014	2312	1.000
2271	1.000	2317	1.000
2272	1.010	2318	1.005
2273	1.012	2319	1.011
2274	1.013	2320	1.014
2275	1.019	2321	1.013
2276	1.014	2322	1.015
2277	1.015	2323	1.013
2278	1.010	2324	1.020
		2325	1.018

Table C.1: List of runs from the 2008 and 2009 underground runs and their correction factors from fitting each run to the first run in their respective run sets. The analysis is discussed in Chapter 4.

Appendix D

List of NIMs Used in Tests

This is list of the Nuclear Instrumentation Modules used during the tests of both PMTs.

- HV power supply: Bertan Associates, inc. Model 375P
- Discriminator: LeCroy 623 Octal Discriminator
- Gate generator: LeCroy 222 Dual Gate Generator
- Fan-in/fan-out: LeCroy 428F Linear fan-in/fan-out (×2)
- Logic: LeCroy 365AL 4-Fold Logic Unit
- Time to pulse height converter: Ortec 437A TPHC
- Counter: Philips PM6654 Programmable high resolution timer/counter
- Pulse generator: Berkley Nucleonics Corp. 7085 Digital Delay/Width Generator

Appendix E

Cicuit Diagrams for Custom Electronics

The following are circuit diagrams for some of the electronics used for PMT measurements that were designed and built by the Electronics Shop of the Department of Physics at the University of Alberta. Included are the bases for both PMTs and the preamplifer used for them. The base for the ET PMT was designed at Queen's University and built at the University of Alberta.

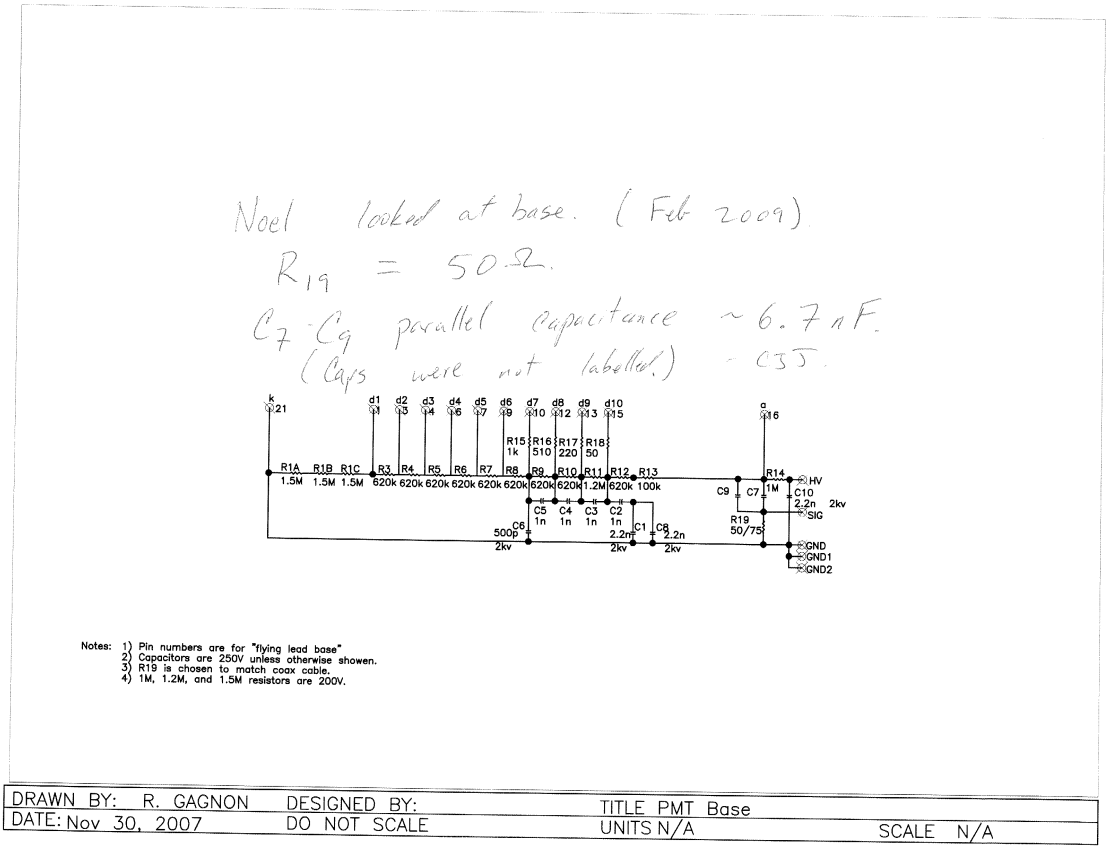

Figure E.1: Circuit diagram for the base used to operate the ET 9390B PMT, designed at Queen's University.

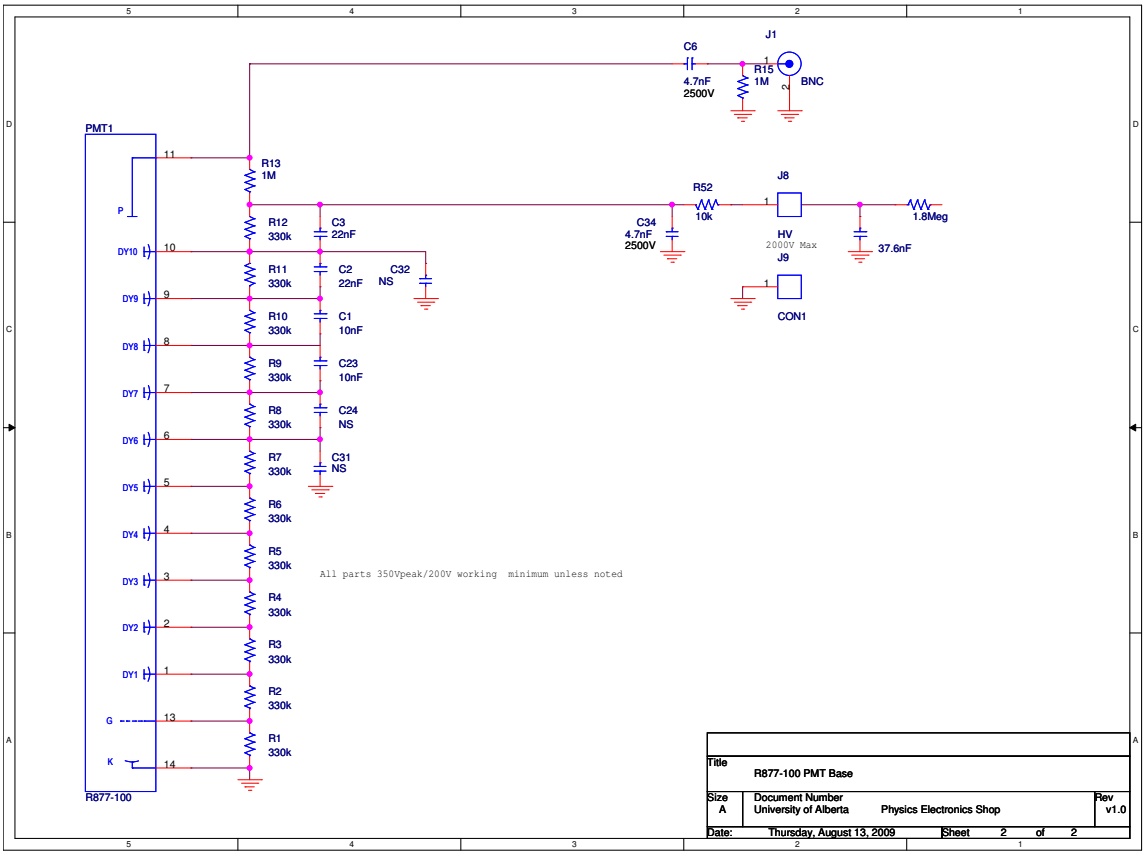

Figure E.2: Circuit diagram for the base used to operate the Hamamatsu R877-100 SBA PMT.

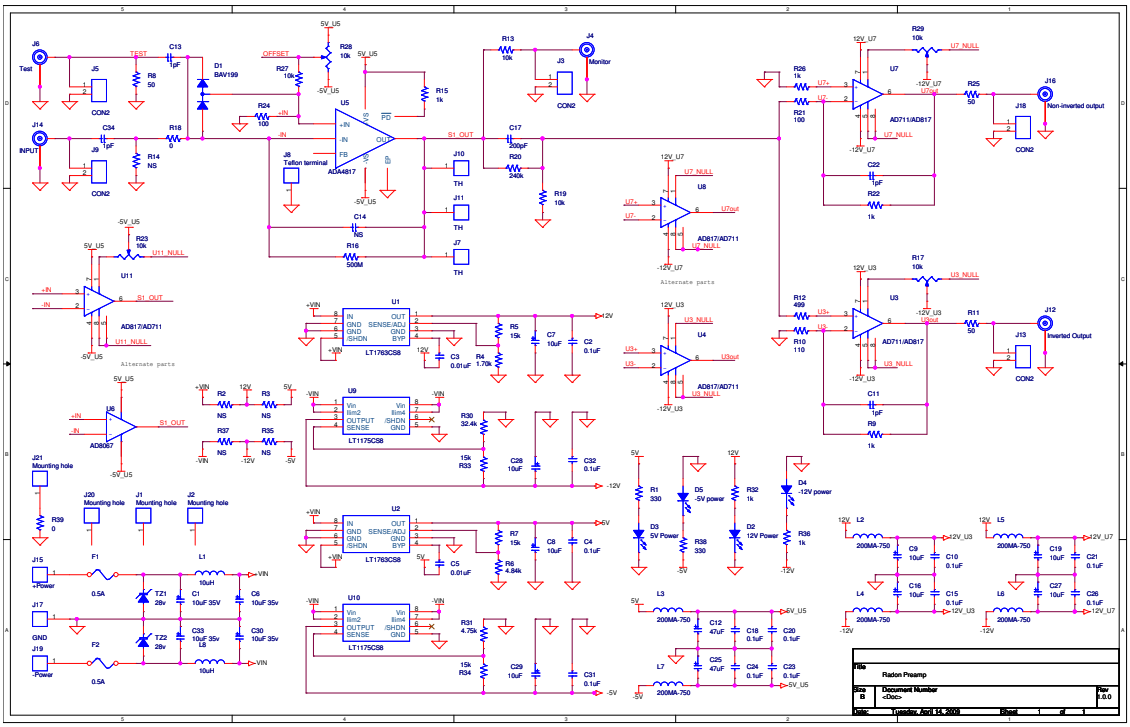

Figure E.3: Circuit diagram for the preamplifer used by both PMTs to measure their response.